

# Ejection processes in the young open cluster NGC 2264

## A study of the [OI] $\lambda$ 6300Å emission line\*

P. McGinnis<sup>1,2</sup>, C. Dougados<sup>1</sup>, S. H. P. Alencar<sup>2,1</sup>, J. Bouvier<sup>1</sup>, and S. Cabrit<sup>3</sup>

<sup>1</sup> Univ. Grenoble Alpes, CNRS, IPAG, 38000 Grenoble, France

e-mail: [pauline@fisica.ufmg.br](mailto:pauline@fisica.ufmg.br)

<sup>2</sup> Departamento de Física - ICEx - UFMG, Av. Antônio Carlos, 6627, 30270-901 Belo Horizonte, MG, Brazil

<sup>3</sup> LERMA, Observatoire de Paris, CNRS, 61 Av. de l'Observatoire, 75014 Paris, France

Received 24 July 2017 / Accepted 21 March 2018

### ABSTRACT

**Context.** Statistical studies of the spectral signatures of jets and winds in young stars are crucial to characterize outflows and understand their impact on disk and stellar evolution. The young, open cluster NGC 2264 contains hundreds of well-characterized classical T Tauri stars (CTTS), being thus an ideal site for these statistical studies. Its slightly older age than star forming regions studied in previous works, such as Taurus, allows us to investigate outflows in a different phase of CTTS evolution.

**Aims.** We search for correlations between the [OI] $\lambda$ 6300 line, a well-known tracer of jets and winds in young stars, and stellar, disk and accretion properties in NGC 2264, aiming to characterize the outflow phenomena that occur within the circumstellar environment of young stars.

**Methods.** We analyzed FLAMES spectra of 184 stars, detecting the [OI] $\lambda$ 6300 line in 108 CTTSs and two Herbig AeBe stars. We identified the main features of this line: a high-velocity component (HVC), and a broad and narrow low-velocity components (BLVC and NLVC). We calculated luminosities and kinematic properties of these components, then compared them with known stellar and accretion parameters.

**Results.** The luminosity of the [OI] $\lambda$ 6300 line and its components correlate positively with the stellar and accretion luminosity. The HVC is only detected among systems with optically thick inner disks; the BLVC is most common among thick disk systems and rarer among systems with anemic disks and transition disks; and the NLVC is detected among systems with all types of disks, including transition disks. Our BLVCs present blueshifts of up to 50 km s<sup>-1</sup> and widths consistent with disk winds originating between ~0.05 au and ~0.5 au from the central object, while the NLVCs in our sample have widths compatible with an origin between ~0.5 au and ~5 au, in agreement with previous studies in Taurus.

A comparison of [OI] $\lambda$ 6300 profiles with CoRoT light curves shows that the HVC is found most often among sources with irregular, aperiodic photometric variability, usually associated with CTTSs accreting in an unstable regime. No stellar properties ( $T_{eff}$ , mass, rotation) appear to significantly influence any property of protostellar jets. We find jet velocities on average similar to those found in Taurus.

**Conclusions.** We confirm earlier findings in Taurus which favor an inner MHD disk wind as the origin of the BLVC, while there is no conclusive evidence that the NLVC traces photoevaporative disk winds. The [OI] $\lambda$ 6300 line profile shows signs of evolving as the disk disperses, with the HVC and BLVC disappearing as the inner disk becomes optically thin, in support of the scenario of inside-out gas dissipation in the inner disk.

**Key words.** accretion, accretion disks – line: formation – stars: jets – stars: pre-main sequence – stars: winds, outflows

## 1. Introduction

Outflows are a ubiquitous aspect of star formation. Powerful, highly collimated, bipolar jets are commonly found in association with YSOs of different evolutionary stages. The many similarities between jets emanating from these different sources suggest that the same physical mechanism is at work in different stages of star formation (Cabrit 2002). Though it has been well established that these ejection phenomena are closely associated with disk accretion (Cabrit et al. 1990; Hartigan et al. 1995, hereafter HEG95), likely occurring as the byproduct of magnetic acceleration from the inner accretion disk (Ferreira et al. 2006; Ray et al. 2007), the exact mechanism which drives them is not yet

well understood. On the other hand, spectroscopic signatures of slow winds ( $v \approx$  a few 10 km s<sup>-1</sup>) are also detected among CTTS in optical (e.g., Kwan & Tademaru 1995; Natta et al. 2014, hereafter N14) as well as infrared forbidden lines (see e.g., Pascucci et al. 2011; Alexander et al. 2014, and references therein). The link of these slow wind signatures with the faster jets is not well established, neither is their impact and role in the evolution of protoplanetary disks. Photoevaporation by high-energy radiation from the central object, which likely contributes significantly to the dispersion of the gas disk (Alexander et al. 2014), has been put forward as a possible origin for these winds (e.g., Ercolano & Owen 2010, 2016).

Statistical studies to test which stellar (or disk) properties scale with jet or wind properties are crucially needed to shed light on these outflow phenomena and their impact on disk and stellar evolution. Young, accreting, low-mass stars known as

\* Tables C.1, C.2, C.3 and C.4 are available in electronic form at the CDS via anonymous ftp to cdsarc.u-strasbg.fr (130.79.128.5) or via <http://cdsweb.u-strasbg.fr/cgi-bin/qcat?J/A+A/>

classical T Tauri stars (hereafter, CTTS), are optically visible, thus allowing us to obtain good estimates of stellar and accretion properties. They are Class II objects, meaning they are associated with well-characterized Keplerian disks. These aspects make them ideal sites to search for correlations between jet or wind properties and stellar or disk properties.

One of the strongest spectroscopic tracers of jets and winds in CTTSs is the forbidden [OI] $\lambda$ 6300 emission line. This line profile has traditionally been separated into two distinct features: a low-velocity component (LVC), centered close to the stellar rest frame or blueshifted by up to  $\sim 20$  km s $^{-1}$ , and a high-velocity component (HVC), blueshifted by  $\sim 50 - 200$  km s $^{-1}$  from the stellar rest frame (HEG95). The HVC is believed to arise in the fast, bipolar jets that are associated with these young objects, while the LVC seems to originate in slower moving winds. N14 found line ratios between [SII] $\lambda$ 4069, [OI] $\lambda$ 6300 and [OI] $\lambda$ 5578 consistent with the LVC arising from slow ( $< 20$  km s $^{-1}$ ), dense ( $n_{\text{H}} > 10^8$  cm $^{-3}$ ), warm ( $T \sim 5000\text{K} - 10000\text{K}$ ), mostly neutral gas. Its precise origin, however, is still debated. Possible scenarios for its formation are: centrifugally driven magnetohydrodynamic (MHD) disk winds (HEG95, Kwan & Tademaru 1995); thermally driven disk winds, powered by photoevaporation from X-ray (Ercolano & Owen 2010, 2016) or extreme ultra-violet (EUV, Font et al. 2004) radiation from the central object; or slower thermal winds from a cooler disk region heated by far-ultraviolet (FUV) radiation from the central object, where the [OI] $\lambda$ 6300,5577 emission is nonthermally excited by OH photodissociation (e.g., Gorti et al. 2011).

In recent studies (Rigliaco et al. 2013; Simon et al. 2016, hereafter R13 and S16, respectively), the LVC has been analyzed in more detail and is found to be often composed of two components itself, a narrow and a broad component (NC and BC, respectively). By comparing not only the full widths at half maximum (FWHM) of the two components but also the [OI] $\lambda$ 5577/[OI] $\lambda$ 6300 line ratios, which differ between the two components in the sources where both were detected with high signal-to-noise ratio (S/N), S16 have concluded that the broad and narrow components of the LVC should originate in distinct regions of the accretion disk. They find that the broad component presents larger blueshifts and narrower lines with lower disk inclination, a trend that is expected for a disk wind. They also argue that the large FWHM of the broad component are consistent with emitting regions very close to the central object (at  $R \sim 0.05 - 0.5$  au), within the critical radius for even 10 000K gas, and therefore this component cannot trace a photoevaporative wind. The NC seems to come from farther out in the disk (at  $R \sim 0.5 - 5$  au). Its nature is less clear and the possibility that it could trace a photoevaporative disk wind has not been excluded.

Statistical studies using high resolution ( $R \gtrsim 20\,000$ ) spectroscopic data are necessary to fully understand the different components of the [OI] $\lambda$ 6300 line. So far, S16 has been the only statistical work conducted in this sense, with a limited sample of 33 objects in the Taurus star forming region (Nisini et al. 2018, hereafter N18, have conducted a study of the [OI] $\lambda$ 6300 line in a sample of over 100 objects in Lupus, Chameleon and  $\sigma$  Orionis, but with insufficient resolution to separate the broad and narrow low-velocity components). It is important to extend such studies to a larger number of objects in other star forming regions to investigate the origins of the different features of the [OI] $\lambda$ 6300 line.

The young, open cluster NGC 2264, located at a distance of  $d = 760$  pc (Sung et al. 1997; Gillen et al. 2014), has been the object of an extensive observational campaign entitled the Coordinated Synoptic Investigation of NGC 2264 (CSI2264, Cody

et al. 2014), in which a number of its low-mass members have been thoroughly characterized in terms of stellar properties (e.g., Venuti et al. 2014), accretion properties (e.g., Sousa et al. 2016) and photometric variability (e.g., Cody et al. 2014). In this paper, we take advantage of the extensive knowledge available on the CTTSs belonging to NGC 2264, in order to search for correlations between the different components of the [OI] $\lambda$ 6300 line and stellar and/or disk and accretion properties.

Our spectroscopic data, taken by the FLAMES/GIRAFFE multi-object spectrograph, mounted on the VLT (ESO), cover a narrower wavelength range than the previous studies mentioned (HEG95, R13, S16), therefore we analyze only the [OI] $\lambda$ 6300 line and cannot determine line ratios. However, our work has the advantage of its sample size, including over 100 [OI] $\lambda$ 6300 line profiles, whereas the previous studies mentioned have been limited to 30-50 objects. Our sample is unique in that it is the first to offer high-precision, high-cadence light curves from the CoRoT satellite for most of the objects studied, making it an ideal opportunity to perform statistical studies of outflows in young stars in conjunction with their photometric variability and rotational properties. Besides this, NGC 2264 is an older star forming region ( $\sim 3-5$  Myr $^{-1}$ ) than those studied in previous works (such as Taurus and Lupus, of  $\sim 1-3$  Myr), allowing us to investigate outflows during a slightly later phase of CTTS evolution.

This paper is organized in the following manner: in Sect. 2 we describe the observations of NGC 2264 in the [OI] $\lambda$ 6300 line, taken for the present study; in Sect. 3 we describe the [OI] $\lambda$ 6300 line profiles we find in our sample; in Sect. 4 we describe correlations we find between the different components of the [OI] $\lambda$ 6300 line and stellar and accretion properties; in Sect. 5 we discuss the connection between the [OI] $\lambda$ 6300 line profile and the stars' photometric variability; in Sect. 6 we discuss our results and the possible origins of each component of the [OI] $\lambda$ 6300 line; and finally in Sect. 7 we present a summary along with our conclusions.

## 2. Observations and data reduction

We observed a total of 487 stars in the direction of NGC 2264 with the VLT FLAMES multi-object spectrograph (Pasquini et al. 2002) using the GIRAFFE/MEDUSA HR13 setup under ESO program ID 094.C-0467(A). The data were provided by ESO after being treated for standard reduction procedures using ESO pipelines, which consist of bias and bad pixel removal, flat-field corrections and wavelength calibrations. The chosen setup covers the wavelength range from 6120Å to 6405Å with a spectral resolution of  $R \sim 26\,500$ , which is very similar to the resolution used by HEG95. It is sufficient to disentangle the different components of the low velocity component of the [OI] $\lambda$ 6300 line (which was not originally done by HEG95).

Of the 487 observed stars, 483 are cataloged as members of NGC 2264 according to the criteria described in Cody et al. (2014). Of these, 237 are weak-line T Tauri stars (WTTS, nonaccreting low-mass stars), 182 are classified as classical T Tauri stars according to Venuti et al. (2014) and criteria described therein, and two are Herbig Ae/Be stars (hereafter HAeBe, young intermediate mass stars with strong emission lines). The remaining 62 have unknown spectral types and have not shown any indication of accretion in previous studies.

The targets were distributed among four different fields, two of which were observed with three different fiber configurations

<sup>1</sup> There is, however, strong evidence for a significant age spread in this cluster (see Dahm 2008; Venuti et al. 2017b).

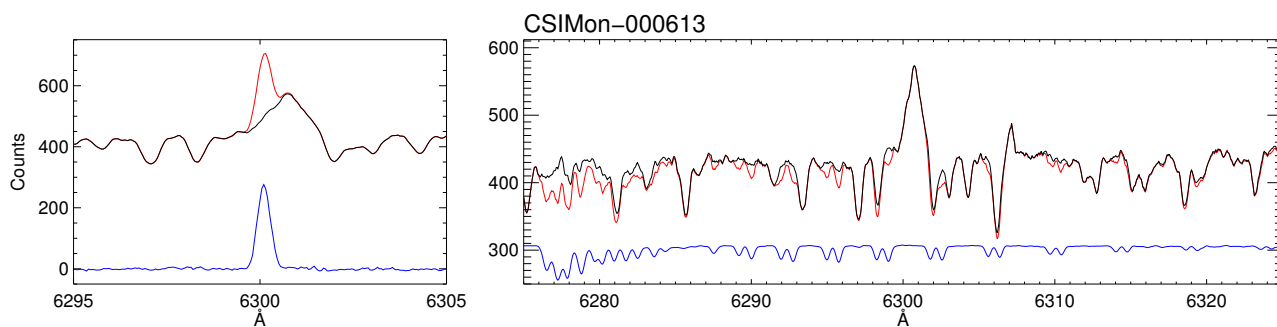


Fig. 1: Example of the process to remove telluric emission and absorption lines from the stellar spectra. Left: the original spectrum is shown in red; the isolated contamination, taken as the average of 3 sky spectra that were observed simultaneously with the stellar spectrum, is shown below in blue; and the result after subtraction is overplotted in black. Right: the spectrum, now with the telluric emission line removed, is shown in red; the telluric absorption line template, scaled and shifted vertically to facilitate a comparison with the stellar spectrum, is shown below in blue; and the final decontaminated spectrum is overplotted in black.

in order to include all targets, giving us a total of 8 different configurations. Each of these configurations was observed at least once for 40 minute exposures, while one was observed four times in a period of  $\sim 2.5$  months (identified as configuration A1). Since the spectral feature we are interested in for the scope of this paper, the [OI] $\lambda 6300$  emission line, is not expected to vary significantly in the time between these observations (HEG95), we added the four spectra after having removed all contaminating effects, obtaining spectra of larger signal-to-noise ratio for the stars observed in this configuration.

The [OI] $\lambda 6300$  emission line is contaminated by a telluric emission line and telluric absorption lines that must be removed in order to recover the intrinsic line profile. For this reason, a number of FLAMES fibers were allocated to regions of the sky where no star was found and only the telluric emission spectrum could be observed. For each stellar spectrum, we used a  $\chi^2$  minimizing technique to identify among the sky spectra observed simultaneously with it the three that most closely match the contamination. We shifted them in wavelength when necessary to best coincide with the contamination, then took the average of the three profiles and subtracted this from the stellar spectrum (see left panel of Fig. 1). This contamination was very strong on most nights, typically much stronger than in the Taurus spectra analyzed by S16. However, this feature is much narrower (it is unresolved in our spectra) than emission coming from circumstellar disks, which makes it easy to identify. Since it is not very variable spatially and many sky fibers were spread around the field of view, we were able to properly identify this contamination and subtract it, even when it was strongly blended with the source's [OI] emission line. Nonetheless, this strong feature may have overshadowed some of the weaker low-velocity emission in our sample, causing the [OI] $\lambda 6300$  emission to go undetected in some of our sources.

After subtracting the telluric emission line, we then proceeded to remove the contamination from telluric absorption lines, which affect the wavelength range from approximately 6275Å to 6325Å. We combined the normalized spectra of two A0-type stars, CSIMon-005644<sup>2</sup> and CSIMon-001235, the first of which was observed four times, to create a template. These stars were chosen because they are hot enough that they have no photospheric features in this region, therefore after normalizing

to the continuum only the telluric absorption spectrum remains. The telluric absorption spectrum is generally not very variable and this template proved to be a good match for all but one of our observed fields. For the final field a star observed simultaneously was needed. There were no A or B-type stars in this field, therefore the template was created using the G-type star CSIMon-001126. This star has high projected velocity ( $v \sin i$ ), leading to very broad photospheric lines, which could be easily identified and fitted with synthetic spectra. The photospheric contribution could then be subtracted from the original spectrum in order to isolate the telluric absorption lines and create the template. The stellar spectra were then divided by the respective templates in the affected wavelength interval in order to eliminate the contamination (right panel of Fig. 1). The left panels of Fig. D.1 show the telluric corrections of all spectra in which a residual [OI] $\lambda 6300$  emission line was detected.

### 3. The [OI] $\lambda 6300$ line profiles

#### 3.1. Recovering intrinsic [OI] $\lambda 6300$ emission line profiles

In order to identify forbidden [OI] $\lambda 6300$  emission in the stellar spectra, it is often necessary to eliminate the photospheric contribution to the spectrum, thus isolating the emission line. Photospheric absorption lines that lie close to the [OI] $\lambda 6300$  emitting region can affect the emission line and even bring it to levels below our detection level, especially when the emission is weak. We chose a sample of WTTS spectra to serve as photospheric templates to compare with our CTTS spectra. We selected WTTSs with spectral types in the range found for our CTTSs and of low  $v \sin i$ 's (rotational velocity projected onto our line of sight). Figure D.2 shows these WTTS's spectra, ordered according to spectral type, while Table C.1 (available at the CDS) provides some of their stellar parameters. Spectral types of both classical and weak-lined TTSs were taken from Venuti et al. (2014), who adopted the values of Dahm & Simon (2005), Rebull et al. (2002) or Walker (1956), in that order of preference, or derived them from CFHT colors when no classification was available in the literature.

We compared each CTTS spectrum to at least three different WTTS templates, which were broadened to adjust for the CTTS's rotation and had an added continuum to simulate veiling (excess accretion flux that affects optical and UV spectra in the presence of accretion shocks on the stellar surface). The templates used were of the same or nearly the same spectral type as the CTTS in question. However, to find the best fit,

<sup>2</sup> The CSIMon ID is a naming scheme devised for the CSI2264 campaign (see Cody et al. 2014), and comprises all cluster members, candidates and field stars in the NGC 2264 region observed during the campaign.

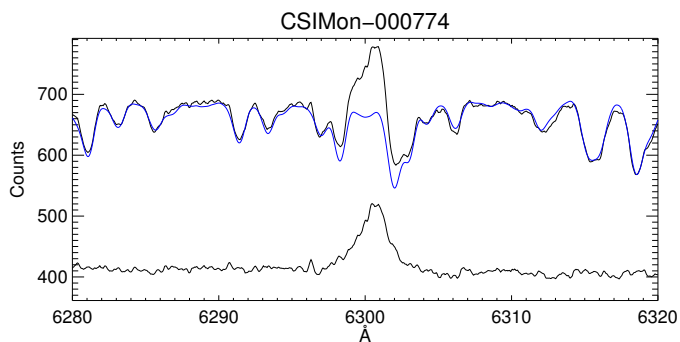


Fig. 2: Example showing the photospheric contribution being removed from a CTTS spectrum in order to recover the intrinsic [OI] $\lambda$ 6300 emission line profile. The veiled, broadened WTTS template is shown in blue, plotted over the CTTS spectrum in black. Below, the final product is shown, shifted vertically to facilitate a comparison with the original spectrum. We can see that the wings of this profile are recovered after removing the photospheric absorption lines.

templates of different spectral types were also tested whenever necessary, in order to account for possible misclassifications of spectral types in the literature. The amount of veiling and rotational broadening were adjusted to the values that simultaneously minimized  $\chi^2$ . The broadened, veiled template with lowest  $\chi^2$  was then subtracted from the CTTS spectrum to recover the intrinsic [OI] $\lambda$ 6300 line profile (see Fig. 2). The right panels of Fig. D.1 show the photospheric corrections of all spectra in which a residual [OI] $\lambda$ 6300 emission line was detected.

In a few cases we found that the best match for a WTTS+veiling template to the star in question was of a different spectral type than the one listed for the star. In three cases we found the difference to be by more than two sub-spectral types. We attribute this to a possible misclassification of the star's spectral type in the literature, possibly due to the excessive amount of veiling presented by these stars, which can interfere with photometric determinations of spectral type. Table 1 provides the spectral type of the WTTS template that best reproduced their photospheric absorption lines. We also found that the stars CSIMon-001149 and CSIMon-001234 are double-lined spectroscopic binaries. Table C.2 (available at the CDS) lists stellar parameters of all CTTSs in our sample, such as their spectral types (from the literature and from our best fits), stellar luminosity, mass and radius (determined uniformly for nearly all stars in our sample in Venuti et al. 2014), as well as our derived values of veiling and  $v \sin i$ .

The Herbig Be star CSIMon-000392 did not undergo photospheric subtraction, since there are no photospheric features in the vicinity of the [OI] $\lambda$ 6300 line in such hot stars. In this case, the continuum was fitted with a fourth order polynomial and subtracted from the spectrum in order to recover the residual profile. This was also done for the stars CSIMon-000423, CSIMon-000632, and CSIMon-001011, which showed such low S/N in their photospheric lines that no photospheric features were detected near the [OI] $\lambda$ 6300 line. The Herbig Ae star CSIMon-000631 presents a shallow, broad absorption line redward of 6300Å. A template of the same spectral type (A2/3) was not found for this star, since few early-type stars were included in our observations. Therefore, in order to remove the contaminating feature, we used as its photospheric template an F-type star with a similar feature close to the [OI] $\lambda$ 6300 line. We fitted only

the region closest to this feature, ignoring the rest of the spectrum.

After removing the photospheric contribution to the spectra, we searched for [OI] $\lambda$ 6300 emission in our stars. We considered as a detection any emission with a peak above  $3\sigma$  and FWHM above the resolution of our spectra, which we measured as  $11.3 \text{ km s}^{-1}$ . Values of  $\sigma$  represent the noise in the residual spectra, measured from two regions of the continuum 5Å before and after the [OI] $\lambda$ 6300 line. A few cases where a marginal detection was found in the exact region where the telluric emission line was originally located were considered as residual contamination from the telluric line and eliminated from the list of detections.

Among our 182 CTTSs, 108 (59%  $\pm$ 4%) show emission in the [OI] $\lambda$ 6300 line, as well as both HAeBe stars in our sample. This low number is somewhat unexpected, since past studies have shown that most accreting T Tauri stars present emission in the forbidden [OI] $\lambda$ 6300 line (HEG95 and Cabrit et al. 1990, for example, detect the [OI] $\lambda$ 6300 line in 100% of the accreting TTSs in their sample, while N14, S16 and N18 detect it, respectively, in 84%, 91%, and 77% of theirs). As shown in Appendix A, we believe this low detection rate may be due to incompleteness. Since NGC 2264 is farther than the star forming regions of these previous studies (Taurus, Lupus,  $\sigma$  Ori) and the targets are therefore fainter, our observations may have been unable to detect the weakest [OI] $\lambda$ 6300 emission lines. Besides this, the telluric emission line in our spectra was often much stronger than in the spectra of S16 (this can be seen in the left panels of Fig. D.1), which very likely interfered with our detection, especially of weaker, low-velocity emission. To avoid any issues this incompleteness may bring about, we include upper limits of nondetections in our analyses whenever possible. We discuss the completion of our sample in more detail in Appendix A.

All profiles shown in this paper have been shifted to the stellar rest velocity  $v_{rad}$  (given in Table C.2), which was determined during the cross-correlation with WTTS spectra. The stellar rest velocities of the WTTSs were found by comparing photospheric absorption lines with those of the synthetic spectrum of closest effective temperature to the star's, adjusted for  $v \sin i$ . Synthetic spectra were created using the program Spectroscopy Made Easy (SME, Valenti & Piskunov 1996) and atomic line files extracted from the Vienna Atomic Line Database (VALD, Kupka et al. 2000, 1999; Ryabchikova et al. 1997; Piskunov et al. 1995) and were broadened to the instrumental resolution. Uncertainties in  $v_{rad}$  are around  $3 \text{ km s}^{-1}$  for most of our sample, but they can reach up to  $\geq 10 \text{ km s}^{-1}$  for a few spectra that present very low S/N in the photospheric lines ( $\sim$ 5% of our sample). Appendix B explains how these uncertainties were estimated.

### 3.2. Characterizing [OI] $\lambda$ 6300 emission line profiles

It has been shown that the [OI] $\lambda$ 6300 emission line profile may present up to three distinct features (R13, S16): a high-velocity component (HVC), a narrow low-velocity component (NLVC) and a broad low-velocity component (BLVC). We identified, as best as we could, each of these features in our [OI] $\lambda$ 6300 line profiles, in order to investigate their origins and their connection to stellar and disk properties. Some profiles clearly show two or three peaks (see the left panel of Fig. 3 for an example), though many profiles have only one clear peak but are asymmetric or very broad at the base. We therefore performed a Gaussian decomposition of all profiles in order to find which ones consist of various components and estimate the centroid velocity and width

Table 1: Spectral types from the literature and from our comparison with WTTS templates for the stars that showed the largest discrepancies among the two.

CSIMon ID	2MASS ID	SpT (lit)	Our SpT	Veiling
CSIMon-000406	J06405968+0928438	K3 <sup>a</sup>	M1	0.85
CSIMon-000474	J06410682+0927322	G <sup>b</sup>	K2	0.15
CSIMon-000795	J06411257+0952311	G:V:e <sup>b</sup>	K2	1.03

**Notes.** The first and second columns give the stars' IDs in the CSIMon and 2MASS catalogs, respectively; spectral types from the literature are given in the third column and from our comparison with WTTS templates in the fourth column; and the fifth column gives the value of veiling (ratio of excess flux to stellar flux) derived from our spectra.

<sup>(a)</sup>Venuti et al. (2014)

<sup>(b)</sup>Dahm & Simon (2005)

of each component, as well as their uncertainties (derived in Appendix B). To determine how many Gaussians are necessary to reproduce an emission profile, reduced  $\chi^2$  values were compared for fits with up to four Gaussians, and the number that resulted in  $\chi^2$  closest to 1 was taken, as long as all components had peak intensity above  $2\sigma$ . The right panel of Fig. 3 shows an example of this Gaussian decomposition (the Gaussian decomposition of all profiles is shown in Fig. D.3).

In order to classify the different components found through these Gaussian fits, we initially used the definition of NLVC, BLVC and HVC provided by S16: all components of  $|v_c| \geq 30 \text{ km s}^{-1}$  were classified as HVCs, those of  $|v_c| < 30 \text{ km s}^{-1}$  with  $\text{FWHM} > 40 \text{ km s}^{-1}$  were classified as BLVCs, and those of  $|v_c| \leq 30 \text{ km s}^{-1}$  with  $\text{FWHM} \leq 40 \text{ km s}^{-1}$  were classified as NLVCs. However, when using these criteria to separate the components in our sample, we found a few inconsistencies. There are ten systems in which, rather than a NLVC and a BLVC, we identified instead two BLVCs, i.e., two components of  $|v_c| \leq 30 \text{ km s}^{-1}$  and  $\text{FWHM} > 40 \text{ km s}^{-1}$ . No source in S16 presented more than one NLVC or BLVC. This suggests that the threshold between narrow and broad LVCs may be slightly different in our sample than in S16's. Besides this, among the profiles with blended HVCs, we found three components identified as HVCs that presented relatively low centroid velocities ( $30 \text{ km s}^{-1} < |v_c| < 50 \text{ km s}^{-1}$ ) and were very broad, showing  $\text{FWHM} > 165 \text{ km s}^{-1}$  (and up to  $\text{FWHM} \sim 250 \text{ km s}^{-1}$ ). This is broader than the spectrally resolved HVCs in our sample, all of which show  $\text{FWHM} < 165 \text{ km s}^{-1}$ . Hence, it is possible that these are in fact BLVCs extending to slightly larger blueshifts (up to  $50 \text{ km s}^{-1}$ ) than probed by the S16 sample.

These issues suggested the need to derive new criteria to classify the different components based on our own sample, rather than rely on previously derived definitions. This would account for intrinsic differences that may exist between the different samples. This is also the first time that the [OI] $\lambda$ 6300 line is studied in over 100 profiles at high spectral resolution<sup>3</sup>, allowing for a statistical analysis of the distribution of FWHM and centroid velocity of the different components of the [OI] $\lambda$ 6300 line. We perform this analysis in the following section in an attempt to properly identify the different components in our sample. It is important to note, however, that the limits between the different components will always be somewhat arbitrary when analyzing only one emission line, especially since there is some overlap between the different components (this is because of the different geometries in which the systems are viewed, which affect both the widths and centroid velocities of the emission).

<sup>3</sup> N18 have studied a sample of similar size, but with lower resolution, which did not allow them to disentangle the narrow and broad low-velocity components.

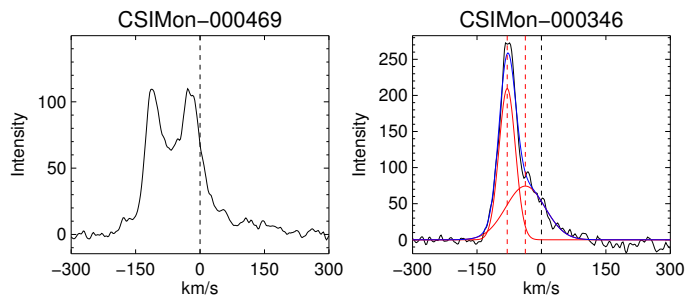


Fig. 3: Two examples of [OI] $\lambda$ 6300 emission line profiles found in our sample. Left: two distinct peaks can be identified, one close to the stellar rest velocity and the other blueshifted by over  $100 \text{ km s}^{-1}$ . Right: Gaussian decomposition of a very asymmetric profile. Two separate Gaussians are shown in red, while the sum of the two is shown in blue, overplotted onto the observed profile (black).

### 3.3. Classification of the different components of the [OI] $\lambda$ 6300 line for the NGC 2264 sample

The right panel of Fig. 4 shows the distribution of FWHM and centroid velocity of all of the components derived from all of the Gaussian fits, and on the left panel a surface plot of the same distribution, with the z axis representing the number of Gaussian components in square bins of  $5 \text{ km s}^{-1} \times 5 \text{ km s}^{-1}$ . There is evidently a very high concentration of components at low, slightly blueshifted centroid velocities and low FWHM. We interpret this as the locus of the narrow LVCs studied by R13 and S16. A Gaussian fit around the surface plot (left panel of Fig. 4) has a  $1\sigma$  width represented in the right panel as a green ellipse. If this truly represents the locus of the narrow component of the LVC, then this component should typically have  $v_c = -2.7 \pm 5.8 \text{ km s}^{-1}$  and  $\text{FWHM} = 37.9 \pm 9.5 \text{ km s}^{-1}$  (where the  $1\sigma$  uncertainty has been taken as the standard deviation of the distribution). If we consider a  $3\sigma$  threshold, then the narrow LVCs should have  $-20.0 \text{ km s}^{-1} < v_c < 14.6 \text{ km s}^{-1}$  and  $\text{FWHM} < 66.6 \text{ km s}^{-1}$ . None of the components are narrower than  $11.3 \text{ km s}^{-1}$ , since this is the resolution of our spectra and therefore this width represents the instrumental profile.

The cutoff in centroid velocity between LVCs and HVCs varies in the literature from  $30 \text{ km s}^{-1}$  (S16) to  $60 \text{ km s}^{-1}$  (HEG95) and is always somewhat arbitrary. In our sample, the lowest centroid velocity of a HVC with a spectrally resolved peak is  $-48.3 \text{ km s}^{-1}$ , but this does not necessarily represent the cutoff between low and high velocity components, only our ability to resolve separate peaks. In an attempt to better characterize the different components and search for the best value at which

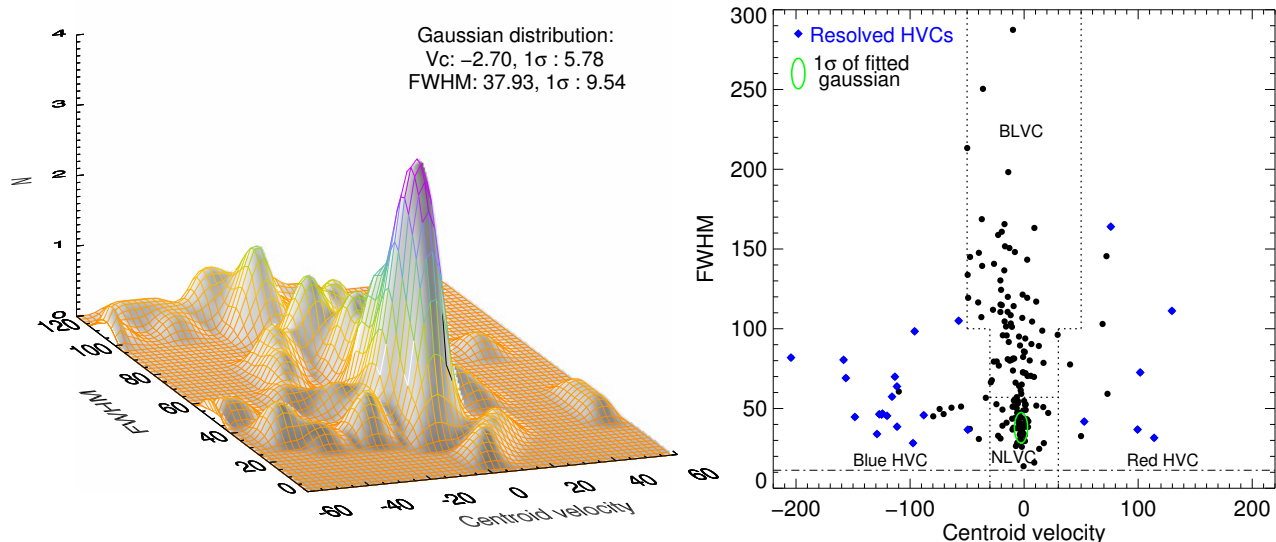


Fig. 4: Right: distribution of FWHM and centroid velocity of all components from all profiles derived from the Gaussian fits. Dotted lines indicate the separation between different components - narrow and broad LVC, red- and blueshifted HVC, according to our analysis (though there is some overlap between the NLVC and BLVC). The dashed-dotted line represents our instrumental profile, below which no components are found. Blue diamonds represent high-velocity components whose peaks are resolved, and not blended with the low-velocity emission. Left: surface plot of the central region of the distribution shown in the right panel, where the z axis represents the number of Gaussian components in square bins of  $5 \text{ km s}^{-1} \times 5 \text{ km s}^{-1}$ . The primary peak corresponds to the locus of the narrow LVC, while the secondary peak represents a concentration of broad LVCs.

to separate the HVC from the NLVC and BLVC, we analyzed the distribution of centroid velocity and FWHM of the different components that are present within the same profile. We began by selecting a sample of 21 stars whose profiles consisted of two Gaussian components with centroid velocity below  $30 \text{ km s}^{-1}$ , in which one was clearly broader than the other<sup>4</sup>. These profiles can help to better distinguish between the narrow and broad components of the LVC. Figure 5 shows the distribution of centroid velocity and FWHM of the LVCs of these 21 stars, with shaded bins representing the narrowest of a profile's two components, and striped bins representing the broadest. We see that the NLVC is generally close to stellar rest velocity or slightly blueshifted, while the centroid velocity of the BLVC varies more.

We then repeated Fig. 5, this time for a group of 28 stars that showed two components of centroid velocity  $|v_c| < 50 \text{ km s}^{-1}$  where, once again, one was clearly broader than the other (Fig. 6). The narrower of the two components continues to show the same behavior, having centroid velocities between  $-24.3 \text{ km s}^{-1}$  and  $8.9 \text{ km s}^{-1}$  in both Figs. 5 and 6, consistent with the value of  $|v_c| < 30 \text{ km s}^{-1}$  used by S16 and with our characterization of the NLVC from Fig. 4. The broader component, however, extends to more blueshifted velocities in Fig. 6, up to  $\sim 50 \text{ km s}^{-1}$ . The right panel of Fig. 4 also shows that there are a number of components with blueshifts of up to  $50 \text{ km s}^{-1}$  that are broader than the clear HVCs (those that present  $|v_c| > 50 \text{ km s}^{-1}$ ), whose FWHMs typically fall below  $\sim 100 \text{ km s}^{-1}$ . These components are therefore likely BLVCs, showing that this component can indeed present blueshifts of up to  $\sim 50 \text{ km s}^{-1}$ , unlike the NLVC.

The FWHM of the NLVC reaches  $59.2 \text{ km s}^{-1}$ , close to the lower limit of  $66.2 \text{ km s}^{-1}$  of the broader component. This would suggest that the threshold between these two components

<sup>4</sup> We exclude from this sample two systems which have photometric variability attributed to occultation by the inner disk (McGinnis et al. 2015), since they are likely observed at high inclination and therefore projection effects may be causing a HVC to have  $|v_c| < 30 \text{ km s}^{-1}$ .

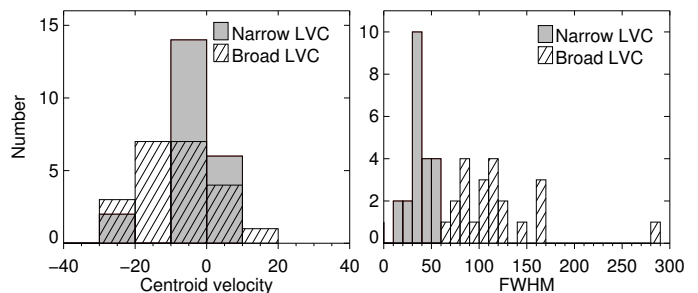


Fig. 5: Distribution of centroid velocity (left) and FWHM (right) of the components from our Gaussian fits for a group of stars that present two LVCs ( $|v_c| < 30 \text{ km s}^{-1}$ ). Shaded bins represent the narrowest of the two components while striped bins represent the broadest.

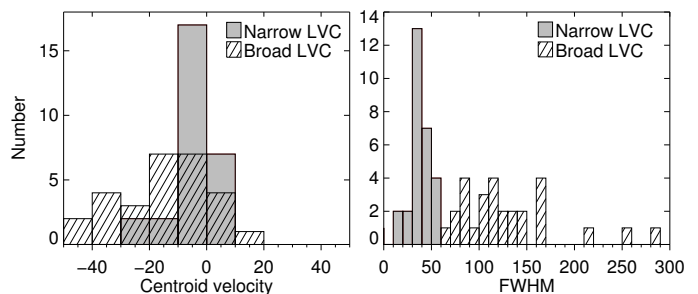


Fig. 6: Same as Fig. 5, but taking components with centroid velocities less than  $50 \text{ km s}^{-1}$ .

is around  $60 \text{ km s}^{-1}$ . However, S16 found at least two [OI] $\lambda 6300$  line profiles with two low-velocity components, in which the broadest of the two had  $\text{FWHM} < 60 \text{ km s}^{-1}$ . This shows that

there is a small overlap between the two components, probably due to projection effects because of the different geometries of the individual star-disk systems. Therefore we take  $57 \text{ km s}^{-1}$  as our cutoff between NLVC and BLVC, which corresponds to  $2\sigma$  of a normal distribution around the primary peak seen in Fig. 4, in the FWHM axis. More than 95% of the NLVCs in Figs. 5 and 6 have FWHM below this value, in accordance with the  $2\sigma$  level of a normal distribution. Using this value rather than  $3\sigma$  will likely minimize the amount of BLVCs that are misclassified as NLVCs, though some misclassification will be inevitable, given that there is some overlap between the components.

Figures 5 and 6 suggest that the cutoff in centroid velocity between the LVC and the HVC should be around  $50 \text{ km s}^{-1}$ . However, for systems seen at high inclinations, the [OI] $\lambda$ 6300 emission coming from a high-velocity jet would be observed at lower projected velocities. If, for instance, a system is observed at an inclination of  $80^\circ$ , emission from a jet traveling at  $200 \text{ km s}^{-1}$  would be centered at  $35 \text{ km s}^{-1}$  ( $v_{jet} * \cos i$ ). We appear to have a few cases like this in our sample. For example, the star CSIMon-000228 shows a broad component centered close to rest velocity and a narrower component (FWHM =  $56.7 \text{ km s}^{-1}$ ) centered at  $-33.6 \text{ km s}^{-1}$ , which is more blueshifted than a typical narrow LVC. We do not have direct measurements of inclination for the stars in this cluster, but we can deduce from its rotation properties that this star is observed at a very high inclination. This component is therefore consistent with a HVC.

In the end, the following criteria were used to classify each component. Firstly, all components with  $|v_c| < 30 \text{ km s}^{-1}$  were classified as LVCs. When more than one component from an emission profile satisfied this condition, the broadest was classified as a broad LVC and the narrowest as a narrow LVC. When there was only one component, it was classified as narrow if FWHM  $< 57 \text{ km s}^{-1}$  and broad if FWHM  $\geq 57 \text{ km s}^{-1}$  (from the analysis of Figs. 4, 5 and 6). There were no cases of more than two components in this velocity bin. Secondly, all components with  $|v_c| > 50 \text{ km s}^{-1}$  were classified as HVCs.<sup>5</sup> Finally, the components with centroid velocity between  $30 \text{ km s}^{-1}$  and  $50 \text{ km s}^{-1}$  were classified as HVCs when their FWHM was less than  $100 \text{ km s}^{-1}$  and as BLVCs if FWHM  $\geq 100 \text{ km s}^{-1}$ . This is justifiable by the fact that the FWHM of the HVC measures the internal velocity dispersion within the jet, and is not expected to exceed  $100 \text{ km s}^{-1}$  unless there is a considerable velocity variability within the beam. Furthermore, using this criterion, there were no cases in which more than one BLVC was identified in the same source. However, we must note that the choice of where to establish a threshold in FWHM between HVC and BLVC is based only on the distribution seen in Fig. 4 and is thus somewhat arbitrary. Therefore there may be some misclassification in this velocity bin.

Of the 182 CTTSs and 2 HAeBe stars observed in NGC 2264, we detected emission in the [OI] $\lambda$ 6300 line of both HAeBe stars and 108 CTTSs, all but one of which presented a LVC (the only exception being CSIMon-001249, which shows both a red and blueshifted HVC; a LVC is likely present, but blended within the two HVCs). Among them, we found a total of 64 narrow LVCs and 75 broad LVCs, with 30 systems presenting both of these components. A HVC, however, was only found in 31 profiles (28% of the total detections). This represents only 17% of all CTTSs and HAeBe stars observed, a much

lower detection rate than was expected<sup>6</sup>. We performed K-S tests between the distributions of FWHM and  $v_c$  of the different components and all proved to be statistically different, with a  $\leq 1\%$  probability that the distributions draw from the same population.

Table 2 presents a summary of the different types of profiles found in our sample, showing how many detected profiles present each of the different components and how many present a combination of two or more of these components. The different components are characterized in terms of their centroid velocities ( $v_c$ ) and full width at half maximum (FWHM) in Table 3.

Both the BLVC and the NLVC appear to be more blueshifted whenever a HVC is present in the system. For the BLVC, the average  $v_c$  is  $-9.3 \text{ km s}^{-1}$  (with a standard deviation of  $\sigma = 15.7 \text{ km s}^{-1}$ ) and  $-19.2 \text{ km s}^{-1}$  ( $\sigma = 16.4 \text{ km s}^{-1}$ ) among systems without and with a detected HVC, respectively. For the NLVC, the respective numbers are  $-1.5 \text{ km s}^{-1}$  ( $\sigma = 8.7 \text{ km s}^{-1}$ ) and  $-9.9 \text{ km s}^{-1}$  ( $\sigma = 7.7 \text{ km s}^{-1}$ ). For the NLVC, a KS test shows that the distributions of the centroid velocities of the two samples (stars that present a HVC and stars that do not) are statistically different, with a probability of deriving from the same population of less than 1%. There is no statistically significant difference in the distributions of FWHM among the two samples for either component. This difference in centroid velocities may be caused by a geometrical effect, since it has been previously shown that systems observed at lower inclinations, which are more favorable to detect a HVC, tend to present BLVCs of larger blueshifts (S16). On the other hand, this effect could simply be due to the difficulty of separating the low-velocity components when a HVC is blended in the profile. In these cases, the LVCs may have been artificially shifted toward the blue in the Gaussian decomposition.

#### 3.4. Comparison of our sample of LVCs with previous studies

In this section, we summarize the differences between the narrow and broad low-velocity components of the [OI] $\lambda$ 6300 line in our sample and in the sample of S16, the only previous study in which the distinction between these two components has been made for a large number of profiles. Figure 7 shows the distributions of centroid velocity and FWHM for both the narrow and broad components of the LVCs in our sample and in that of S16. In this section, we use the widths corrected for the instrumental profiles (referred to as FWHM<sub>cor</sub>, to avoid confusion with the uncorrected widths), in order to accurately compare the two samples of different spectral resolutions. Besides this, throughout this section we use S16's definition of NLVC and BLVC for our components as well, in order to compare the two samples regardless of the difference in definitions used to classify the components (i.e., BLVCs have  $|v_c| < 30 \text{ km s}^{-1}$  and FWHM<sub>cor</sub>  $> 40 \text{ km s}^{-1}$  and NLVCs have  $|v_c| < 30 \text{ km s}^{-1}$  and FWHM<sub>cor</sub>  $\leq 40 \text{ km s}^{-1}$ ). Using these definitions, we find a total of 29 NLVCs and 100 BLVCs in our sample, while S16 had found 18 NLVCs and 25 BLVCs in the Taurus sample.

Table 4 summarizes the comparison between the two samples. This table gives the mean and standard deviation ( $\sigma$ ) of the distributions of centroid velocity and FWHM<sub>cor</sub> of each component in both samples. We also give the results of KS tests performed between the distributions.

The left and middle panels of Fig. 7 show that, when using the same criteria to classify the low-velocity components as S16, both the NLVCs and BLVCs show very similar distributions of centroid velocity between the two samples. A KS test

<sup>5</sup> There were two cases (stars CSIMon-000260 and CSIMon-000392) in which two blueshifted HVCs were found. Multiple HVCs have been detected in other studies as well (e.g., S16).

<sup>6</sup> This may be due to a sensitivity issue, as discussed in Appendix A.

Table 2: Number of profiles that present each of the different components (narrow LVC, broad LVC, redshifted HVC and blueshifted HVC) or a combination of two or more components.

Only LVC			Have HVC				
Only NLVC	Only BLVC	NLVC+BLVC		NLVC+HVC	BLVC+HVC	NLVC+BLVC+HVC	Only HVC
				7 profiles	15 profiles	8 profiles	1 profile
27 profiles	30 profiles	22 profiles		Of which the HVC are:			
			Blueshifted:	3 profiles	12 profiles	5 profiles	0 profiles
			Redshifted:	1 profiles	2 profile	1 profile	0 profiles
			Both:	3 profiles	1 profile	2 profiles	1 profile
Total number of stars with				NLVCs: 64;	BLVCs: 75;	HVCs: 31	

Table 3: Information about the centroid velocities ( $v_c$ ) and FWHM of the different components of the [OI] $\lambda$ 6300 emission line.

		Min	Max	Mean	Median	$1\sigma$
<b>NLVC:</b>	$v_c$	-29.2	21.1	-3.5	-2.7	9.1
Detected in 64 profiles	FWHM	13.8	66.4	41.6	41.1	10.6
<b>BLVC:</b>	$v_c$	-49.9	29.4	-12.4	-11.8	16.5
Detected in 75 profiles	FWHM	61.4	287.4	112.5	104.5	41.7
<b>Blueshifted HVC:</b>	$v_c$	-204.4	-33.6	-100.3	-109.9	41.3
Detected in 27 profiles	FWHM	28.3	105.0	54.3	46.8	19.3
<b>Redshifted HVC:</b>	$v_c$	40.3	129.6	79.8	73.1	28.2
Detected in 11 profiles	FWHM	31.6	164.0	79.6	72.6	46.1

**Notes.** All values are in units of  $\text{km s}^{-1}$ . The instrumental profile is  $11.3 \text{ km s}^{-1}$ . In the final column,  $1\sigma$  is the standard deviation of the distributions of  $v_c$  and FWHM.

between the centroid velocities of the BLVCs in our sample and in the sample of S16 gives a high probability ( $P = 20\%$ ) that the distributions derive from the same population, with a very similar result ( $P = 24\%$ ) for the NLVC. Even if we include the BLVCs in our sample that extend beyond  $|v_c| = 30 \text{ km s}^{-1}$  up to  $|v_c| = 50 \text{ km s}^{-1}$ , we still find a probability of 8% that the samples derive from the same population, which is high enough to suggest that the difference in the range of  $|v_c|$ 's we observe may not only be due to the different cutoffs chosen between LVC and HVC, but possibly to our larger number statistics, which may have allowed us to sample the tail of the most blueshifted components.

In the right panel of Fig. 7, we can see that the distribution of FWHM of the BLVC is also very similar among the two samples, with a KS test giving a 91% probability that they derive from the same population. Our values extend further than those of S16 (the figure is clipped at  $180 \text{ km s}^{-1}$  for clarity, but there is one component in our sample whose FWHM reaches nearly  $300 \text{ km s}^{-1}$ ), but the result of the KS test shows that this is simply a matter of our larger number statistics, which allowed us to better sample the tail of the distribution. As for the NLVC, we see that the distributions of FWHM differ considerably, with S16 finding many more components narrower than  $25 \text{ km s}^{-1}$  than we do, despite our larger sample size. It is possible that the contamination of the telluric emission line, which is much stronger in our observations than in those of S16 (see the left panels of Fig. D.1 and Fig. 28 of S16), may have made it very difficult for us to recover the narrowest [OI] $\lambda$ 6300 line profiles. The narrow LVCs are generally very close to stellar rest velocity (as illustrated by the middle panel of Fig. 7), which means that they closely coincide with the telluric emission line, and many profiles with only a very narrow LVC may have been entirely engulfed by this contamination. This would also help to explain our low detection rate (discussed in Sect. 3.1 and Appendix A) in comparison with previous studies of the [OI] $\lambda$ 6300 line among accreting T Tauri stars. The higher spectral resolution of S16 (almost twice ours) will also have made it much easier for them to properly remove

Table 4: Comparison between the [OI] $\lambda$ 6300 LVC in NGC 2264 (our sample) and in Taurus (S16)

	This paper		S16		KS test
	Mean	$\sigma$	Mean	$\sigma$	P
<b>NLVC:</b>					
$v_c$	-3.4	8.2	-2.5	4.1	59%
$\text{FWHM}_{cor}$	30.2	9.5	22.5	9.3	30%
<b>BLVC:</b>					
$v_c$	-6.4	11.7	-5.0	9.8	20%
$\text{FWHM}_{cor}$	87.2	40.9	79.9	30.5	91%

**Notes.** The first four columns show the mean and standard deviation ( $\sigma$ ) of the distributions of centroid velocities ( $v_c$ ) and FWHM for the NLVCs and BLVCs of the [OI] $\lambda$ 6300 line in our sample and in the sample of Taurus from S16. The last column shows the results of KS tests between the two samples, restricted to components of  $\text{FWHM} > 25 \text{ km s}^{-1}$ . P is the probability that the distributions derive from the same population.  $\text{FWHM}_{cor}$  represents the FWHM corrected for the instrumental broadening of  $\text{FWHM}_{inst} = 11.3 \text{ km s}^{-1}$ , for our sample, and  $\text{FWHM}_{inst} = 7.0 \text{ km s}^{-1}$ , for S16's sample. The definitions of S16 are used to classify NLVCs and BLVCs in both samples, in order to compare them regardless of the different definitions.

this contamination. In light of this, we compare the two samples of NLVCs only for components of  $\text{FWHM} > 25 \text{ km s}^{-1}$ . In this case, we find a probability of 30% that the distributions of FWHM of the two samples derive from the same population, and a probability of 59% for the centroid velocity of this component.

This study of NGC 2264 and the study of Taurus conducted by S16 probe similar ranges of mass, stellar luminosity and mass accretion rates. However, the average values of all three of these parameters are larger in our sample, when considering only systems with positive [OI] $\lambda$ 6300 detections, than in the sample of S16. Our sample with [OI] detection has an average mass of  $0.88 \pm 0.51 M_{\odot}$  (ranging from  $0.14 M_{\odot}$  to  $3 M_{\odot}$ ), compared to  $0.67 \pm 0.30 M_{\odot}$  for S16; an average stellar

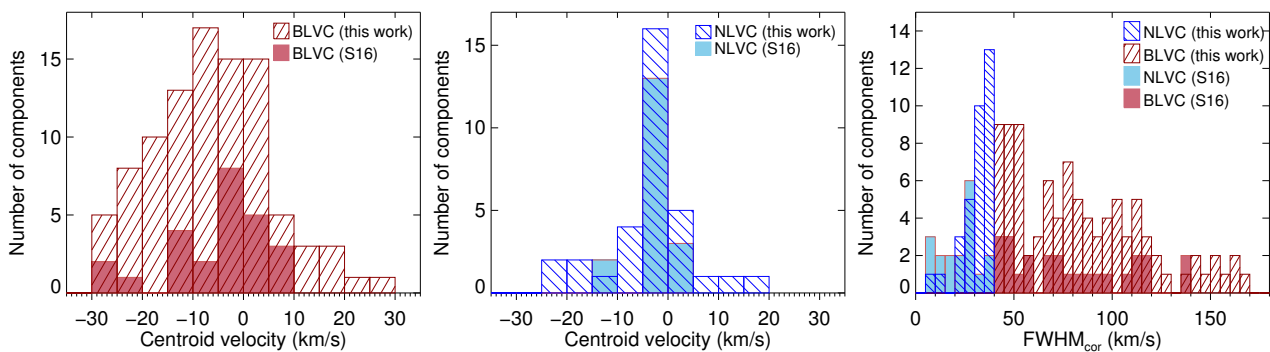


Fig. 7: Comparison of the centroid velocities and FWHM of the low-velocity components of the [OI] $\lambda$ 6300 line in our sample and in S16. Striped red bins represent our broad LVCs, shaded red bins represent the BLVCs of S16, striped blue bins represent our narrow LVCs, and shaded blue bins represent the NLVCs of S16. For this figure, we use the definition of S16 to classify our components, in order to compare the two samples (i.e., BLVCs have  $|v_c| < 30 \text{ km s}^{-1}$  and  $\text{FWHM} > 40 \text{ km s}^{-1}$  and NLVCs have  $|v_c| < 30 \text{ km s}^{-1}$  and  $\text{FWHM} \leq 40 \text{ km s}^{-1}$ ). In the right panel, FWHM have been deconvolved from the instrumental profiles in both samples, in order to compare without the influence of the different spectral resolutions.

luminosity of  $\log L_*/L_\odot = -0.08 \pm 0.45$ , compared to S16's  $\log L_*/L_\odot = -0.36 \pm 0.37$ ; and an average accretion luminosity of  $\log L_{\text{acc}}/L_\odot = -1.05 \pm 0.75$ , compared to  $\log L_{\text{acc}}/L_\odot = -1.69 \pm 0.76$  for S16. The values of X-ray luminosities are very similar in the two samples:  $\log L_X/L_\odot = -3.55 \pm 0.54$  in NGC 2264, versus  $\log L_X/L_\odot = -3.66 \pm 0.59$  in Taurus.

## 4. [OI] $\lambda$ 6300 line luminosities

### 4.1. Recovering equivalent widths and line luminosities

Equivalent widths (EW) were measured for each [OI] $\lambda$ 6300 line profile and its components. In order to estimate uncertainties, we added a random distribution of noise at the same level of the flux uncertainty and calculated the resulting EW. This was done 200 times, then the mean and standard deviation were taken as our final value of EW and its uncertainty. We estimated the EW of the narrow and broad components of the LVC from their Gaussian fits. For the HVC, we took the line's total value, measured by integrating above the continuum over the full profile, minus the EWs of all other components. This is to account for the fact that the HVC usually deviates from a Gaussian profile more than the narrow and broad components of the LVC and therefore using the value derived from the Gaussian fit may result in a larger error. For the 7 stars that present both a redshifted and a blueshifted HVC, we first estimated the EW of each of these components from their Gaussian fits. We then made a second estimate by subtracting the values of all other Gaussian components, including that of the other HVC, from the total [OI] $\lambda$ 6300 line's EW. This slightly overestimates each HVC's EW because the residuals from both components as they deviate from a Gaussian profile are added to each component's measure of EW. Therefore to minimize this effect, we consider this value to be an upper limit and the estimate from the Gaussian fit to be a lower limit, and take the average of the two as the final value. The equivalent widths, as well as the centroid velocities and FWHM, of each component in our sample are given in Table C.3 (available at the CDS).

Our spectra are not flux calibrated, therefore in order to retrieve [OI] $\lambda$ 6300 line luminosities we estimated the continuum flux around  $6300 \text{ \AA}$  using the average  $r$ -band magnitude from the CFHT Megacam 2012 campaign (described in Venuti et al. 2014). To account for a star's variability, we took the amplitude of variability of its CoRoT light curve(s) as the error bar. For

the brightest stars that saturated in the CFHT observations, we used the CoRoT  $R$  magnitudes, which were converted from the mean CoRoT flux using the photometric zero-point of 26.74, as determined by Cody et al. (2014). A comparison of the CFHT  $r$  and CoRoT  $R$  magnitudes in our sample showed that the two coincide very well among the brightest stars ( $R \leq 14$ ) and therefore we introduced very little error by using the CoRoT magnitudes for the stars with no CFHT photometry. Magnitudes were corrected for extinction (see below), then converted to flux using a distance to the cluster of  $d = 760 \text{ pc}$  (Sung et al. 1997; Gillen et al. 2014). The continuum flux was then multiplied by the measured equivalent widths in order to retrieve the luminosities of the [OI] $\lambda$ 6300 line's individual components, which were then added together in order to retrieve the total [OI] $\lambda$ 6300 line luminosity. The values found for each component and for the full [OI] $\lambda$ 6300 line are given in Table C.4 (available at the CDS).

To correct for extinction we used the individual values derived for each star by Venuti et al. (2014). When no value was available, we used the average extinction toward the cluster of  $A_R = 0.40$ , estimated from the stars in our sample with measured extinction. This was done when calculating the luminosity of the [OI] $\lambda$ 6300 line's LVCs. The HVC, however, is believed to arise from jets far enough above the disk mid-plane that it is likely only affected by interstellar extinction in our line-of-sight toward the cluster, and not by the circumstellar disk material of individual objects. Therefore, when calculating the flux in the [OI] $\lambda$ 6300 line's blueshifted HVC, we used the average extinction toward the cluster for all stars rather than their individual values. However, interstellar extinction is not necessarily uniform across the entire cluster, so using the average value may introduce additional uncertainties in the HVC luminosities. Therefore, we took into account the differences between the average value of extinction and individually determined values when calculating the error bars in the [OI] $\lambda$ 6300 HVC luminosity. Most of the stars in NGC 2264 present low extinction that is very similar to the average value of  $A_R = 0.40$ , meaning that this did not result in a large addition to the uncertainty, except for a few stars which seem to be in more embedded regions.

When calculating the luminosity of the redshifted HVCs, the individually derived values of extinction were used, just as for the LVCs. Even so, it is likely that their luminosities were often underestimated, because this emission suffers additional extinction when traversing the circumstellar disk, which should in-

intersect our line-of-sight to the receding part of the protostellar jet. In fact, when a star presents both redshifted and blueshifted high velocity components, the luminosity of the former is usually lower than that of the latter. Therefore care must be taken when analyzing luminosities of the redshifted HVC.

We also calculated  $H\alpha$  line luminosities from equivalent widths and the same estimated continuum flux as for the  $[OI]\lambda 6300$  line, using  $r$ -band or CoRoT magnitudes corrected for individual extinction values. For the range of spectral types considered in this paper there should not be a considerable difference between the continuum flux at  $6300\text{\AA}$  and at  $6563\text{\AA}$ .  $H\alpha$  equivalent widths were taken from previous FLAMES campaigns (Sousa et al. 2016) or from the literature (Rebull et al. 2002; Dahm & Simon 2005).

#### 4.2. Correlations with stellar and accretion properties

We analyzed the relation between the luminosity of the  $[OI]\lambda 6300$  line and its individual components (NLVC, BLVC, and HVC) and different properties of the star, disk and accretion (these properties are given in Table C.2 and the relations can be seen in Fig. D.4). In order to evaluate possible correlations between these properties and the  $[OI]\lambda 6300$  emission line and its different components, we used the ASURV (Astronomy SURVival) package (Lavalley et al. 1992), which implements the methods described in Isobe et al. (1986). We chose these methods because they allow us to perform linear regression and correlation tests while taking into account the upper limits of our non-detections and thus diminishing possible observational biases.

**Stellar luminosity** Stellar bolometric luminosities were determined in a self-consistent way for nearly all stars in our sample by Venuti et al. (2014) and were determined by us following the procedures described therein for the few remaining stars. We find a strong correlation between the stellar luminosity and all components, especially the low velocity components, something that is also seen by N14<sup>7</sup>, S16 and N18<sup>8</sup>. A Kendall  $\tau$  test gives a probability of less than 0.01% that these correlations do not exist.

**Accretion luminosity** Accretion luminosities were calculated from UV excess luminosity by Venuti et al. (2014) when available, and  $H\alpha$  luminosity otherwise (following the relation proposed by Fang et al. 2009). All components of the  $[OI]\lambda 6300$  line correlate well with the accretion luminosity  $L_{acc}$ , or similarly with the mass accretion rate  $\dot{M}_{acc}$ , as has been noted in many previous studies (Cabrit et al. 1990, HEG95, R13, N14, S16, N18). These correlations remain even when we normalize both  $L_{acc}$  and the luminosity of the components of the  $[OI]\lambda 6300$  line by the stellar luminosity  $L_*$ , showing that these correlations are not driven by an underlying correlation with  $L_*$ .

A Kendall  $\tau$  test shows that the probability that  $L_{acc}$  and the luminosities of the different components of the  $[OI]\lambda 6300$  line are not correlated is less than 0.008% for all components. However, for the HVC, if we examine only positive detections we no longer find a clear correlation between  $L_{acc}$  and  $L_{HVC}$ . This correlation has been found in other studies (e.g., N18) and

<sup>7</sup> The studies performed by N14 and N18 were conducted using X-shooter, which has a resolution of only  $R=8,800$  in the  $[OI]\lambda 6300$  line. These studies were therefore unable to separate the broad and narrow components of the LVC in their sample and analyzed the LVC as a whole.

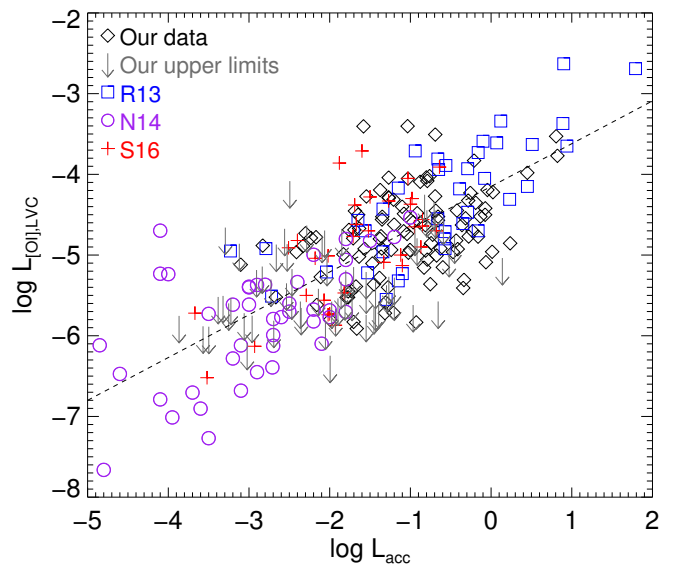


Fig. 8:  $[OI]\lambda 6300$  LVC luminosity versus accretion luminosity. Black diamonds represent our detections, while gray arrows represent our  $3\sigma$  upper limits to the LVC luminosities when no emission in  $[OI]\lambda 6300$  was detected. Blue squares, purple circles and red crosses represent the values given in R13, N14 and S16 for their samples, respectively. The dashed line shows a linear fit to the combination of all four samples, including our upper limits.

many of the nondetections in our sample belong to sources of low accretion luminosities, meaning that they may in fact have weak  $[OI]\lambda 6300$  HVC emission which was below our detection threshold. Therefore it is reasonable to assume that this lack of correlation between the HVC luminosity and accretion luminosity when considering only positive detections should be due to an observational bias. This demonstrates the importance of including upper limits in this analysis.

Using the parametric EM algorithm available in ASURV, we find the following relations for each component of the  $[OI]\lambda 6300$  line:

$$\log L_{NLVC} = -4.64(\pm 0.14) + 0.84(\pm 0.11) \log L_{acc} \quad (1)$$

$$\log L_{BLVC} = -4.52(\pm 0.11) + 0.57(\pm 0.07) \log L_{acc} \quad (2)$$

$$\log L_{HVC} = -4.78(\pm 0.20) + 0.89(\pm 0.15) \log L_{acc}. \quad (3)$$

We can compare our correlations of the LVC with those of R13, N14 and S16. Figure 8 shows the luminosity of the full (narrow+broad) LVC of the  $[OI]\lambda 6300$  line versus accretion luminosity for all four samples. We consider the full LVC rather than the broad or narrow components individually in order to compare with R13, who only decomposed their LVC into separate components for two stars, and N14, who did not have enough spectral resolution to perform this decomposition. We see that all of the samples agree well in both relations, allowing us to establish a well-defined link between the  $[OI]\lambda 6300$  line's LVC luminosity and the accretion luminosity over 7 orders of magnitude. Using once again the EM method, we find the following for the combination of all four samples:

$$\log L_{LVC,all} = -4.15(\pm 0.06) + 0.53(\pm 0.04) \log L_{acc} \quad (4)$$

Equation 4 is in agreement with the relation found for only our sample, using the same method:

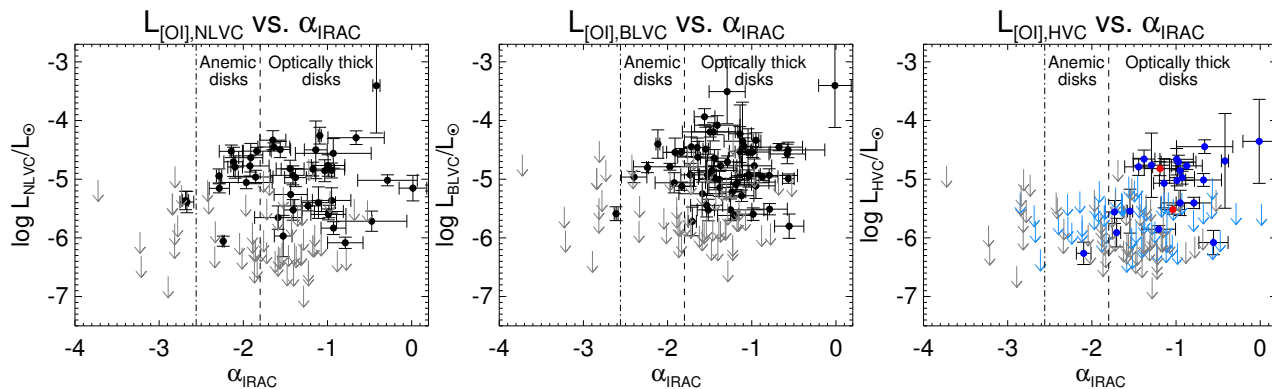


Fig. 9: Luminosity of each [OI] $\lambda$ 6300 component versus the  $\alpha_{IRAC}$  index for all accreting systems. Gray arrows represent upper limits for [OI] $\lambda$ 6300 line luminosities when no emission in [OI] $\lambda$ 6300 was detected. In the HVC plots (right column): light blue arrows represent upper limits for HVC luminosities when only low-velocity [OI] $\lambda$ 6300 emission was detected; blue filled circles represent blueshifted HVCs while red filled circles represent redshifted HVCs (systems that did not present a blueshifted component). Dashed lines represent the boundary between systems with optically thick inner disks (right) and systems with anemic disks (middle), while dashed-dotted lines represent the boundary between systems with anemic disks and naked photospheres, according to  $\alpha_{IRAC}$  (left).

$$\log L_{LVC,ours} = -4.44(\pm 0.11) + 0.64(\pm 0.07) \log L_{acc}. \quad (5)$$

The relation between  $L_{LVC}$  and  $L_{acc}$  is also in agreement with those found by R13, S16 and N18, though our slope is not as steep as the one found by N14 for their data. As for the HVC, our slope of  $L_{HVC}$  vs.  $L_{acc}$  (Eq. 3) agrees with that of N18, though our values of  $L_{HVC}$  in general lie below theirs for the same  $L_{acc}$ .

In Fig. 8, we can see that our upper limits in [OI] $\lambda$ 6300 LVC luminosity are within the same range as the luminosities measured by N14 and S16 in their samples, particularly among the stars of low mass accretion rates ( $L_{acc} \lesssim 10^{-2} L_{\odot}$ ). This strongly supports the idea that our low detection rate, especially among these stars of low accretion luminosity, is likely not due to a physical effect but instead to a sensitivity limit. Many of the stars in our sample where no emission was detected in [OI] $\lambda$ 6300 could in fact present [OI] $\lambda$ 6300 emission that was unfortunately below our detection threshold.

**X-ray luminosity** We also searched for correlations between the luminosity of the [OI] $\lambda$ 6300 line and its components and X-ray luminosities<sup>8</sup> (provided by Ettore Flaccomio, private communication; some of these values are published in Guarcello et al. 2017). The X-ray luminosities do not correlate with the HVC luminosity. However, we find a positive correlation with the luminosity of the LVC, a different result than the one obtained by S16, who find a 10.8% likelihood that no such correlation exists in their sample. In fact, when we separate the contributions of the narrow and broad components, we find that there is only a 0.05% chance that the X-ray luminosity ( $L_X$ ) does not correlate with the broad LVC luminosity, and an even smaller one ( $< 0.001\%$ ) that there is no correlation with the narrow LVC. However, since our data also show a correlation between the X-ray luminosity and the stellar luminosity, it is unclear to us whether the relationships found between  $L_X$  and  $L_{NLVC,BLVC}$  are real or whether they are driven by an underlying correlation with the stellar luminosity. In an attempt to remove the possible influence of the stellar luminosity ( $L_*$ ), we normalized the X-ray luminosities and the [OI] $\lambda$ 6300 line's NLVC and BLVC luminosities by  $L_*$ . We

find no correlation between these two quantities, even spanning a range of around 2 orders of magnitude in  $L_X/L_*$ . Therefore it is likely that the correlations we find between  $L_X$  and  $L_{NLVC}$  or  $L_{BLVC}$  are not intrinsic, but are driven by the stellar luminosity.

**UV luminosity** We also find a correlation between both the NLVC and BLVC luminosities and the luminosity of the CFHT  $u$ -band, with a very low ( $< 0.001\%$ ) probability that it is false. However, since the  $u$ -band flux shows a strong positive correlation with stellar luminosity, it is unclear if the relation we find is real and not driven by the stellar luminosity, as was the case for  $L_X$ . Again, no correlations are found when the [OI] $\lambda$ 6300 line luminosities and UV luminosity are normalized by stellar luminosity (again spanning around 2 orders of magnitude in  $L_{UV}/L_*$ ), meaning that this relation is very likely driven by the stellar luminosity and is not an intrinsic one. Still, it is interesting to note that the NLVC correlates best with the X-ray luminosity, while the BLVC correlates better with the UV flux.

**The  $\alpha_{IRAC}$  index** Figure 9 shows the relation between the luminosities of each of the [OI] $\lambda$ 6300 components and the  $\alpha_{IRAC}$  index, which indicates the amount of dust present in the inner circumstellar disk. This index corresponds to the slope of a star's spectral energy distribution between  $3.6\mu\text{m}$  and  $8\mu\text{m}$  and can be used to classify a system's inner ( $\sim 0.1$  au) disk structure (Lada et al. 2006). The dashed line in Fig. 9 represents the boundary between, on the right, systems with optically thick inner disks and, in the middle, systems with anemic disks (optically thin inner disks), while the dashed-dotted line represents the boundary between systems with anemic disks and, on the left, systems that would be classified as naked photospheres according to the  $\alpha_{IRAC}$  index. It is clear from the right panel that in order to possess high velocity [OI] $\lambda$ 6300 emission, a system must be optically thick in this region of the disk. All systems showing this emission have optically thick inner disks, with the exception of one star (CSIMon-000250) that has an anemic disk and presents a faint [OI] $\lambda$ 6300 HVC. The NLVC is present in a number of anemic disk systems and even some systems classified as naked photospheres according to  $\alpha_{IRAC}$ , while the BLVC seems to show an intermediate behavior, having been observed in some anemic

<sup>8</sup> Measured in the 0.5-8.0 keV band.

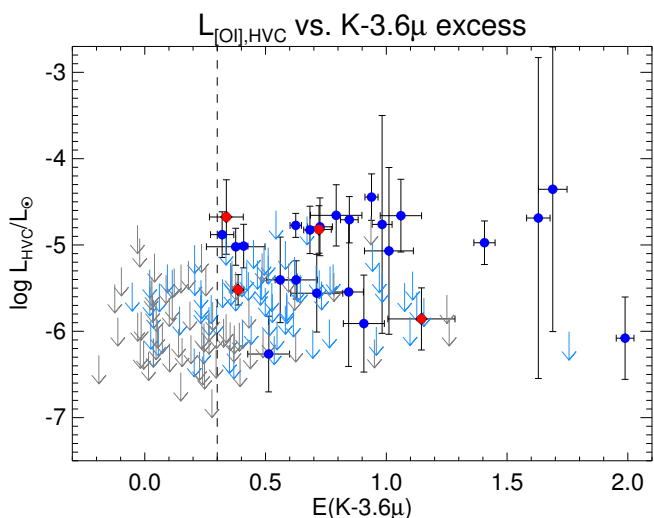


Fig. 10:  $[OI]\lambda 6300$  HVC luminosity versus  $K-IRAC_{3.6\mu}$  excess. The dashed line marks the threshold at  $K-IRAC_{3.6\mu} = 0.3$ , below which the HVC is not detected.

disk systems but not as many as the LVC. These plots point to an evolution of the  $[OI]\lambda 6300$  line profile with the evolution of the disk. Systems with primordial disks often have a BLVC, or a combination of NLVC and BLVC, associated with a HVC. As the disk evolves the HVC disappears, followed by the BLVC, leaving only a NLVC among systems with optically thin inner disks. This is in line with what is discussed by [Ercolano & Pascucci \(2017\)](#) and observed by S16, who show that systems with transition disks (those that present a dust cavity in their inner disk) present almost exclusively a NLVC in their  $[OI]\lambda 6300$  line profile.

**Infrared excess** The  $K - 3.6\mu$  excess probes a region of the disk that is even closer to the star than  $\alpha_{IRAC}$ . Figure 10 shows an even clearer threshold for HVC emission: all systems showing this emission, whether bright or faint, have  $E(K - 3.6\mu) > 0.3$ , the same conclusion reached by HEG95. This indicates that in order for a high velocity jet to be launched, the inner disk region must be optically thick. There is however no correlation between the amount of infrared excess and the jet's luminosity or velocity.

## 5. Photometric variability and the $[OI]\lambda 6300$ line

In this section, we take advantage of the highly detailed light curves made available by the CoRoT satellite for many members of NGC 2264 and for the first time investigate properties of the  $[OI]\lambda 6300$  line profile in relation to a source's photometric behavior. This cluster was observed by CoRoT for 23 days in 2008 and again between Dec 1 2011 and Jan 9 2012, resulting in high precision light curves of hundreds of cluster members ([Alencar et al. 2010](#); [Cody et al. 2014](#)). Of the 108 CTTSs in our sample that present  $[OI]\lambda 6300$  emission, 91 were observed by the CoRoT satellite in either of these two observing runs. The light curves of T Tauri stars have been classified in previous papers according to their morphology into the following groups: spot-like light curves, characterized by a very regular, periodic variability that has been attributed to rotational modulation of stable cold spots on the stellar surface ([Alencar et al. 2010](#)); light curves dominated by irregular flux bursts attributed to abrupt events of increased accretion ([Cody et al. 2014](#); [Stauffer et al. 2014](#));

AA Tau-like light curves ([McGinnis et al. 2015](#)), which resemble that of the CTTS AA Tau in [Bouvier et al. \(1999\)](#), attributed to quasi-periodic occultation events of the stellar photosphere by an inner disk warp; and light curves dominated by aperiodic extinction events attributed to the occultation of the photosphere by irregularly distributed material in the disk ([McGinnis et al. 2015](#)). However, many light curves present a more complex behavior not easily attributed to one of these groups, which may or may not have an underlying periodicity. They are likely the product of a combination of physical mechanisms, though a portion of these light curves has been attributed mainly to time-variable mass accretion producing transient hot spots on the stellar surface ([Stauffer et al. 2016](#)).

It is reasonable to assume that a relatively high inclination is necessary to observe either AA Tau-like occultations or aperiodic extinction events, since optically thick material from the disk must intersect our line-of-sight in order to produce the occulting events. On the other hand, spot-like variability and light curves dominated by flux bursts are probably observed in systems with medium to low inclinations, since extinction events are absent from these light curves, meaning there is no optically thick disk material intersecting our line-of-sight. The complex, difficult to classify, light curves probably represent an intermediate case, where we observe both extinction events and spots on the stellar surface. We can therefore sometimes use the light curve classification to infer system inclinations, which is very useful since we do not have direct inclination measurements for this cluster.

In Fig. 11, comparing the average profile of stars with AA Tau-like or aperiodic extinction-dominated light curves (bottom left) with that of stars with spot-like or flux burst-dominated light curves (top left), we see that the low velocity components of the two profiles are very similar, whereas the high velocity components are not. The average profile of the stars with spot-like or flux burst-dominated light curves has a blueshifted HVC with a clearly separated peak, which is consistent with systems observed close to pole-on possessing fast bipolar jets, since the velocity of these jets projected in our line-of-sight would be close to their terminal velocities and the resulting high velocity  $[OI]\lambda 6300$  emission would be blueshifted enough to be easily distinguished from the  $[OI]\lambda 6300$  emission line's LVC. The average  $[OI]\lambda 6300$  line profile for the stars with AA Tau-like or aperiodic extinction-dominated light curves presents a typical LVC with a somewhat broad base and only a modest extended blue wing. This is consistent with a scenario where these systems are observed nearly edge-on, and therefore even if there were fast jets present, they would be nearly perpendicular to our line-of-sight and the projected velocity would be so low that we would barely be able to distinguish the HVC they produce from a LVC.

The light curve classification can help indicate in which way a CTTS is accreting matter. Magnetohydrodynamic (MHD) simulations (e.g., [Romanova et al. 2008](#); [Kulkarni & Romanova 2008](#)) have shown that it is possible for a star to accrete matter from the disk via a stable accretion regime, where one major accretion funnel flow and accretion shock are present on each hemisphere of the star-disk system; or via an unstable accretion regime, where a series of accretion funnel flows (or accretion "tongues") appear randomly around the star; or even in a sort of boundary between the two, such as the "ordered unstable" regime discussed in [Blinova et al. \(2016\)](#). AA Tau-like photometric variability has been associated with a stable accretion regime ([Bouvier et al. 2007](#); [Romanova et al. 2013](#); [McGinnis et al. 2015](#)), in which an inner disk warp may be produced as

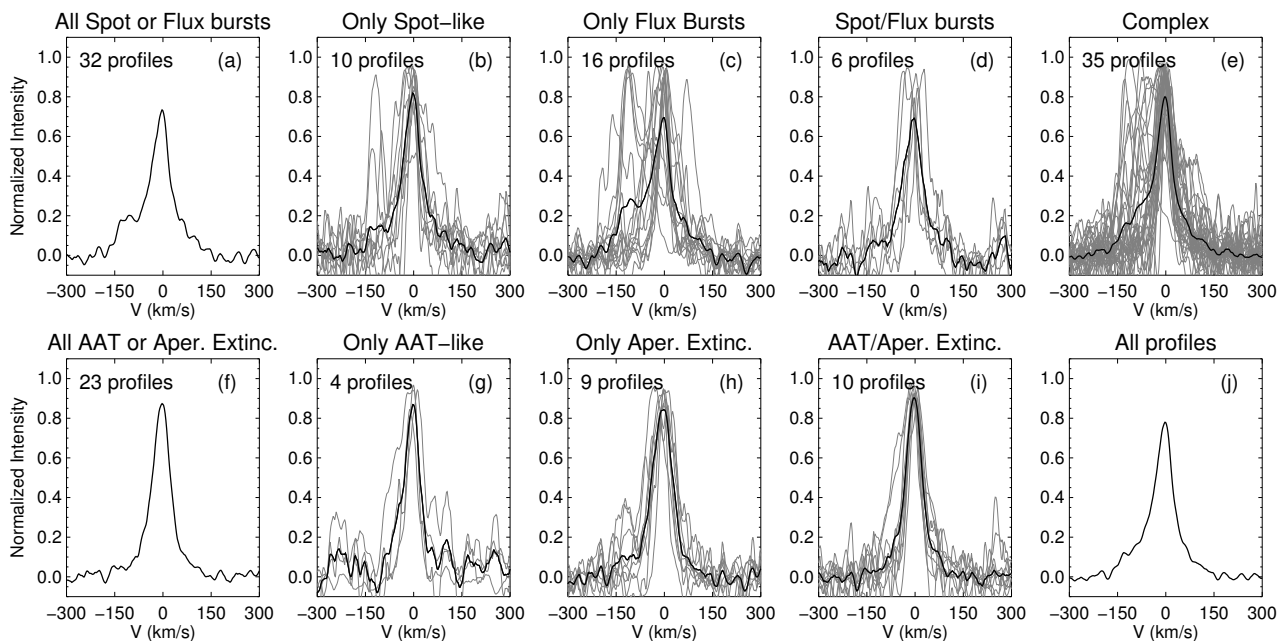


Fig. 11: [OI] $\lambda$ 6300 line profiles for different types of photometric variability. Profiles of individual stars are shown in gray while the average in each group is shown in a thick black. From left to right, top to bottom: (a) stars that presented either spot-like or flux burst-dominated light curves in either CoRoT observation (likely observed at medium to low inclinations); (b) stars with spot-like light curves in both CoRoT observations; (c) stars with light curves dominated by stochastic flux bursts in both CoRoT observations; (d) stars that altered between spot-like and flux bursts between 2008 and 2011; (e) stars with complex (difficult to classify) light curves; (f) stars that presented either AA Tau-like or aperiodic extinction-dominated light curves in either CoRoT observation (likely observed at high inclinations); (g) stars that presented only AA Tau-like light curves in both CoRoT observations; (h) stars that presented only aperiodic extinction-dominated light curves in both CoRoT observations; (i) stars that alternated between AA Tau-like and aperiodic extinction between 2008 and 2011; and finally (j) an average of all [OI] $\lambda$ 6300 line profiles. Each profile was normalized by its maximum intensity before the average was taken.

a consequence of the intense interaction between the inner disk and an inclined, strongly bipolar stellar magnetic field. If a system undergoing stable accretion is observed at a high enough inclination, its light curve would then present quasi-periodic flux dips due to this warp occulting the stellar photosphere as the system rotates. If this system were observed at a lower inclination its light curve would likely be dominated by rotational modulation of stable spots on the stellar surface. On the other hand, Kurosawa & Romanova (2013) show that a system undergoing unstable accretion would probably show stochastic photometric variability due to irregularly distributed hot spots on the stellar surface. McGinnis et al. (2015) proposed that if these systems are observed at sufficiently high inclinations, the light curves could be dominated by irregular obscuration of the photosphere from material lifted above the disk mid-plane in the accretion tongues. Therefore, we might assume that CTTSs that present periodic or quasi-periodic light curves (spot-like and AA Tau-like) are accreting in the stable regime, whereas those that present aperiodic light curves (dominated by flux bursts or extinction events) are accreting in the unstable regime.

It is important to remember that a CTTS's light curve morphology is not a permanent characteristic of that system, but rather a reflection of the system's current state, and as that system progresses through different phases of accretion and of its evolution, its light curve morphology will change accordingly. McGinnis et al. (2015) and Sousa et al. (2016) show that many of the CTTSs in NGC 2264 that were observed by CoRoT in both epochs suffered a transition from one light curve type to a different one in 2011. These transitions were usually between

spot-like and flux burst-dominated light curves or between AA Tau-like and aperiodic extinction-dominated light curves, and were attributed to a change in these systems' accretion regimes between the two observing runs. According to Kurosawa & Romanova (2013), some of the most important factors to determine in which regime a CTTS will accrete are mass accretion rate and the strength and topology of the stellar magnetic field. Systems undergoing a stable accretion regime tend to have lower mass accretion rates and more ordered magnetic fields, with stronger bipolar components, than those undergoing an unstable accretion regime. Therefore if any of these factors change over time, the CTTS may transition from one regime to another.

Figure 11 shows (in black) the average [OI] $\lambda$ 6300 line profiles of the different groups of our CTTSs that present [OI] $\lambda$ 6300 emission, separated according to their light curve morphology in both CoRoT epochs and according to whether they maintained a constant photometric behavior or transitioned between different classifications. Each profile was normalized by its maximum intensity before the average was taken. The individual normalized profiles are also shown (in gray), in order to highlight the diversity of the [OI] $\lambda$ 6300 line profiles in each group. We can see that stars that present AA Tau-like light curves in one or both CoRoT epochs show a narrow profile, with only a broad base or a modest blue wing, while stars that present aperiodic extinction in both CoRoT epochs show a much broader profile, with a more extended blue wing. In a similar fashion, stars with light curves dominated by flux bursts in both CoRoT epochs have a very broad profile and a clear blueshifted HVC with a distinct peak, whereas the stars with spot-like light curves in one epoch

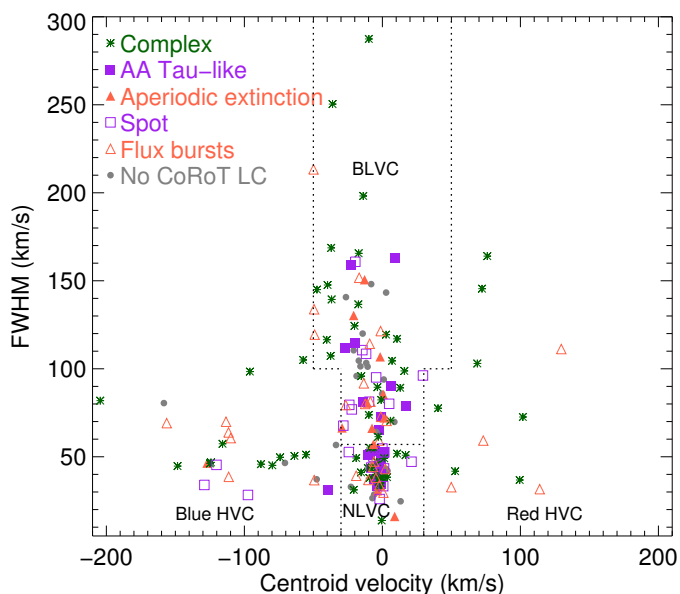


Fig. 12: Distribution of centroid velocities and FWHM of all components in our sample, with different colors and symbols representing different types of photometric variability. Purple symbols represent systems that showed a periodic behavior in one or both CoRoT observing runs, with filled squares corresponding to AA Tau-like systems and open squares to those with spot-like behavior. Orange symbols represent systems that were nonperiodic in both 2008 and 2011, with filled triangles corresponding to systems whose light curves are dominated by aperiodic extinction and open triangles to those dominated by flux bursts. Green asterisks represent light curves that were classified as complex. Dashed lines indicate approximately the separation between different components - narrow and broad LVC, red- and blueshifted HVC.

or another present a much weaker HVC, whether in the form of an extended blue wing or clearly separated from the LVC. This may be explained by the fact that the stars with very irregular, aperiodic photometric variability are often the ones with the highest mass accretion rates, especially those whose light curves are dominated by flux bursts (Sousa et al. 2016). These higher mass accretion rates would be connected to more intense jets and therefore stronger [OI] $\lambda$ 6300 emission line HVCs.

Figure 12 shows the distribution of centroid velocities and FWHM of all components in our sample, with different colors and symbols representing different types of photometric variability. This figure helps to illustrate how the HVC is much more often associated with systems that show irregular, nonperiodic variability (green and orange symbols), while systems that show periodic variability (purple symbols) usually present only low-velocity [OI] $\lambda$ 6300 emission. This becomes even clearer in the left panel of Fig. 13, which shows a histogram of light curve types for all systems in which the [OI] $\lambda$ 6300 line was detected (striped black bins) and for those that present a HVC (shaded gray bins). We can see that most ( $81_{-10}^{+5}\%$ ) of the systems with a HVC are associated with either light curves dominated by flux bursts or complex variability (compared with  $57\pm 5\%$  for the full [OI] $\lambda$ 6300 sample). A few systems are dominated by spot-like light curves, which are generally viewed at low inclinations (close to face-on), favorable to detect a HVC. Only very few objects with a HVC present AA Tau-like light curves or photometric variability attributed to aperiodic extinction events, which

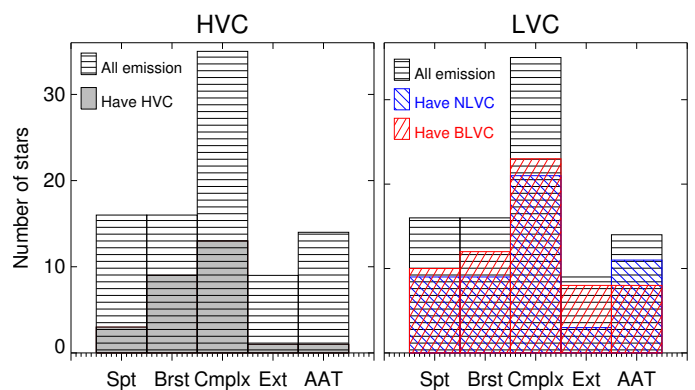


Fig. 13: Histogram of light curve types for the systems where [OI] $\lambda$ 6300 emission was detected (black striped bins), for those that present a HVC (left panel, shaded gray bins), for those that present a NLVC (right panel, blue), and for those that present a BLVC (right panel, red). The ordinate represents the number of systems that present each light curve type. From left to right, the bins represent systems with spot-like light curves in one or both CoRoT runs; systems with accretion burst-dominated light curves in both CoRoT runs; systems with complex light curves in both CoRoT runs; systems with aperiodic extinction-dominated light curves in both CoRoT runs; and systems that showed an AA Tau-like light curve in one or both CoRoT runs.

can be explained by the high system inclinations necessary to observe these phenomena, making it difficult to deconvolve the HVC from the LVC. Besides this geometrical effect, Fig. 13 shows us that the [OI] $\lambda$ 6300 line's HVC is indeed most often associated with irregular photometric behavior. Among the few systems with periodic (AA Tau-like or spot-like) light curves in which a HVC is found, this component is on average weaker than among the systems with complex or flux burst-dominated light curves. The periodic systems also present on average lower mass accretion rates and infrared excess than the other systems where a HVC is found. It seems that the occurrence of large-scale jets is not only more common among the sources accreting in the unstable regime, but is also stronger in these systems. The right panel of Fig. 13 shows that the LVC does not present a clear trend with photometric variability.

## 6. Discussion

### 6.1. Where does the low-velocity emission come from?

Emission originating in the disk is subject to broadening by Keplerian rotation, therefore if the narrow and broad components of the LVC come from disk winds, their widths can indicate at which disk radii they originate<sup>9</sup>. Since it is the rotation velocity projected in our line-of-sight that determines the observed width of a line, then the FWHM of the NLVC and BLVC should show strong trends with the system inclination, as was found by S16 for their sample. If Keplerian rotation is the only major source of line broadening for both the NLVC and BLVC, then there should be a correlation between their FWHM among systems where both were detected, since the system inclination should affect both components in a similar manner (S16). We find this correlation in our sample, as S16 find in theirs, with a Kendall  $\tau$  test

<sup>9</sup> Assuming that no other mechanism strongly affects the line broadening besides Keplerian rotation and the instrumental profile, which can easily be removed.

giving only a 0.2% probability of false correlation. Nevertheless, there is a significant spread in this relation, meaning that other factors besides the system inclination should be influencing the FWHM of one or both of these components.

In order to further investigate the region in the disk where the [OI] $\lambda$ 6300 emission originates, we must derive system inclinations. We do not have direct measurements of the inclinations of our systems, but we can estimate them from stellar rotation properties, using the relation  $v \sin i = (2\pi R_*/P_{rot}) \sin i$  (where  $v \sin i$  is the stellar rotation velocity projected in our line of sight,  $R_*$  is the stellar radius and  $P_{rot}$  the stellar rotation period). This method is subject to a number of uncertainties and the resulting inclinations are very inaccurate (see, e.g., Appenzeller & Bertout 2013, for a comparison between inclinations derived from rotation properties and those measured directly). Nevertheless, though direct imaging of disks should give much more accurate system inclinations, the inclinations provided are of the outer disk (beyond 10 au). In-depth studies of T Tauri and Herbig Ae/Be disks are beginning to show that a misalignment between the inner and outer disk is not a rare phenomenon (e.g., Marino et al. 2015; Loomis et al. 2017; Min et al. 2017). Using stellar rotation properties ensures that we are estimating the inclination of the inner disk, where [OI] $\lambda$ 6300 emission is believed to arise, though the accuracy is far from ideal.

To estimate inclinations, we used the periods obtained from the 2011 CoRoT light curves given in Venuti et al. (2017a) or the 2008 CoRoT light curves given in Alencar et al. (2010). Stellar radii were taken from Venuti et al. (2014), who compared locations on the HR diagram to pre-main sequence model grids of Siess et al. (2000). Values of  $v \sin i$  were measured directly in our FLAMES spectra by comparing to synthetic spectra (described in Sect. 3.1) of the closest effective temperature to the star's,  $\log g = 4$ , and broadened to the instrumental resolution of  $R = 26500$ . An extra continuum was added to simulate veiling and the synthetic spectrum was rotationally broadened, with both veiling and  $v \sin i$  adjusted simultaneously to minimize  $\chi^2$ .

Figure 14 shows the  $\text{FWHM}_{cor}/\sqrt{M_*}^{10}$  of the broad and narrow LVCs versus system inclinations, which describes the relation expected for Keplerian broadening and therefore indicates the region in the disk where each component originates (if the line width is dominated by Keplerian rotation, then the deprojected half width at half maximum corresponds to  $v_{Kep}(r_0) = \sqrt{GM_*/r_0}$ , where  $r_0$  is the emitting radius, so  $\text{FWHM}_{cor}/\sqrt{M_*} \propto (r_0)^{-1/2} * \sin i$ ). There is a smooth transition between the two components in this plot, with some overlap between them (though it is possible that the overlap may be caused partly by inaccurate inclination estimates). The sample of S16 also shows a smooth transition. In Fig. 14 we plot the data from S16 as open symbols in order to compare our results with theirs. We see that our data lie in the same region as theirs, though we do not find linear correlations between the  $\text{FWHM}_{cor}/\sqrt{M_*}$  of either component and inclinations as S16 did, possibly due to our large uncertainties in inclination.

Figure 14 suggests that most of the NLVCs in NGC 2264 originate between  $\sim 0.5$  au and  $\sim 5$  au, while most of the BLVCs seem to come from a region between  $\sim 0.05$  au and  $\sim 0.5$  au, in agreement with what S16 find in Taurus. For a small number of BLVCs, we infer launching radii  $< 0.05$  au, however the large uncertainty in inclination makes at least two of them compatible with 0.05 au. For the remaining two systems, their truncation radii could be located at  $\sim 0.02$  au if their stellar magnetic fields

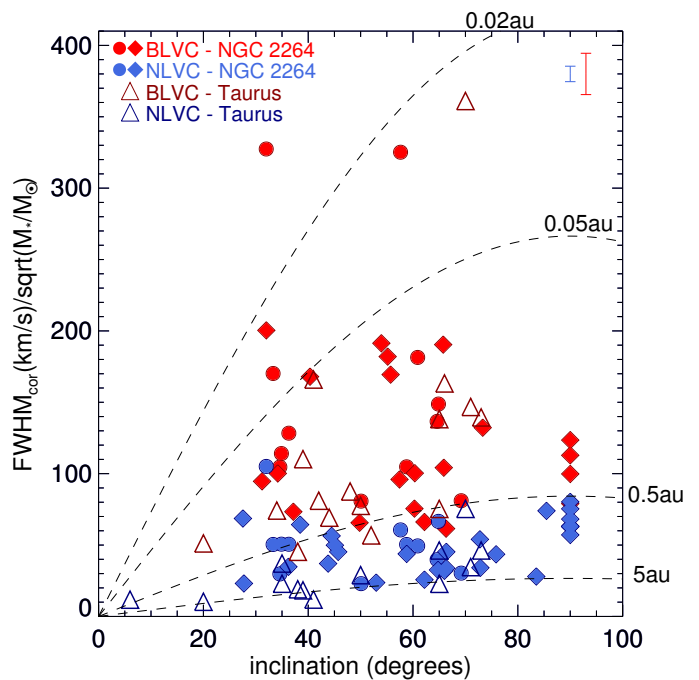


Fig. 14:  $\text{FWHM}_{cor}^{10}$  normalized by the square root of the stellar mass vs. inclination. Filled red symbols represent our broad LVCs, while filled blue symbols represent our narrow LVCs. Circles show cases where two LVCs were identified and diamonds show cases where only a BLVC or a NLVC was identified. Open symbols represent the data from S16, dark red for the BLVC and dark blue for the NLVC. Black dashed lines show line width as a function of inclination for Keplerian rotation at four different disk radii: 0.02 au, 0.05 au, 0.5 au, and 5 au (assuming that  $\text{FWHM} = 2v_{Kep}(r)$ ). Typical error bars on the ordinate are shown in the top left corner in blue and red for our NLVCs and BLVCs, respectively.

are on the order of 100 G, according to Equation 6 of Bessolaz et al. (2008). This is somewhat low for CTTSs, but not implausible. In any case, by disregarding any broadening mechanisms besides instrumental and Doppler broadening due to Keplerian rotation, we may be somewhat underestimating these inferred launching radii.

## 6.2. A comparison between the NLVC and photoevaporative disk wind models

Ercolano & Owen (2010) propose that the LVC of the [OI] $\lambda$ 6300 emission line may be produced in an X-ray driven photoevaporative disk wind. R13 argue against this, based on a number of reasons, such as the fact that these models could not reproduce the observed widths of the [OI] $\lambda$ 6300 LVCs. However, this was before the LVC was found to be composed of two components, one narrower than the other. In the work of S16, the broad component is shown to be consistent with an origin in an MHD disk wind, while the NLVC is investigated in the context of a photoevaporative disk wind, though they do not find enough evidence to confirm this as its origin. In this and the following section, we discuss whether the data from NGC 2264 supports or conflicts with this scenario.

It is interesting that in our sample a weak correlation is found between the luminosity of the [OI] $\lambda$ 6300 LVC and the X-ray luminosity, while both S16 and R13 find no such correlation.

<sup>10</sup>  $\text{FWHM}_{cor}$  represents the FWHM corrected to remove the instrumental profile and  $M_*$  is the stellar mass.

In Sect. 4.2 we have noted that the correlation with X-ray luminosity is strongest for the NLVC. Even if it is driven by an underlying correlation with the stellar luminosity, as was suggested in Sect. 4.2, this alone would not exclude the possibility that a photoevaporative disk wind may be the origin of the narrow component of the [OI] $\lambda$ 6300 line's LVC. Ercolano & Owen (2016) argue that a correlation between  $L_X$  and  $L_{[OI],LVC}$  is not necessarily expected, since the observed  $L_X$  traces mostly hard X-rays, while it is the soft X-rays that would be the main responsible for heating the gas in the [OI] $\lambda$ 6300 emitting region, as they are strongly absorbed and thus not detectable by X-ray observations.

The launching radii of the NLVC implied by Fig. 14 are compatible with the critical radius expected for photoevaporative winds (Alexander et al. 2014). This is confirmed by the updated photoevaporative disk wind model of Ercolano & Owen (2016). However, this model is still unable to reproduce the widths of the observed profiles. Using a very similar spectral resolution to ours, Ercolano & Owen (2016) produce [OI] $\lambda$ 6300 low-velocity profiles of  $14.36 \text{ km s}^{-1} < \text{FWHM} < 32.89 \text{ km s}^{-1}$  for a star of  $0.7 M_\odot$ , much narrower than most of the values we observe (more than half of our sample of NLVCs have FWHM larger than their upper limit).

Figure 15 shows the relation between the  $\text{FWHM}_{cor} / \sqrt{M_*}^{10}$  and centroid velocities of our observed NLVCs, along with the expected relation according to Ercolano & Owen (2016) for a photoevaporating disk wind model around a star of  $M_* = 0.7 M_\odot$ ,  $L_X = 2 \times 10^{30} \text{ erg/s}$ , and  $L_{acc} = L_{bol}$ , varying the system inclination from  $i = 0^\circ$  to  $i = 90^\circ$  (thick red line). As was noted in Sect. 3.4, we may be incomplete at  $\text{FWHM} < 25 \text{ km s}^{-1}$ , so we add the sample of S16 to this figure to better populate the lower region of this diagram (represented in Fig. 15 as blue triangles). We highlight the systems that are likely observed at high inclinations with regard to our line-of-sight (based on  $\sin i \gtrsim 1$  or extinction-dominated CoRoT light curves), since some of these low-velocity components may in fact be misclassified HVCs projected at low ( $v_c < 30 \text{ km s}^{-1}$ ) velocities (represented in Fig. 15 as purple diamonds). We see that the model does not agree well with the bulk of the distribution of  $\text{FWHM}_{cor} / \sqrt{M_*}^{10}$ , even if we ignore the components that may be misclassified. As for the centroid velocities, in total 43/64 (67%) of our values fall, within the  $1\sigma$  uncertainties, in the range of  $-5.1 \text{ km s}^{-1} \leq v_c \leq 0 \text{ km s}^{-1}$  that is expected from this model, and 58/64 (91%) fall in this range within  $3\sigma$ . Hence, most of the centroid velocities of our NLVCs are in agreement with theoretical expectations for photoevaporative disk winds, however we cannot exclude that a more efficient acceleration mechanism may be required for at least some of these systems (e.g., magneto-thermal disk winds, Béthune et al. 2017). In total, if we exclude the systems observed at high inclinations, we still find that nearly half of our sample of NLVCs (27/64) have a combination of FWHM and centroid velocity that cannot be reproduced by this model.

### 6.3. The BLVC as the base of high-velocity jets

The high blueshifts (up to nearly  $50 \text{ km s}^{-1}$ ) we find for the broad LVCs in our sample are compatible with disk winds of up to  $50 \text{ km s}^{-1}$  (assuming random system inclinations, the largest blueshifts likely arise from systems viewed closer to face-on, meaning that their centroid velocities may represent the maximum velocities of these disk winds). Figure 14 points to an origin in the innermost part of the disk, less than one au from the star, too close for a photoevaporative wind to arise. In this region of the disk the interaction with the stellar magnetosphere is

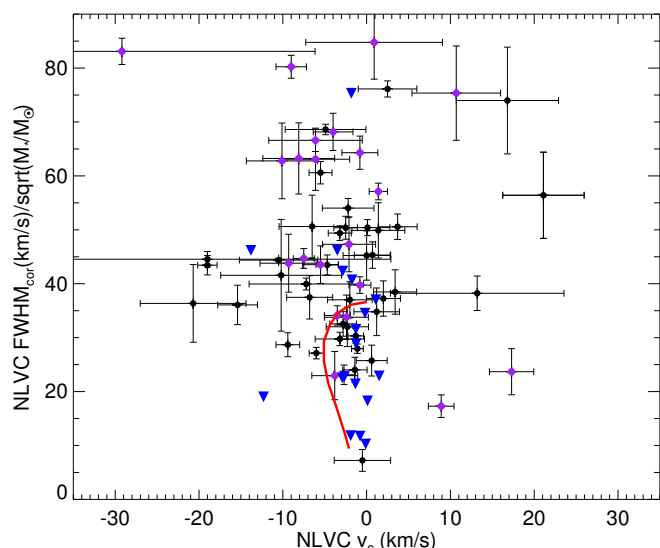


Fig. 15: Distribution of  $\text{FWHM}_{cor} / \sqrt{M_*}^{10}$  versus centroid velocities for the narrow LVCs in our sample (black dots) and in S16 (blue triangle), compared with theoretical expectations from Ercolano & Owen (2016) for a star of  $M_* = 0.7 M_\odot$ ,  $L_X = 2 \times 10^{30} \text{ erg/s}$ , and  $L_{acc} = L_{bol}$ , varying the system inclination from  $i = 0^\circ$  to  $i = 90^\circ$  (thick red line). Purple diamonds represent systems observed at high inclinations, therefore there could be misclassification of the components in their [OI] $\lambda$ 6300 line profile due to projection effects.

strongest, meaning this could represent emission coming from a magnetized inner disk wind, as was proposed by S16. The strong correlation we find between its luminosity and the accretion luminosity (stronger than the one found for all other components), besides the positive correlation S16 find between the FWHM of the BLVC and the accretion luminosity, suggest that accretion plays an important role in launching this wind.

The emitting region of the BLVC deduced from Fig. 14 is consistent with estimates of the launching region of protostellar jets (see, e.g., Tabone et al. 2017, who estimate from jet rotation a launching range of 0.05 to 0.3 au for the HH 212 SiO jet, and Anderson et al. 2003; Pesenti et al. 2004, who infer that the launching radius for DG Tau can extend up to  $\sim 3\text{au}$ ), leading us to speculate that the BLVC may be tracing the base of the same wind that is accelerating into a protostellar jet. The blueshifts of up to  $\sim 50 \text{ km s}^{-1}$  found for the BLVC would then represent the intermediate propagation velocity of a wind that is accelerating from  $0 \text{ km s}^{-1}$  to typical velocities of protostellar jets. We find that most ( $74^{+6}_{-9}\%$ ) of the systems where a HVC was detected also present a BLVC. If they are indeed connected, then we would expect to find a BLVC in all systems with a HVC. As discussed in Appendix A, our sample is likely subject to a sensitivity issue and may be incomplete. Therefore it is possible that these systems indeed present a BLVC that was unfortunately below our detection threshold.

If the BLVC represents the base of the jet traced by the HVC, then we may expect there to be a correlation between parameters of these two components among the systems that present both. However, we do not necessarily expect there to be a direct correlation between the FWHM of the two, since the HVC is dominated by jet emission on much larger scales from the source ( $\gtrsim 30 \text{ au}$ ), where collimation has been achieved. Its FWHM

is therefore likely dominated by turbulent and/or thermal processes, leading to a much narrower profile.

A relationship we could investigate is between the emitting region of the BLVC and the expected launching radius of the jet associated with the HVC. For a jet launched via a magneto-centrifugal wind from a Keplerian disk, [Blandford & Payne \(1982\)](#) argue that the maximum velocity of the jet should scale with the Keplerian velocity of the launching radius ( $r_0$ ) as  $v_{jet} = v_{Kep}(r_0) * \sqrt{(2\lambda - 3)}$ , where  $\lambda$  is the magnetic lever arm and  $v_{Kep}(r_0) = \sqrt{(GM_*/r_0)}$ . If Keplerian rotation is the main responsible for the broadening of the BLVC, then half of its FWHM, deconvolved from the instrumental profile, should correspond to the Keplerian velocity at the emitting radius projected in our line-of-sight. Therefore, if the BLVC originates in a disk wind that is the base of the HVC-emitting jet, then its FWHM would be equivalent to  $2v_{Kep}(r_0) * \sin i$  (where  $i$  is the system inclination), and this quantity should correlate with the HVC jet velocity.

We search for a correlation between the centroid velocities of the HVC (which correspond to the average jet velocities projected in our line-of-sight) and the BLVCs' FWHM deconvolved from the instrumental profile, but do not find a convincing one. We must keep in mind, however, that the system inclination would strongly interfere with any correlation that may exist, since the deprojected velocities are perpendicular to each other. Therefore this does not exclude the possibility that the BLVC may be connected to the base of the large scale jets traced by the HVC. Ideally we would search for a correlation between the deprojected velocities, but unfortunately we only have reliable estimates of system inclination for seven systems in which both a HVC and a BLVC were detected, which subjects this result to very low number statistics, and the uncertainties in inclination are large enough to mask any correlation. If there is indeed a connection between the two components, then the relation between the deprojected velocities of these seven systems gives an average value of  $\lambda \sim 4.5$ . In order to confirm this scenario, however, it is necessary to analyze a statistically significant sample of systems that present both components and have accurate measurements of system inclinations.

#### 6.4. Evolution of the LVC with the evolution of the disk

In our study, we have seen that the BLVC is much more common than the NLVC among systems with thick disks and rarer than the NLVC among systems with a thin inner disk (left and middle panels of Fig. 9). The overall detection rate of the BLVC among accreting TTs in our sample decreases from  $50 \pm 5\%$  in the optically thick range of the  $\alpha_{IRAC}$  index, to  $28^{+10}_{-7}\%$  in the range considered to have anemic disks, to only  $6^{+11}_{-2}\%$  in the range that would be classified as a naked photosphere based only on  $\alpha_{IRAC}$ . On the other hand, the NLVC has a lower detection rate among systems with optically thick disks ( $29 \pm 4\%$ ) than among those with anemic disks ( $41 \pm 9\%$ ), and its detection rate decreases again to  $12^{+12}_{-4}\%$  in the most optically thin range. This is in agreement with S16, who show that the NLVC is often present among systems with transition disks, whereas the BLVC rarely is. In our sample, the NLVC is also more common among transition disk systems than the BLVC. Among the 13 transition disk systems (Alana Sousa, private communication) with a detected [OI] $\lambda$ 6300 line, seven show only a NLVC, three show both a NLVC and a BLVC, and only three show a BLVC alone. This can be seen in Fig. 16, which shows the ratio of the broad

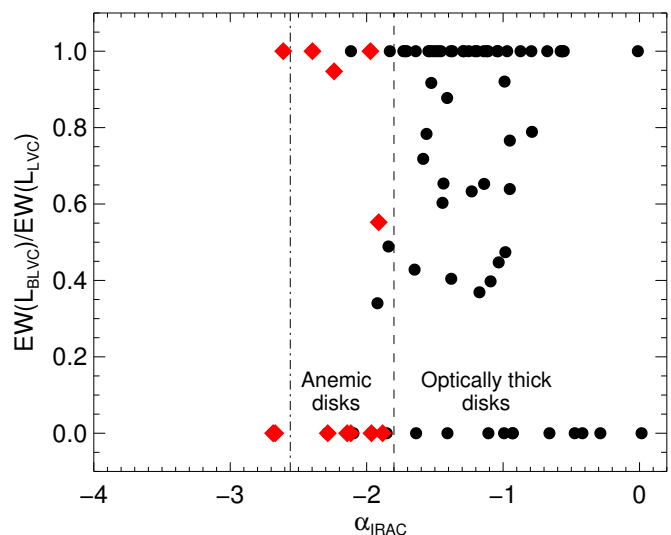


Fig. 16: Ratio of the [OI] $\lambda$ 6300 BLVC equivalent width to the equivalent width of the total LVC versus the  $\alpha_{IRAC}$  index. Transition disk sources are shown as red filled diamonds, while all other sources are shown as black filled circles.

component's equivalent width to the equivalent width of the total LVC versus  $\alpha_{IRAC}$ .

These results support the scenario proposed by S16 and discussed by [Ercolano & Pascucci \(2017\)](#) of an evolution of the [OI] $\lambda$ 6300 line profile with the evolution of the disk. In this scenario, the broad LVC disappears as the inner disk evolves and, as an inner hole is formed, the narrow LVC tends to dominate the [OI] $\lambda$ 6300 line profile. Since it has been shown that the BLVC originates closer to the central object than the NLVC (Fig. 14), this points to an inside-out gas dissipation of the inner disk. Even among the transition disk sources that still present a BLVC, their inferred launching regions are all consistent with originating beyond 0.2 au from the central object. This is close to the upper limit for the BLVC and therefore consistent with an inside-out clearing of the inner disk.

[Ercolano & Owen \(2010\)](#) predict that, if the [OI] $\lambda$ 6300 emission comes from a photoevaporative disk wind, then this emission would be approximately twice as luminous among sources with transition disks than among sources with primordial disks. If the NLVC traces such a photoevaporative wind and the BLVC traces an inner MHD disk wind, then we could expect to detect much stronger NLVCs than BLVCs as the systems evolve. However, in our sample alone, we do not see a tendency of the NLVC luminosity with the clearing of the inner dust disk (left panel of Fig. 9).

#### 6.5. The high-velocity component: testing launching models

In order to investigate which properties of the star-disk system may be connected to the mechanism that drives protostellar jets, we search for trends between these properties and the [OI] $\lambda$ 6300 HVC. However, the expected correlations for models of jet launching via stellar or magnetospheric winds often involve not one stellar parameter, but a complex combination of them. To properly explore this issue, it is necessary to delve into the theoretical background of the possible jet launching mechanisms, which is not the scope of this paper. We therefore discuss here only the general trends found in our sample, and reserve

a more thorough analysis of the HVC origin from a statistical viewpoint to a forthcoming paper, in which we will also include results from other star forming regions in order to increase the size of our sample.

We first analyzed the relationship between the luminosity of the HVC of the [OI] $\lambda$ 6300 line and stellar and accretion properties. Figure 17 shows the HVC luminosity versus stellar mass, on the left, and versus mass accretion rates, on the right. We plot in this Fig. only the mass accretion rates derived from the UV excess and not the values derived from the H $\alpha$  equivalent widths, in order to compare a more self-consistent sample<sup>11</sup>. We find no direct correlation between the HVC luminosity and stellar mass. The left panel of Fig. 17 shows an apparently bimodal behavior: some of the stars have [OI] $\lambda$ 6300 HVC luminosities that fall in the same range as many of the upper limits of nondetections, while another group shows higher luminosities that are nearly constant among the entire mass range, with  $\log L_{HVC}/L_{\odot} \sim -4.7$ . The right panel, on the other hand, shows that there is a relation between the [OI] $\lambda$ 6300 HVC and mass accretion, as has already been established here through the correlation between HVC luminosity and accretion luminosity in Sect. 4.2 and in other papers (Cabrit et al. 1990, HEG95). However, there is not a clear threshold between the two groups identified in the left panel. It is possible that these groups represent two slightly different populations that coexist in this star forming region, as other studies have found evidence of multiple substructures and subpopulations in NGC 2264 (Venuti et al. 2017b). However, we find no significant difference between the ages, radial velocities, or spatial distribution of the two groups we observe. We are, nonetheless, subject to low number statistics, therefore we cannot necessarily rule out this possibility.

In order to relate jet velocities with stellar and accretion parameters, we calculated the deprojected jet velocities from the HVC centroid velocities and from estimates of inclinations derived from stellar rotation properties in Sect. 6.1. We assume that the centroid velocity of the [OI] $\lambda$ 6300 emission line's HVC represents the average propagation velocity of the jet responsible for the emission, projected in our line-of-sight. Since the jet is perpendicular to the accretion disk, then the deprojected jet velocity ( $v_{jet}$ ) is the HVC centroid velocity divided by the cosine of the system inclination ( $v_{c,HVC}/\cos i$ ). We recall that deriving system inclinations from stellar rotation properties is subject to large uncertainties, therefore our values of jet velocity are also very imprecise. We find deprojected jet velocities mostly in the range  $100 \text{ km s}^{-1} < v_{jet} < 200 \text{ km s}^{-1}$ . Within the uncertainties they all agree with the average value of  $v_{jet} = 140(\pm 76) \text{ km s}^{-1}$ . It is therefore unclear if the large spread we observe in  $v_{jet}$  is due to an intrinsic spread in jet velocities across our sample or to the large uncertainties in deriving inclinations. We can also estimate the average jet velocity independently of inclination estimates by taking the median and standard deviation HVC peak velocity of  $v_c = 97.4(\pm 38.8) \text{ km s}^{-1}$  (found when considering both red and blueshifted HVCs), and deprojecting this value considering a median system inclination of  $60^\circ$ . This gives us  $v_{jet} = 195(\pm 78) \text{ km s}^{-1}$  for our sample, slightly larger than our first estimate and in agreement with the average jet veloc-

ity of  $v_{jet} = 196(\pm 16) \text{ km s}^{-1}$  found in Taurus by Appenzeller & Bertout (2013) from resolved [NII] lines.

We searched for correlations between the deprojected jet velocities and stellar properties such as effective temperature, mass and rotation rate, and found none. It is important to note, nevertheless, that our very large error bars may be masking possible trends. Appenzeller & Bertout (2013), who used direct measurements of inclination for a number of stars in Taurus, also searched for correlations between jet velocities and various stellar properties (escape velocities, photospheric radii, rotation periods, magnetic field data, spectral veiling, mass accretion rates and mass loss rates) and found no convincing correlations, except with the mass loss rate.

The occurrence of a HVC seems to be independent of the stellar rotation rate. Figure 18 shows a histogram of the rotation rates (normalized by break-up rates) of all of the CTTs in our sample, of those that have detected [OI] $\lambda$ 6300 emission but show no HVC, and of those for which an [OI] $\lambda$ 6300 HVC was detected. We can see in this figure that the HVCs are mostly associated with slow rotators ( $0.02 \lesssim v_{rot}/v_{brk} \lesssim 0.06$ ) but a KS test shows that their distribution is not statistically different than the distribution for sources without a HVC. This suggests that stellar rotation alone may not play a key role in launching jets and that an extra energy source, namely the tapping of accretion power, is required.

One last aspect we wish to investigate is the detection of jets among sources of different internal structures, and therefore likely possessing different stellar magnetic field topologies, as a star's magnetic field configuration is believed to change considerably as its internal structure changes. It seems that the stellar magnetic field increases in complexity and the dipole component decreases in strength as a radiative core develops, as argued by Gregory et al. (2012) for accreting T Tauri stars and Fig. 12 of Hill et al. (2017) for young stars. While fully convective stars have substantial dipolar components of 0.3 to a few KG, no strong dipolar component above a few tenths of a kG has yet been detected for  $M_{core}/M_* \gtrsim 0.4$  or  $T_{eff} \gtrsim 4500\text{K}$ , however it is unclear if this is due to a true evolution or to the current low number statistics. The limit of  $M_{core}/M_* \approx 0.4$  is empirical and more observations are required to confirm, and properly determine, the exact boundary.

Figure 19 shows that our sample contains many sources whose position on the HR diagram indicates that they should be fully convective (right of the green lines in Fig. 19), and also a number of sources in the region where a significant radiative core is expected to have developed (the left of the green lines in Fig. 19 corresponds to the region where  $M_{core}/M_* \gtrsim 0.4$ , according to Gregory et al. 2012). We do not see a difference in the fraction of stars with detected [OI] $\lambda$ 6300 HVC to stars with detected [OI] $\lambda$ 6300 emission ( $N(\text{HVC})/N([\text{OI}]) = 29_{-5}^{+6}\%$ ) and the range where a significant ( $\gtrsim 0.4M_*$ ) radiative core is expected to have developed ( $N(\text{HVC})/N([\text{OI}]) = 30_{-7}^{+10}\%$ ). If there truly is an evolution of the stellar magnetic field topology in this region of the HR diagram, then this result shows that the topology of the stellar magnetic field does not strongly affect the occurrence of protostellar jets and that kG-order dipoles are not necessary to launch them.

Villebrun et al. (2016) show that stellar magnetic fields of strength  $\gtrsim 200\text{G}$  are commonly detected in T Tauri stars and Herbig Ae/Be stars of effective temperatures up to around 6000K, beyond which very few magnetic stars are found. Our sample does not probe well the region beyond this threshold, so we cannot fully exclude the influence of stellar magnetic fields

<sup>11</sup> Determining mass accretion rates using these two different methods leads to slightly different values (see e.g., Sousa et al. 2016). UV excess is a more direct measurement of accretion, since the H $\alpha$  line can have contributions from a wind and from accretion shocks, and does not necessarily originate only in accretion columns as is normally assumed when estimating  $\dot{M}_{acc}$ , whereas the UV excess originates only in the accretion shocks.

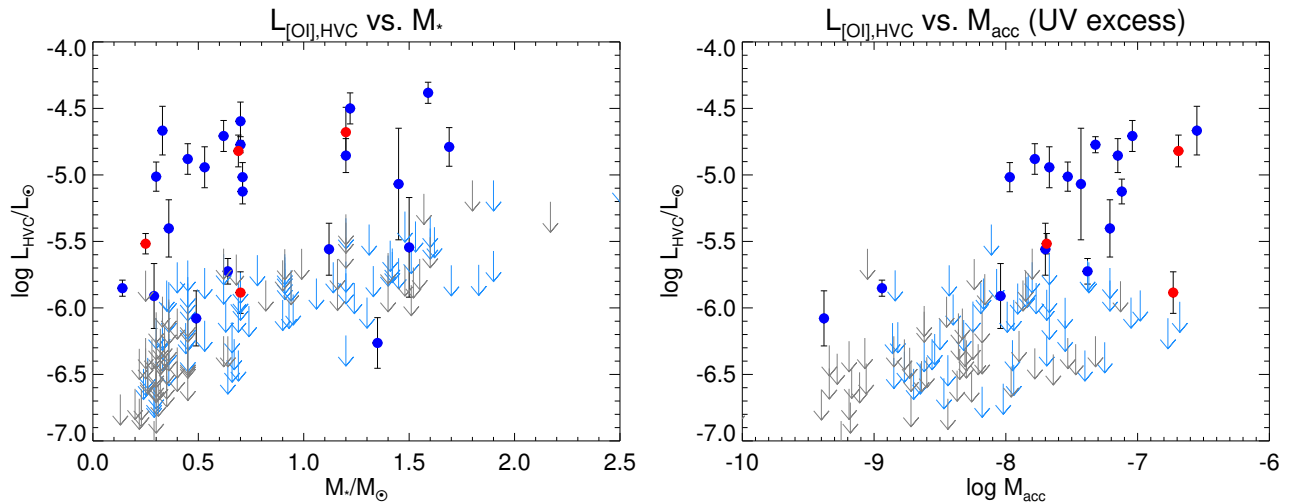


Fig. 17: [OI]λ6300 HVC luminosity versus stellar mass (left) and mass accretion rate derived from the UV excess (right). Gray arrows represent upper limits for [OI]λ6300 line luminosities when no emission in [OI]λ6300 was detected, while light blue arrows represent upper limits for HVC luminosities when only low-velocity [OI]λ6300 emission was detected. Blue filled circles represent blueshifted HVCs, while red filled circles represent redshifted HVCs (systems that did not present a blueshifted component). Luminosities of redshifted HVCs should be considered as lower limits, since the redshifted part of the jet suffers additional extinction from the circumstellar disk.

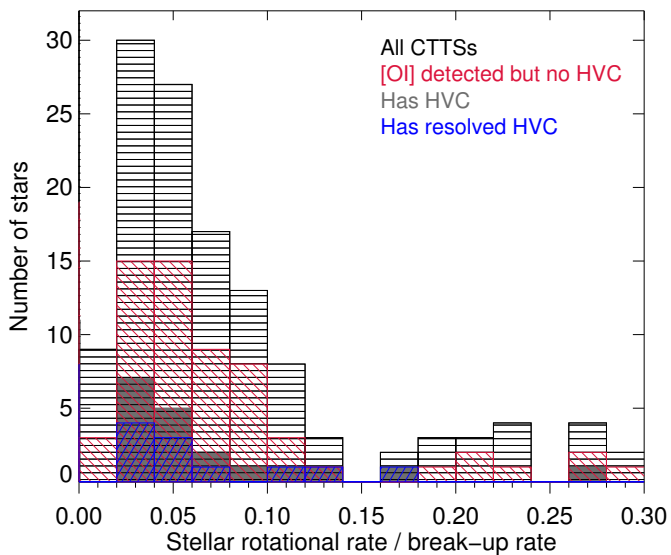


Fig. 18: Distribution of rotation rates as a fraction of break-up rate for all CTTSs (black), stars with [OI]λ6300 emission but no HVC (red), stars with a HVC (gray) and stars with a spectrally resolved HVC (blue).

in launching jets. We can however conclude from Figure 19 that, if stellar magnetic fields are necessary to power protostellar jets, then fields of a few 100G are sufficient to do so.

## 7. Summary and conclusions

We have searched for [OI]λ6300 emission in the spectra of 182 CTTSs and two HAeBe stars in the young, open cluster and well-known star forming region NGC 2264. We calculated the luminosity of these emission line profiles in order to compare them with previously determined stellar and accretion properties. We also compared the [OI]λ6300 line profiles of different groups

separated according to their CoRoT light curve morphologies, in order to analyze the relation between photometric variability and [OI]λ6300 emission. In this section, we emphasize our main results.

We detected [OI]λ6300 emission in 108 CTTSs and two HAeBe stars. Our detection rate among accreting T Tauri stars is low (59%) compared to previous studies of this forbidden emission line and decreases toward lower masses, reaching only 40% for  $M_* \leq 0.5M_\odot$  (for  $M_* > 0.5M_\odot$  this rate is 75%). We find no statistical difference between the ages or radial velocities of the systems in which we detect [OI]λ6300 and those in which we do not. Since other studies have detected [OI]λ6300 emission in stars of similar  $L_*$  and  $\dot{M}_{\text{acc}}$  as ours and find [OI]λ6300 line luminosities in the same range as the upper limits of our nondetections, we are led to believe that our low detection rate is likely due to a sensitivity issue.

A Gaussian decomposition of our [OI]λ6300 line profiles led us to identify up to four different components: a narrow low-velocity component (NLVC), a broad low-velocity component (BLVC), a blueshifted high-velocity component (HVC), and a redshifted HVC. The NLVC was detected in 64 stars (among 184 CTTSs and HAeBe stars analyzed), with an average FWHM of  $41.6(\pm 10.6)$  km s<sup>-1</sup> and centroid velocity ( $v_c$ ) of  $-3.5(\pm 9.1)$  km s<sup>-1</sup>. The BLVC was detected in 75 stars, with an average FWHM of  $112.5(\pm 41.7)$  km s<sup>-1</sup> and average  $v_c$  of  $-12.4(\pm 16.5)$  km s<sup>-1</sup>. The HVC was detected in 31 stars, 20 of which showed only a blueshifted HVC, 4 only a redshifted HVC, and 7 showed both a red- and blueshifted HVC. The average HVC has a FWHM of  $61.7(\pm 31.2)$  km s<sup>-1</sup> and  $|v_c|$  of  $94.3(\pm 38.8)$  km s<sup>-1</sup>. Both LVCs appear to be more blueshifted when a HVC is present.

The luminosities of both LVCs and of the HVC all correlate with the stellar luminosity  $L_*$  and with the accretion luminosity  $L_{\text{acc}}$ . The luminosity of the HVC does not correlate with the stellar X-ray luminosity  $L_X$ , but the luminosities of the NLVC and the BLVC weakly do. The luminosities of both the NLVC and BLVC also correlate positively with the UV flux. However, these correlations with X-ray luminosity and UV flux disappear

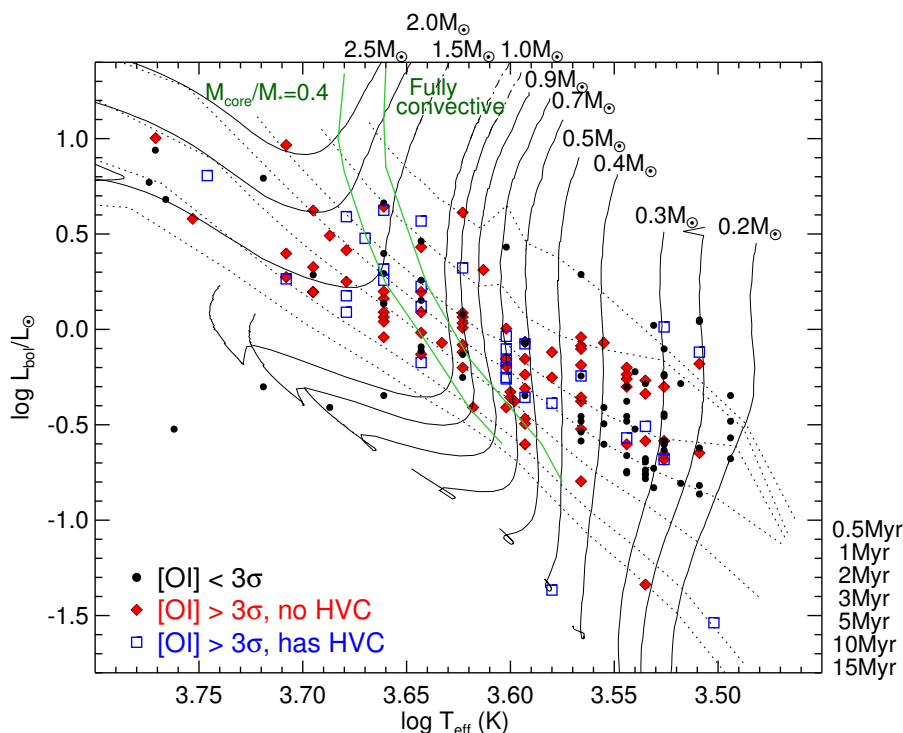


**Fig. 19.** HR diagram of the CTTs in our sample where no emission was detected (black dots), those with detected [OI] $\lambda$ 6300 emission but no HVC (red diamonds), and those with a HVC (blue squares). Solid and dotted black lines represent mass tracks and isochrones, respectively, of Siess et al. (2000). Solid green lines separate the regions in which a star is expected to be fully convective (right) and possess a radiative core of  $M_{\text{core}} > 0.4 M_{\odot}$  (left), according to Gregory et al. (2012).

after normalizing by the stellar luminosity  $L_{\star}$ , and thus could be driven by an underlying correlation with  $L_{\star}$ .

We find that systems that present aperiodic photometric variability, especially those dominated by flux bursts, tend to present stronger and more frequent HVCs than systems that show periodic (spot-like or AA Tau-like) behavior, whose [OI] $\lambda$ 6300 line profiles are usually dominated by the LVC. These aperiodic light curves have been associated with stars accreting in an unstable regime, which generally present higher mass accretion rates and more complex stellar magnetic fields than those accreting in a stable regime. We also find that systems whose light curves are dominated by stable spots or flux bursts show much more pronounced HVCs in their [OI] $\lambda$ 6300 line profile, often with a resolved peak, than the ones with light curves dominated by AA Tau-like or aperiodic flux dips. This is consistent with a scenario in which the latter are viewed at much higher inclinations than the former, as was proposed when interpreting these light curve classifications (e.g., McGinnis et al. 2015).

Assuming that the LVC broadening is dominated by Keplerian rotation, we infer launching radii between 0.05 au and 0.5 au for the BLVC and between 0.5 au and 5 au for the NLVC. This is the same as what S16 find for their sources in Taurus. The centroid velocities of the NLVCs in our sample are in reasonable agreement with current photoevaporative disk winds models (Ercolano & Owen 2016), however the FWHM of at least 42% (27/64) of the NLVCs in our sample cannot be reproduced by these models. Meanwhile, the larger blueshifts and FWHM of our BLVCs are much more consistent with inner disk winds. These winds may represent the base of the same winds that accelerate and collimate on larger scales, to form the HVC jets, but no concluding evidence was found to support this hypothesis. It is necessary to study a large sample of systems that present both the BLVC and HVC and have accurate system inclination measurements, in order to confirm this scenario.

We detected a HVC in the [OI] $\lambda$ 6300 line only among objects with significant infrared excess ( $K - 3.6\mu\text{m} > 0.3$ ), as was noted also by HEG95. This shows that it is necessary for

the system to have an optically thick inner disk in order to be able to power strong bipolar jets, from which this component is emitted. The NLVC, on the other hand, was detected in many sources with optically thin inner disks ( $K - 3.6\mu\text{m}$  down to 0 and  $\alpha_{\text{IRAC}}$  indices that would classify the systems as naked photospheres), while the BLVC is much more common among thick disk systems than among those with anemic disks, indicating that as the disk evolves, the BLVC disappears and the NLVC tends to dominate the [OI] $\lambda$ 6300 emission. The evolution of the [OI] $\lambda$ 6300 line profile with disk evolution is also demonstrated by the higher detection of NLVCs than BLVCs among systems with transition disks (also observed by S16 in Taurus). Since the BLVC has been shown to originate closer to the star than the NLVC, these findings support the scenario of inside-out gas dissipation in the inner disk.

The maximum velocities of the jets in our sample do not correlate with any stellar or accretion properties. We are, however, subject to large uncertainties because of the lack of directly measured system inclinations and to low number statistics, so we cannot exclude the possibility that a correlation may exist, masked within the uncertainties. The average deprojected jet velocity in our sample is  $v_{\text{jet}} = 140(\pm 76) \text{ km s}^{-1}$ , which agrees with the average jet velocities measured in the younger star forming region Taurus ( $196 \pm 16 \text{ km s}^{-1}$ , according to Appenzeller & Bertout 2013).

The HVC was detected across the full T Tauri range of the HR diagram, with no apparent difference in the detection rates among stars that should be fully convective and those that have probably already developed a significant radiative core ( $M_{\text{core}} > 0.4 M_{\odot}$ ), suggesting that the topology of the stellar magnetic field may not play a significant role in the jet launching process. It is important to confirm this with proper mapping of stellar magnetic fields and to extend this study to larger stellar masses, where a significant drop of stellar magnetic field detection has been shown to occur.

*Acknowledgements.* The authors acknowledge the anonymous referee for their contribution to the quality of this paper. We thank E. Flaccomio for provid-

ing us with X-ray luminosities and A.P. Sousa for information on transition disks. P.M. would like to thank M. Guimarães for helpful discussions and the physics department at the Universidade Federal de Sergipe, Brazil, for support during visits. This work is based on data products from observations made with ESO Telescopes under program ID 094.C-0467(A). This work was partly supported by CAPES, within the CAPES/Cofecub program, and by FAPEMIG under grant number 23893. P.M. and S.H.P.A also acknowledge financial support from CNPq.

## References

- Alencar, S. H. P., Teixeira, P. S., Guimarães, M. M., et al. 2010, *A&A*, 519, A88 [5](#), [6.1](#), [C.2](#)
- Alexander, R., Pascucci, I., Andrews, S., Armitage, P., & Cieza, L. 2014, *Protostars and Planets VI*, 475 [1](#), [6.2](#)
- Anderson, J. M., Li, Z.-Y., Krasnopolsky, R., & Blandford, R. D. 2003, *ApJL*, 590, L107 [6.3](#)
- Appenzeller, I. & Bertout, C. 2013, *A&A*, 558, A83 [6.1](#), [6.5](#), [7](#)
- Bessolaz, N., Zanni, C., Ferreira, J., Keppens, R., & Bouvier, J. 2008, *A&A*, 478, 155 [6.1](#)
- Béthune, W., Lesur, G., & Ferreira, J. 2017, *A&A*, 600, A75 [6.2](#)
- Blandford, R. D. & Payne, D. G. 1982, *MNRAS*, 199, 883 [6.3](#)
- Blinova, A. A., Romanova, M. M., & Lovelace, R. V. E. 2016, *MNRAS*, 459, 2354 [5](#)
- Bouvier, J., Alencar, S. H. P., Bouvier, T., et al. 2007, *A&A*, 463, 1017 [5](#)
- Bouvier, J., Chelli, A., Allain, S., et al. 1999, *A&A*, 349, 619 [5](#)
- Cabrit, S. 2002, in *EAS Publications Series*, Vol. 3, *EAS Publications Series*, ed. J. Bouvier & J.-P. Zahn, 147–182 [1](#)
- Cabrit, S., Edwards, S., Strom, S. E., & Strom, K. M. 1990, *ApJ*, 354, 687 [1](#), [3.1](#), [4.2](#), [6.5](#)
- Cody, A. M., Stauffer, J., Baglin, A., et al. 2014, *AJ*, 147, 82 [1](#), [2](#), [2](#), [4.1](#), [5](#), [C.2](#)
- Dahm, S. E. 2008, *The Young Cluster and Star Forming Region NGC 2264*, ed. B. Reipurth, 966 [1](#)
- Dahm, S. E. & Simon, T. 2005, *AJ*, 129, 829 [3.1](#), [1](#), [4.1](#), [C.1](#), [C.2](#)
- Ercolano, B. & Owen, J. E. 2010, *MNRAS*, 406, 1553 [1](#), [6.2](#), [6.4](#)
- Ercolano, B. & Owen, J. E. 2016, *MNRAS*, 460, 3472 [1](#), [6.2](#), [15](#), [7](#)
- Ercolano, B. & Pascucci, I. 2017, *Royal Society Open Science*, 4, 170114 [4.2](#), [6.4](#)
- Fang, M., van Boekel, R., Wang, W., et al. 2009, *A&A*, 504, 461 [4.2](#)
- Ferreira, J., Dougados, C., & Cabrit, S. 2006, *A&A*, 453, 785 [1](#)
- Font, A. S., McCarthy, I. G., Johnstone, D., & Ballantyne, D. R. 2004, *ApJ*, 607, 890 [1](#)
- Gillen, E., Aigrain, S., McQuillan, A., et al. 2014, *A&A*, 562, A50 [1](#), [4.1](#)
- Gorti, U., Hollenbach, D., Najita, J., & Pascucci, I. 2011, *ApJ*, 735, 90 [1](#)
- Gregory, S. G., Donati, J.-F., Morin, J., et al. 2012, *ApJ*, 755, 97 [6.5](#), [19](#)
- Guarcello, M. G., Flaccomio, E., Micela, G., et al. 2017, *A&A*, 602, A10 [4.2](#)
- Hartigan, P., Edwards, S., & Ghandour, L. 1995, *ApJ*, 452, 736 [1](#)
- Hill, C. A., Carmona, A., Donati, J.-F., et al. 2017, *MNRAS*, 472, 1716 [6.5](#)
- Isobe, T., Feigelson, E. D., & Nelson, P. I. 1986, *ApJ*, 306, 490 [4.2](#)
- Kulkarni, A. K. & Romanova, M. M. 2008, *MNRAS*, 386, 673 [5](#)
- Kupka, F., Piskunov, N., Ryabchikova, T. A., Stempels, H. C., & Weiss, W. W. 1999, *A&AS*, 138, 119 [3.1](#)
- Kupka, F. G., Ryabchikova, T. A., Piskunov, N. E., Stempels, H. C., & Weiss, W. W. 2000, *Baltic Astronomy*, 9, 590 [3.1](#)
- Kurosawa, R. & Romanova, M. M. 2013, *MNRAS*, 431, 2673 [5](#)
- Kwan, J. & Tademaru, E. 1995, *ApJ*, 454, 382 [1](#)
- Lada, C. J., Muench, A. A., Luhman, K. L., et al. 2006, *AJ*, 131, 1574 [4.2](#)
- Lavalley, M. P., Isobe, T., & Feigelson, E. D. 1992, in *BAAS*, Vol. 24, *Bulletin of the American Astronomical Society*, 839–840 [4.2](#)
- Loomis, R. A., Öberg, K. I., Andrews, S. M., & MacGregor, M. A. 2017, *ApJ*, 840, 23 [6.1](#)
- Marino, S., Perez, S., & Casassus, S. 2015, *ApJL*, 798, L44 [6.1](#)
- McGinnis, P. T., Alencar, S. H. P., Guimarães, M. M., et al. 2015, *A&A*, 577, A11 [4](#), [5](#), [7](#)
- Min, M., Stolker, T., Dominik, C., & Benisty, M. 2017, *A&A*, 604, L10 [6.1](#)
- Natta, A., Testi, L., Alcalá, J. M., et al. 2014, *A&A*, 569, A5 [1](#)
- Nisini, B., Antonucci, S., Alcalá, J. M., et al. 2018, *A&A*, 609, A87 [1](#)
- Pascucci, I., Sterzik, M., Alexander, R. D., et al. 2011, *ApJ*, 736, 13 [1](#)
- Pasquini, L., Avila, G., Blecha, A., et al. 2002, *The Messenger*, 110, 1 [2](#)
- Peñati, N., Dougados, C., Cabrit, S., et al. 2004, *A&A*, 416, L9 [6.3](#)
- Piskunov, N. E., Kupka, F., Ryabchikova, T. A., Weiss, W. W., & Jeffery, C. S. 1995, *A&AS*, 112, 525 [3.1](#)
- Porter, J. M., Oudmaijer, R. D., & Baines, D. 2004, *A&A*, 428, 327 [B](#), [B](#)
- Ray, T., Dougados, C., Bacciotti, F., Eisloffel, J., & Chrysostomou, A. 2007, *Protostars and Planets V*, 231 [1](#)
- Rebull, L. M., Makidon, R. B., Strom, S. E., et al. 2002, *AJ*, 123, 1528 [3.1](#), [4.1](#), [C.1](#), [C.2](#)
- Rigliaco, E., Pascucci, I., Gorti, U., Edwards, S., & Hollenbach, D. 2013, *ApJ*, 772, 60 [1](#)
- Romanova, M. M., Kulkarni, A. K., & Lovelace, R. V. E. 2008, *ApJL*, 673, L171 [5](#)
- Romanova, M. M., Ustyugova, G. V., Koldoba, A. V., & Lovelace, R. V. E. 2013, *MNRAS*, 430, 699 [5](#)
- Ryabchikova, T. A., Piskunov, N. E., Kupka, F., & Weiss, W. W. 1997, *Baltic Astronomy*, 6, 244 [3.1](#)
- Siess, L., Dufour, E., & Forestini, M. 2000, *A&A*, 358, 593 [6.1](#), [19](#), [A.1](#)
- Simon, M. N., Pascucci, I., Edwards, S., et al. 2016, *ApJ*, 831, 169 [1](#)
- Sousa, A. P., Alencar, S. H. P., Bouvier, J., et al. 2016, *A&A*, 586, A47 [1](#), [4.1](#), [5](#), [11](#)
- Stauffer, J., Cody, A. M., Baglin, A., et al. 2014, *AJ*, 147, 83 [5](#)
- Stauffer, J., Cody, A. M., Rebull, L., et al. 2016, *AJ*, 151, 60 [5](#)
- Sung, H., Bessell, M. S., & Lee, S.-W. 1997, *AJ*, 114, 2644 [1](#), [4.1](#)
- Tabone, B., Cabrit, S., Bianchi, E., et al. 2017, *A&A*, 607, L6 [6.3](#)
- Valenti, J. A. & Piskunov, N. 1996, *A&AS*, 118, 595 [3.1](#)
- Venuti, L., Bouvier, J., Cody, A. M., et al. 2017a, *A&A*, 599, A23 [6.1](#), [C.2](#)
- Venuti, L., Bouvier, J., Flaccomio, E., et al. 2014, *A&A*, 570, A82 [1](#), [2](#), [3.1](#), [3.1](#), [1](#), [4.1](#), [4.2](#), [4.2](#), [6.1](#), [A](#), [C.1](#), [C.2](#)
- Venuti, L., Prisinzano, L., Sacco, G. G., et al. 2017b, submitted to *A&A* [1](#), [6.5](#)
- Villebrun, F., Alecian, E., Bouvier, J., Hussain, G., & Folsom, C. P. 2016, in *SF2A-2016: Proceedings of the Annual meeting of the French Society of Astronomy and Astrophysics*, ed. C. Reylé, J. Richard, L. Cambrésy, M. Deleuil, E. Pécontal, L. Tresse, & I. Vauglin, 199–202 [6.5](#)
- Walker, M. F. 1956, *ApJS*, 2, 365 [3.1](#), [C.1](#), [C.2](#)

## Appendix A: Completion

As has been mentioned throughout this work, our detection of the [OI] $\lambda$ 6300 emission line is much lower among CTTSs than in previous studies (we find a detection rate of 59%, compared to 100% in HEG95, 84% in N14, 91% in S16 and 77% in N18). On the one hand, the sample studied by HEG95 (and R13, who obtained modern estimates of accretion luminosities for this sample) was composed of stars with on average higher mass accretion rates than ours, which could explain their much higher detection rate<sup>12</sup>. Among stars of  $L_{acc} > 10^{-2.6}L_{\odot}$  (where 90% of their sample lies), our detection rate is 69%. This is much higher than the global detection rate we find, but still lower than HEG95, who detected the [OI] $\lambda$ 6300 line in all CTTSs analyzed. On the other hand, N14 analyzed a sample of CTTSs with lower mass accretion rates than ours and still found a 91% detection rate in the [OI] $\lambda$ 6300 line among CTTSs, meaning that mass accretion rates alone cannot account for our low detection rate.

Our global detection rate of the [OI] $\lambda$ 6300 emission line is not constant throughout the HR diagram, but is much higher in the upper left portion and decreases toward lower effective temperatures (see Fig. A.1). Among stars of  $M_{*} \leq 0.5M_{\odot}$  (or  $T_{eff} \lesssim 3800K$ ) the detection rate is only 40% (32/80), while for stars of  $M_{*} > 0.5M_{\odot}$  ( $T_{eff} \gtrsim 3800K$ ) it is 75% (78/104). This could be the result of an observational bias if the cooler stars tend to present emission of lower intensity compared to the level of noise in their spectra, which fall below our detection threshold. One or more of the following factors could cause this: lower mass stars tend to have lower mass accretion rates (Venuti et al. 2014), which would result in lower intensity [OI] $\lambda$ 6300 emission lines; cooler stars have more numerous and deeper photospheric absorption lines near the [OI] $\lambda$ 6300 line that, even after subtracting a photospheric template, lead to higher levels of noise in the spectra; and stars of lower luminosity tend to have spectra with lower signal to noise ratios (S/N), since all of the spectra were observed with the same integration time<sup>13</sup>.

<sup>12</sup> See Sect. 4.2 for a discussion on the connection between mass accretion and [OI] $\lambda$ 6300 emission.

<sup>13</sup> The stars that were observed in configuration A1 are an exception (see Sect. 2), which was observed a total of four times, resulting in spectra of better S/N than those observed in the other configurations. However the detection rate in this configuration was no different than the overall detection rate.

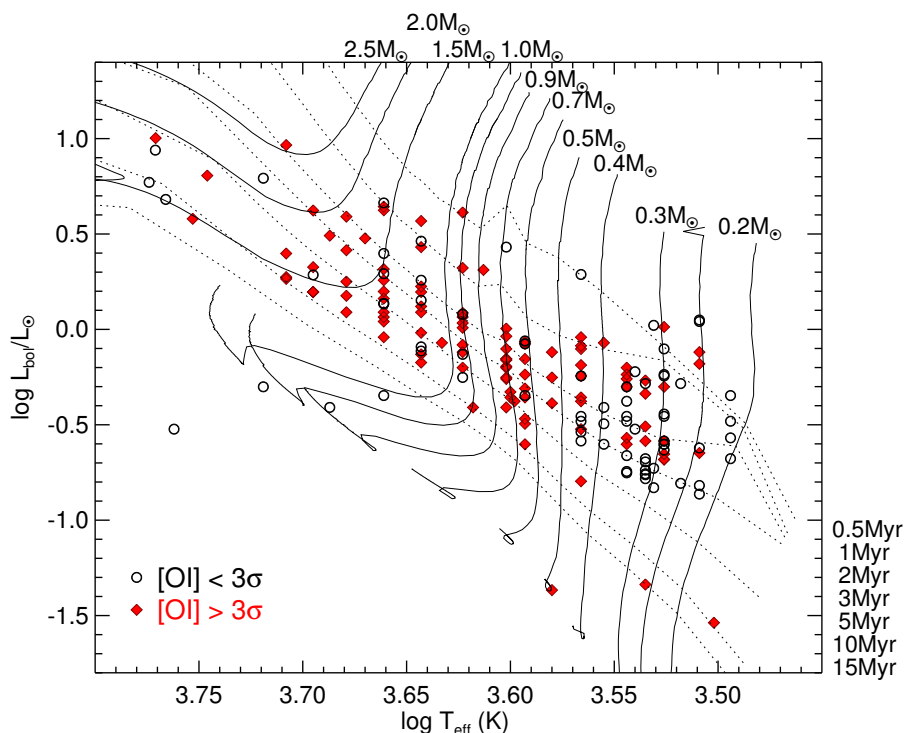


**Fig. A.1.** HR Diagram of the CTTSs in our sample that have detected [OI] $\lambda$ 6300 emission (red filled diamonds) and that do not (black open circles). Mass tracks and isochrones of Siess et al. (2000) are shown as solid and dashed lines, respectively.

The third factor should be countered by a contrast effect: the lower a photosphere’s luminosity, the higher the contrast between a jet’s emission and the stellar continuum. This may be partly why we still detect emission in the lower right corner of the HR diagram, despite the sources being fainter, though this contrast effect does not seem to be enough to counter the other factors. Another effect that can be interfering with the overall [OI] $\lambda$ 6300 detection is the telluric [OI] $\lambda$ 6300 emission line. If a star has only a weak component of low radial velocity which coincides closely with the radial velocity of the telluric emission line on the night of the observation, it will be impossible to recover the intrinsic profile.

In an attempt to assess the level of observational bias, we plot in Fig. A.2 the equivalent width of the measured [OI] $\lambda$ 6300 emission line versus the flux of the continuum at 6300Å. The flux is given in instrumental counts, since our data are not flux calibrated. We separate the stars observed in configuration A1 (right panel) from those observed in all other configurations (left panel), because we expect there may be a difference in the detectability of the [OI] $\lambda$ 6300 line in configuration A1, since it was observed four times and therefore these spectra show better S/N than the spectra that were observed only once. Detections are shown as red filled diamonds, while the upper limits of nondetections are shown as black open diamonds. Upper limits are defined as  $3\sigma$  times the average FWHM of all detected components of the [OI] $\lambda$ 6300 line profiles ( $79 \text{ km s}^{-1}$ ), where  $\sigma$  was measured from two regions of the spectrum  $5\text{Å}$  before and after the [OI] $\lambda$ 6300 line. Though the detections generally lie well above the  $3\sigma$  threshold, there are several that fall in the same range as the upper limits. When analyzing only configuration A1 the outcome is similar. Though in this case the detections separate more from the nondetections, there are still some very close to the region where upper limits fall. The global [OI] $\lambda$ 6300 detection rate in this configuration is very similar to the overall detection rate. From this diagram, we judge that it is not possible to state for certain that the nondetections in our sample truly have no [OI] $\lambda$ 6300 emission. Our heterogeneous detection rate across

the HR diagram, as well as our overall low detection rate compared with other works, are likely caused by an observational bias.

## Appendix B: Calculation of uncertainties

Uncertainties in stellar radial velocities were estimated by assuming that photospheric absorption lines are approximately Gaussian and using the formula for the uncertainty in the centroid of a Gaussian fit, according to Porter et al. (2004):

$$\delta v_{r0} = \frac{FWHM_{phot}}{2\sqrt{2\ln 2} S/N_{phot}}, \quad (\text{B.1})$$

where  $FWHM_{phot}$  corresponds to a typical width of the photospheric lines of a given spectrum and  $S/N_{phot}$  is the signal-to-noise ratio of that spectrum, both of which were measured directly in the spectra. For the CTTSs, we added to the uncertainty the  $\delta v_{r0}$  of the WTTS template that was used to determine its stellar rest velocity, therefore  $\delta v_{r0,CTTS} = \sqrt{\delta v_{r0}^2 + \delta v_{r0,WTTS}^2}$ .

For the absolute values of  $v_{rad}$ , given in Table C.2, we considered an additional uncertainty corresponding to a systematic shift of  $\Delta\lambda = 2 \text{ km s}^{-1}$ , which was observed between these values of  $v_{rad}$  and values we derived from FLAMES spectra of previous campaigns, which may be due to wavelength calibration issues. The final error bars on  $v_{rad}$  are thus  $\delta v_{rad} = \sqrt{\delta v_{r0}^2 + \Delta\lambda^2}$ . For most ( $\sim 80\%$ ) of our sample,  $\delta v_{rad} \leq 2.6 \text{ km s}^{-1}$ , but it reaches  $13 \text{ km s}^{-1}$  for the spectrum that presented the worst S/N in the photospheric lines (that of star CSIMon-000423).

Errors in the centroid velocities of the Gaussian components ( $\delta v_c$ ) were estimated using the formula

$$\delta v_c = \sqrt{\left(\frac{FWHM}{2\sqrt{2\ln 2} S/N}\right)^2 + \delta v_{r0}^2}, \quad (\text{B.2})$$

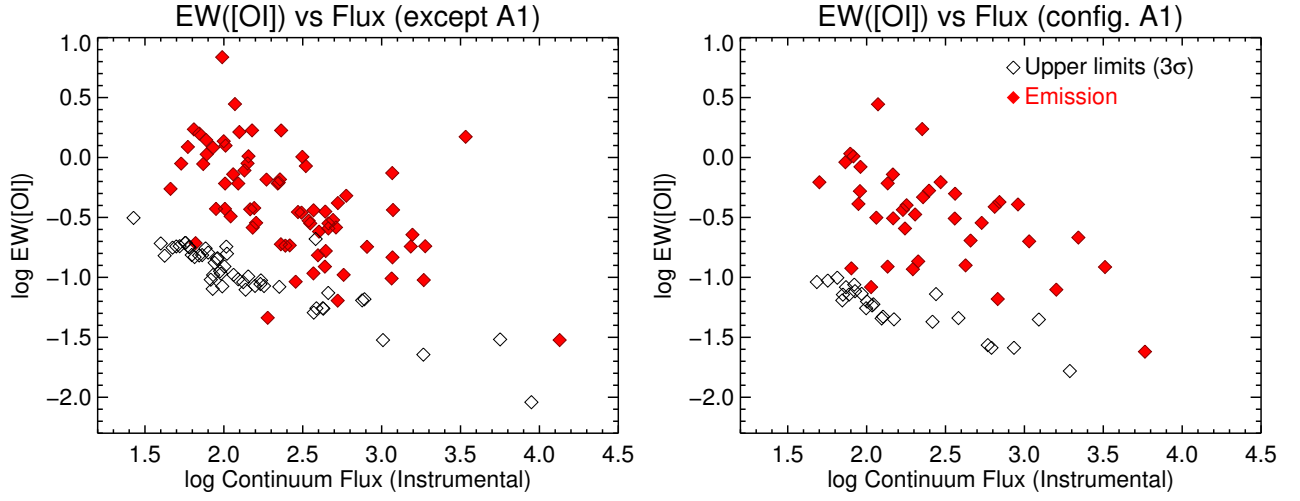


Fig. A.2: Equivalent width of the [OI] $\lambda$ 6300 line versus the instrumental flux of the continuum at 6300Å. Detections are shown as red filled diamonds, while upper limits of nondetections (taken as  $3\sigma$  times the average FWHM of detections in our sample) are shown as black open diamonds. The right panel shows the A1 configuration, which was observed four times and has better S/N, while the left panel shows all other configurations.

where  $S/N$  is the signal to noise ratio of the component (its peak intensity divided by the noise of the residual spectrum) and  $\delta v_{r0}$  is the uncertainty of the stellar rest velocity, disregarding the shift due to wavelength calibration, which would not affect the centroid velocity of the [OI] $\lambda$ 6300 line relative to the stellar rest frame measured in the same spectrum.

For the FWHM, errors were estimated using the formula adapted from Porter et al. (2004),

$$\delta FWHM = \frac{FWHM}{\sqrt{2} S/N}. \quad (\text{B.3})$$

### Appendix C: Tables of stellar and line parameters

Tables C.1 - C.4 are available at the CDS.

Table C.1: Stellar parameters of the WTTs used as photospheric templates

CSIMon ID	2MASS ID	Sp type (Literature)	$L_{bol}$ ( $L_{\odot}$ )	$M_*$ ( $M_{\odot}$ )	$R_*$ ( $R_{\odot}$ )
CSIMon-000020	J06420924+0944034	K7	0.44	0.71	1.39
CSIMon-000029	J06410328+0957549	K7	0.64	0.70	1.68
CSIMon-000057	J06410393+0958094	M3	0.53	0.30	2.16
CSIMon-000066	J06410357+1000353	M1	0.39	0.45	1.53
CSIMon-000071	J06410025+0958496	K1.5	2.60	1.69	2.14
CSIMon-000104	J06410417+0952020	K6	0.98	0.91	1.87
CSIMon-000145	J06412346+0945586	K7	0.44	0.71	1.39
CSIMon-000172	J06411031+0921495	M2.5	0.55	0.33	2.10
CSIMon-000336	J06411889+0939440	K3	0.34	0.82	0.86
CSIMon-000389	J06404875+0932425	K4	0.96	1.25	1.56
CSIMon-000427	J06404244+0932206	K4	0.66	1.12	1.30
CSIMon-000444	J06414457+0942124	M2	0.41	0.36	1.75
CSIMon-000445	J06420256+0936525	K6	0.58	0.95	1.44
CSIMon-000548	J06410856+0942515	M1	0.45	0.45	1.66
CSIMon-000555	J06412445+0932451	M5	0.18	0.19	1.45
CSIMon-000559	J06412425+0931541	K6	0.63	0.95	1.50
CSIMon-000565	J06410077+0951223	K4.5	1.91	1.35	2.29
CSIMon-000606	J06411446+0933214	K5	1.05	1.20	1.77
CSIMon-000622	J06412179+0945309	K5	0.78	1.16	1.53
CSIMon-000779	J06404819+0927008	M5	0.24	0.21	1.67
CSIMon-000798	J06405694+0948407	F9	5.90	1.57	2.30
CSIMon-000819	J06412918+0939359	G5	5.20	1.65	2.37
CSIMon-000901	J06404335+0950595	K7	0.95	0.69	2.03
CSIMon-000995	J06402569+0958356	K2	2.70	1.75	2.25
CSIMon-001089	J06402989+0950104	K2	1.94	1.55	1.90
CSIMon-001158	J06392625+0941108	M0	0.86	0.62	2.01
CSIMon-001172	J06400637+0939335	K7:M0	0.92	0.65	2.04
CSIMon-001192	J06403878+0921382	K3	0.47	0.93	0.95
CSIMon-001247	J06402894+0942171	K6	0.78	0.93	1.68
CSIMon-001248	J06394672+0940539	G5	3.10	1.39	1.84
CSIMon-001251	J06403183+0936006	M2.5	0.50	0.33	2.00
CSIMon-001256	J06394157+0934405	G0	3.30	1.36	1.73
CSIMon-001264	J06403061+0946106	K4	1.13	1.32	1.70
CSIMon-001307	J06392294+0936168	K0	1.25	1.17	1.36

**Notes.** Spectral types were taken from [Venuti et al. \(2014\)](#), who adopted the values of [Dahm & Simon \(2005\)](#), [Rebull et al. \(2002\)](#) or [Walker \(1956\)](#), in that order of preference, or derived them from CFHT colors when no classification was available in the literature. Stellar luminosities, masses and radii were also adopted from [Venuti et al. \(2014\)](#).

## Appendix D: Additional figures

Table C.2: Stellar parameters of the CTTSS

CSIMon ID	2MASS ID	Sp type (Lit)	Sp type (WTTTS)	$L_{bol}$ ( $L_{\odot}$ )	$M_{*}$ ( $M_{\odot}$ )	$R_{*}$ ( $R_{\odot}$ )	$\dot{M}_{acc}$ ( $M_{\odot}/yr$ )	$L_{acc}$ ( $L_{\odot}$ )	Veiling ( $r$ )	$\alpha_{RAC}$	$E(K-3.6\mu m)$	Period (days)	$v_{rad}$ (km/s)	$v \sin i$ (km/s)	$i$ ( $^{\circ}$ )
CSIMon-000011	J06411725+0954323	K7	K7	0.79	0.70	1.86	1.86e-07	9.74e-02	0.30±0.02	...	1.15	...	21.2±2.1	14.5±2.0	...
CSIMon-000021	J06405944+0959454	K5	K5	0.96	1.20	1.69	9.50e-10	1.70e-02	0.06±0.02	...	0.48	3.15	18.5±2.1	17.7±4.2	53 <sup>+37</sup> <sub>-28</sub>
CSIMon-000056	J06415315+0950474	K5	K5	0.77	1.16	1.52	5.75e-09	2.18e-03	0.02±0.02	-1.36	0.25	5.83	20.2±2.0	15.8±2.7	61 <sup>+29</sup> <sub>-13</sub>
CSIMon-000062	J06422190+0948329	K0	...	0.50	0.90	0.86	...	...	...	...	0.12	...	...	...	...
CSIMon-000063	J06411193+0959412	M2.5	M2.5	0.17	0.32	1.19	6.17e-09	2.89e-03	0.35±0.03	-1.37	...	...	17.9±2.0	16.0±6.2	...
CSIMon-000064	J06411070+0957424	M1.5	M1	0.39	0.40	1.62	4.68e-09	1.27e-03	0.03±0.02	-1.15	0.43	9.44	23.1±2.0	9.5±2.0	55 <sup>+35</sup> <sub>-16</sub>
CSIMon-000090	J06410896+0933460	M3	M5	0.58	0.30	2.26	1.10e-08	1.83e-02	0.00±0.03	-0.88	...	4.11	20.4±2.0	13.5±3.2	29 <sup>+16</sup> <sub>-14</sub>
CSIMon-000103	J06405954+0935109	K6	K5	4.10	0.93	3.84	9.61e-09	5.38e-02	0.12±0.03	-1.14	0.78	3.35	22.0±2.7	33.2±2.3	35 <sup>+12</sup> <sub>-11</sub>
CSIMon-000109	J06413743+0937280	K4	K4	2.50	1.51	2.32	...	...	0.13±0.02	-1.76	-0.12	...	46.3±2.0	...	...
CSIMon-000117	J06405413+0948434	M2.5	M2.5	0.18	0.32	1.21	3.39e-08	2.07e-01	1.14±0.06	-2.34	0.39	...	12.5±2.0	32.3±19.1	...
CSIMon-000119	J06412100+0933361	K6	K6	1.16	0.91	2.04	3.34e-09	4.19e-02	0.24±0.06	-1.44	0.72	3.31	18.9±2.1	20.8±1.2	42 <sup>+16</sup> <sub>-13</sub>
CSIMon-000120	J06411911+0926294	M3	M5	0.50	0.30	2.09	1.70e-07	1.01e-01	0.10±0.03	-2.12	0.30	...	20.5±3.9	18.2±4.6	...
CSIMon-000123	J06410821+0934094	M2.5:M3	M2.5	1.05	0.31	2.97	5.56e-10	1.46e-03	0.41±0.04	-1.09	0.30	...	21.3±2.0	22.9±4.8	...
CSIMon-000126	J06405783+0941201	M0	M2.5	0.86	0.62	2.02	2.14e-08	3.03e-02	0.68±0.11	-1.09	0.97	...	21.6±23.1	12.3±2.3	...
CSIMon-000131	J06404927+0923350	K7	K7	0.70	0.70	1.60	1.10e-08	1.22e-01	0.09±0.06	...	...	12.87	19.4±2.1	14.7±2.7	90
CSIMon-000134	J06411441+0926582	M3.5	M5	0.52	0.28	2.20	1.70e-09	4.77e-04	0.37±0.03	-1.72	0.05	3.02	18.2±2.0	22.8±5.1	38 <sup>+25</sup> <sub>-18</sub>
CSIMon-000136	J06411599+0926094	M0	...	0.84	0.62	1.99	1.58e-08	7.94e-02	...	-0.53	0.36	...	...	...	...
CSIMon-000137	J06404712+0942077	M2	M2.5	0.25	0.36	1.36	2.88e-09	2.73e-03	0.00±0.08	-1.54	0.44	5.51	18.3±3.1	13.0±6.6	40 <sup>+50</sup> <sub>-23</sub>
CSIMon-000153	J06405990+0947044	M3	M2.5	0.21	0.29	1.35	9.12e-09	4.90e-03	0.64±0.09	-1.71	0.91	1.90	19.8±18.4	19.1±16.1	32 <sup>+36</sup> <sub>-34</sub>
CSIMon-000168	J06414287+0925084	K5:M0	M2.5	0.39	0.90	1.20	1.15e-08	4.59e-02	0.28±0.03	-1.38	0.53	10.02	20.0±2.4	10.6±3.1	70 <sup>+20</sup> <sub>-8</sub>
CSIMon-000177	J06410620+0936229	G5	K2	3.80	1.48	2.03	9.29e-09	2.20e-01	0.05±0.03	...	0.34	3.03	21.7±2.1	30.0±4.0	62 <sup>+28</sup> <sub>-27</sub>
CSIMon-000192	J06405001+0944545	M3	M5	0.25	0.30	1.49	8.51e-10	5.96e-04	0.07±0.02	-1.31	...	4.50	20.7±2.0	17.2±4.5	50 <sup>+18</sup> <sub>-9</sub>
CSIMon-000207	J06405904+0949062	M2:M2.5	M2.5	0.30	0.34	1.52	5.18e-10	2.92e-03	0.00±0.02	-2.04	-0.02	2.00	20.9±2.0	12.1±3.0	18 <sup>+9</sup> <sub>-9</sub>
CSIMon-000212	J06411830+0944067	M2.5	M2.5	0.21	0.32	1.30	6.46e-10	...	0.13±0.02	-1.16	0.24	7.64	20.5±2.0	14.1±4.4	63 <sup>+27</sup> <sub>-11</sub>
CSIMon-000219	J06411890+0935541	M4	M5	0.14	0.23	1.18	1.91e-09	8.86e-03	0.37±0.03	-1.87	0.24	...	14.4±2.0	22.8±17.2	...
CSIMon-000220	J06412454+0937355	M3	M2.5	0.36	0.30	1.79	2.51e-09	6.55e-04	0.23±0.03	...	0.05	0.75	11.9±2.0	55.5±10.1	27 <sup>+14</sup> <sub>-13</sub>
CSIMon-000225	J06410622+0925036	M5	M5	0.45	0.22	2.30	4.47e-09	6.15e-03	0.28±0.03	-1.58	0.27	8.84	20.9±2.0	23.2±13.9	42 <sup>+48</sup> <sub>-22</sub>
CSIMon-000228	J06405624+0939327	M1	M1.5	0.57	0.45	1.86	1.66e-08	8.03e-03	0.62±0.03	...	0.32	6.33	25.4±8.8	20.7±2.8	73 <sup>+7</sup> <sub>-7</sub>
CSIMon-000250	J06410050+0945031	K3	K2	1.23	1.35	1.63	1.44e-09	1.96e-02	0.00±0.02	-2.10	0.51	8.93	24.0±2.1	14.0±2.0	84 <sup>+6</sup> <sub>-3</sub>
CSIMon-000260	J06411099+0935556	K7	M1	0.55	0.71	1.55	1.07e-08	2.20e-02	0.46±0.03	-0.93	1.41	9.04	23.4±4.2	11.5±8.9	31 <sup>+59</sup> <sub>-29</sub>
CSIMon-000273	J06411837+0939411	M1	M2.5	0.42	0.45	1.60	2.14e-08	1.41e-01	0.04±0.02	-2.28	0.04	11.32	22.1±2.3	12.4±2.6	90
CSIMon-000279	J06412119+0932146	M2.5	M2.5	0.20	0.32	1.28	6.76e-10	8.72e-04	0.35±0.03	-1.59	0.18	7.93	19.4±2.0	13.4±8.1	41 <sup>+49</sup> <sub>-23</sub>
CSIMon-000280	J06404100+0927543	K4	K4	0.45	0.99	1.07	8.91e-10	1.04e-02	0.14±0.01	-1.97	0.15	12.47	20.2±2.0	14.2±3.9	90
CSIMon-000290	J06405867+0936132	M4	M5	1.10	0.25	3.35	2.95e-08	8.49e-03	0.13±0.04	...	0.33	5.94	18.0±2.0	31.2±7.2	54 <sup>+36</sup> <sub>-16</sub>
CSIMon-000295	J06404340+0930343	M0	M2.5	0.25	0.67	1.09	2.75e-09	3.12e-03	0.21±0.03	-1.12	0.76	...	21.5±5.7	13.4±3.3	...
CSIMon-000296	J06405059+0954573	K2	K2	1.57	1.42	1.71	1.73e-09	4.49e-02	0.00±0.02	-2.14	0.35	7.83	21.6±2.0	15.1±1.6	76 <sup>+14</sup> <sub>-6</sub>
CSIMon-000297	J06404516+0928444	K2	K1.5	1.57	1.42	1.71	5.75e-09	2.03e-01	0.01±0.03	...	0.47	3.17	17.3±2.2	31.5±2.7	65 <sup>+25</sup> <sub>-15</sub>
CSIMon-000314	J06404459+0932261	M3	M5	0.21	0.29	1.35	9.55e-09	7.07e-03	0.40±0.04	-2.61	0.20	3.28	14.7±4.7	35.4±8.7	73 <sup>+17</sup> <sub>-7</sub>

Table C.2: Stellar parameters of the CTTs - continued

CSIMon ID	2MASS ID	Sp type (Lit)	Sp type (WTTs)	$L_{bol}$ ( $L_{\odot}$ )	$M_*$ ( $M_{\odot}$ )	$R_*$ ( $R_{\odot}$ )	$\dot{M}_{acc}$ ( $M_{\odot}/yr$ )	$L_{acc}$ ( $L_{\odot}$ )	Veiling ( $r$ )	$\alpha_{RAC}$	E(K-3.6 $\mu$ m)	Period (days)	$v_{rad}$ (km/s)	$v \sin i$ (km/s)	$i$ ( $^{\circ}$ )
CSIMon-000318	J06404458+0948126	K6	K6	1.20	0.91	2.07	4.70e-10	5.20e-03	0.00±0.06	-0.97	...	4.95	20.8±2.0	14.3±2.9	43 <sup>+30</sup> <sub>-19</sub>
CSIMon-000326	J06405882+0939187	M0	K7	0.34	0.66	1.27	1.70e-09	1.16e-02	0.26±0.05	-1.39	0.06	6.64	20.3±2.1	13.1±6.5	44 <sup>+46</sup> <sub>-21</sub>
CSIMon-000328	J06412700+0930131	M1	M2	0.30	0.45	1.34	2.40e-09	1.02e-02	0.51±0.06	-1.88	0.02	10.00	20.9±2.4	11.5±2.4	86 <sup>+4</sup> <sub>-4</sub>
CSIMon-000330	J06413160+0948328	K2	K2	1.93	1.55	1.89	1.34e-10	2.76e-03	0.00±0.04	-2.84	-0.10	5.05	17.7±2.0	23.2±1.6	70 <sup>+8</sup> <sub>-8</sub>
CSIMon-000335	J06413728+0945066	K4	K4	1.45	1.40	1.92	2.31e-09	4.45e-02	0.00±0.02	-0.93	0.36	4.58	16.8±2.1	15.2±2.1	46 <sup>+29</sup> <sub>-18</sub>
CSIMon-000340	J06415593+0940468	M2.5	M1.5	0.52	0.33	2.05	3.55e-09	1.24e-03	0.00±0.02	-2.82	0.11	1.23	17.3±2.0	12.4±4.2	8 <sup>+3</sup> <sub>-3</sub>
CSIMon-000341	J06405426+0949203	M0.5	M2.5	0.56	0.53	1.73	6.17e-08	1.61e-01	0.12±0.03	...	0.63	9.80	21.7±2.9	36.3±19.8	90
CSIMon-000342	J06405573+0946456	M4	M5	0.24	0.25	1.57	1.66e-08	2.36e-02	0.30±0.03	-1.79	0.37	...	19.3±2.0	22.5±4.2	...
CSIMon-000346	J06410908+0930090	K7	K7	0.69	0.70	1.73	2.28e-09	2.32e-02	0.54±0.03	...	...	5.83	20.8±2.5	18.0±3.0	61 <sup>+29</sup> <sub>-12</sub>
CSIMon-000347	J06410444+0936433	M2.5	M5	0.26	0.33	1.45	1.12e-08	2.58e-02	0.43±0.04	-0.47	0.40	...	18.2±10.4	31.2±6.0	...
CSIMon-000349	J06404912+0937363	K7:M0	K7	0.42	0.69	1.38	6.46e-09	7.84e-03	0.63±0.03	...	1.08	...	21.2±2.6	17.1±4.5	...
CSIMon-000352	J06412562+0944032	M2	M2.5	0.33	0.36	1.56	5.01e-09	2.83e-02	0.03±0.02	-1.18	0.30	...	18.8±2.0	12.1±2.6	...
CSIMon-000356	J06410574+0931012	M5	K6	1.68	1.20	2.24	1.29e-09	1.74e-02	0.18±0.02	-1.23	0.23	4.36	29.8±2.0	...	...
CSIMon-000358	J06410673+0947275	M3	M5	0.22	0.29	1.39	6.61e-09	4.27e-04	0.07±0.03	-1.59	0.37	12.88	18.7±2.2	14.6±4.5	65 <sup>+25</sup> <sub>-11</sub>
CSIMon-000359	J06404221+0940110	M0	K7:M0	0.70	0.62	1.83	1.48e-08	1.49e-01	0.17±0.02	-1.92	0.36	5.82	23.2±5.8	19.2±5.4	65 <sup>+25</sup> <sub>-11</sub>
CSIMon-000361	J06410308+0929045	M	M2.5	0.17	0.26	1.25	8.71e-10	1.13e-03	0.03±0.03	-1.62	0.19	2.30	20.4±2.0	19.1±5.1	61 <sup>+13</sup> <sub>-13</sub>
CSIMon-000370	J06405679+0937490	K5	K5	1.57	1.20	2.17	2.55e-08	4.36e-01	0.22±0.02	-1.17	...	11.84	21.2±2.1	12.4±1.8	69 <sup>+21</sup> <sub>-21</sub>
CSIMon-000379	J06410497+0950460	K2	K1.5	2.12	1.60	1.99	1.26e-09	5.37e-02	0.03±0.03	-1.91	0.51	3.66	19.8±2.2	25.2±3.6	66 <sup>+24</sup> <sub>-30</sub>
CSIMon-000392	J06404464+0948021	B8	...	58.0	2.70	2.10	...	2.81e+00	...	...	...	27.18	65.0±23.5	265±75	90
CSIMon-000406	J06405968+0928438	K3	M1	0.63	0.70	1.59	4.79e-08	1.03e-01	0.85±0.09	-0.87	0.63	6.63	24.8±2.4	24.4±18.9	31 <sup>+59</sup> <sub>-39</sub>
CSIMon-000412	J06404711+0932401	M1	K7	0.79	0.45	2.19	1.05e-07	4.74e-02	0.19±0.02	-1.37	0.50	6.68	19.3±2.2	17.2±2.8	56 <sup>+13</sup> <sub>-13</sub>
CSIMon-000423	J06411485+0925550	M2.5	M2.5	0.05	0.26	0.61	1.41e-09	2.30e-02	3.04±0.26	-0.57	1.76	...	18.5±30.9	...	...
CSIMon-000424	J06411521+0937576	M1	M2.5	0.35	0.45	1.45	6.61e-09	3.93e-03	0.44±0.07	-1.08	0.35	...	20.7±2.0	11.8±3.4	...
CSIMon-000425	J06411668+0929522	K5	K5	3.70	1.22	3.34	5.89e-09	5.41e-02	0.20±0.02	-0.66	0.94	7.51	37.2±2.0	15.7±3.4	44 <sup>+21</sup> <sub>-21</sub>
CSIMon-000426	J06411945+0930286	K5	K3	1.42	1.20	2.06	1.75e-08	2.56e-01	0.00±0.02	-2.73	-0.02	...	47.4±2.0	12.7±1.4	...
CSIMon-000433	J06410111+0934522	M1	M1	0.16	0.44	0.99	1.38e-09	3.52e-03	0.37±0.03	-2.24	...	9.80	21.7±2.2	14.0±1.4	90
CSIMon-000434	J06410406+0935211	M2.5	M5	0.54	0.33	2.08	4.79e-09	2.15e-03	0.08±0.05	-1.25	0.27	7.49	20.6±2.4	15.1±3.3	54 <sup>+36</sup> <sub>-16</sub>
CSIMon-000441	J06405809+0936533	M2	M2.5	0.50	0.36	1.92	3.63e-09	1.86e-03	0.61±0.04	-1.41	0.70	12.50	22.2±7.3	...	...
CSIMon-000448	J06410360+0930290	M4	M5	0.66	0.25	2.61	1.15e-08	5.98e-03	0.12±0.03	-1.12	0.54	4.73	16.4±4.4	30.1±8.2	51 <sup>+99</sup> <sub>-17</sub>
CSIMon-000456	J06405154+0943242	K4	K4	1.58	1.41	2.00	5.12e-09	9.08e-02	0.09±0.05	...	0.51	5.05	22.6±2.1	22.6±3.1	60 <sup>+13</sup> <sub>-13</sub>
CSIMon-000457	J06410673+0934459	G6	G5	6.40	1.82	2.70	6.01e-09	9.24e-02	0.65±0.06	-0.01	1.69	...	23.1±3.0	42.1±2.4	...
CSIMon-000462	J06404218+0933374	G0	F9	10.06	1.90	2.90	3.16e-08	5.20e-01	0.00±0.12	...	0.67	1.91	17.8±2.1	35.7±1.4	28 <sup>+8</sup> <sub>-8</sub>
CSIMon-000469	J06404114+0933578	K7	M5	0.56	0.71	1.56	7.59e-08	1.47e-01	1.68±0.34	-0.99	0.38	...	20.8±22.0	...	...
CSIMon-000474	J06410682+0927322	G	K2	...	...	...	...	6.64e+00	0.15±0.05	...	...	...	22.2±2.0	17.5±1.3	...
CSIMon-000484	J06410542+0934095	M4.5	M5	0.01	0.13	0.34	9.12e-11	3.18e-04	0.71±0.05	...	...	19.50	25.7±2.0	...	...
CSIMon-000491	J06405616+0936309	K3	K3	2.60	1.70	2.36	3.72e-09	2.20e-01	0.35±0.08	-0.58	1.11	...	19.2±4.1	61.9±4.7	...
CSIMon-000498	J06404750+0949289	K3	K4	3.90	1.90	2.88	1.00e-08	1.73e-01	0.12±0.05	-1.41	0.42	4.30	27.3±2.1	26.0±2.7	50 <sup>+40</sup> <sub>-18</sub>

Table C.2: Stellar parameters of the CTTs - continued

CSIMon ID	2MASS ID	Sp type (Lit)	Sp type (WTTs)	$L_{bol}$ ( $L_{\odot}$ )	$M_*$ ( $M_{\odot}$ )	$R_*$ ( $R_{\odot}$ )	$\dot{M}_{acc}$ ( $M_{\odot}/yr$ )	$L_{acc}$ ( $L_{\odot}$ )	Veiling ( $r$ )	$\alpha_{RAC}$	$E(K-3.6\mu m)$	Period (days)	$v_{rad}$ (km/s)	$v \sin i$ (km/s)	$i$ ( $^{\circ}$ )
CSIMon-000510	J06410429+0924521	M0	K7	0.84	0.62	1.99	9.12e-08	2.29e-01	0.78±0.04	-0.97	0.85	14.99	18.1±2.2	14.3±2.1	90
CSIMon-000525	J06405118+0944461	G0	G0	8.70	1.80	2.82	1.23e-08	1.97e-01	0.27±0.20	-1.69	0.94	1.99	18.1±2.0	51.8±4.6	46 <sup>+26</sup> <sub>-17</sub>
CSIMon-000530	J06411938+0921469	K2.5	K2	0.39	0.82	0.89	1.35e-08	3.02e-01	0.14±0.02	-1.59	...	...	39.3±2.0	13.1±2.1	...
CSIMon-000553	J06410303+0937357	M1	M1	1.94	0.45	3.44	9.75e-10	3.21e-03	1.02±0.05	-1.22	0.95	...	19.8±2.0	39.8±5.8	...
CSIMon-000558	J06413974+0940279	K4	K4	4.40	1.60	3.35	6.06e-08	9.00e-01	0.25±0.02	-1.46	0.45	11.71	18.4±2.0	15.4±2.1	58 <sup>+32</sup> <sub>-14</sub>
CSIMon-000566	J06405275+0943004	M3.5	M5	0.16	0.26	1.21	2.29e-09	1.92e-03	0.09±0.03	...	0.37	...	18.8±2.0	18.0±3.9	...
CSIMon-000577	J06405639+0935533	K3	K4	1.50	1.45	1.79	3.72e-08	9.22e-02	1.79±0.10	-1.14	1.01	...	17.8±4.1	16.3±2.9	...
CSIMon-000578	J06414382+0940500	K1	K1.5	2.50	1.62	2.03	2.10e-09	4.22e-02	0.03±0.03	-1.49	0.49	...	15.8±2.3	29.3±1.7	...
CSIMon-000578	J06415003+0929322	K6	K6	0.74	0.94	1.63	6.92e-09	9.26e-03	0.08±0.06	-2.78	0.03	3.27	19.5±2.0	25.9±4.1	55 <sup>+35</sup> <sub>-15</sub>
CSIMon-000590	J06405891+0928528	M1	M2.5	0.57	0.45	1.86	2.40e-09	9.62e-03	0.00±0.10	-1.89	0.19	...	18.0±2.0	22.1±4.8	...
CSIMon-000598	J06405932+0946165	M1	M1	0.82	0.45	2.24	4.17e-08	3.28e-02	0.34±0.05	-1.64	0.40	13.41	28.4±2.4	15.2±1.8	90
CSIMon-000613	J06410577+0948174	K6.5	K6	2.05	0.78	2.85	1.92e-08	1.32e-01	0.41±0.02	-1.65	0.71	8.46	24.6±2.1	14.4±3.5	58 <sup>+32</sup> <sub>-10</sub>
CSIMon-000619	J06411475+0934134	K8.5	M2.5	0.44	0.69	1.41	3.98e-08	4.02e-02	0.43±0.03	-1.04	0.96	6.40	19.7±2.5	15.7±4.8	57 <sup>+30</sup> <sub>-14</sub>
CSIMon-000628	J06410827+0930228	M3	M5	0.26	0.30	1.51	3.39e-09	1.34e-02	1.26±0.09	-1.52	0.35	...	26.3±11.4	...	...
CSIMon-000631	J06410587+0922556	A2/3	...	25.90	...	...	...	...	...	...	...	...	20.0±5.3	...	...
CSIMon-000632	J06404936+0952539	M0.5	M1.5	0.04	0.49	0.48	4.17e-10	3.67e-03	1.51±0.08	-0.56	1.99	...	24.8±25.2	...	...
CSIMon-000636	J06404884+0943256	M0	M1	0.87	0.62	2.03	4.79e-08	4.65e-03	0.11±0.04	-0.68	1.26	9.04	28.0±2.0	16.3±2.7	72 <sup>+18</sup> <sub>-8</sub>
CSIMon-000637	J06404921+0957387	M1	M1	0.44	0.45	1.64	3.16e-09	1.83e-02	0.09±0.02	-2.67	0.14	12.31	26.0±2.6	13.3±3.0	90
CSIMon-000650	J06410098+0932444	K1	K4	...	...	...	...	1.62e-01	0.26±0.05	...	...	...	18.4±2.1	...	...
CSIMon-000655	J06412313+0937338	M1	M2.5	0.29	0.45	1.33	1.86e-09	2.24e-03	0.40±0.03	-1.85	0.51	...	20.1±2.0	16.9±4.4	...
CSIMon-000660	J06410051+0929159	K4	K2	1.36	1.40	1.86	1.45e-10	8.06e-03	0.02±0.02	-1.72	0.60	5.12	19.3±2.0	23.5±3.3	66 <sup>+24</sup> <sub>-10</sub>
CSIMon-000667	J06412878+0938388	K3	K2	1.78	1.53	1.95	1.84e-09	2.25e-02	0.00±0.10	-0.57	0.94	5.90	18.1±2.1	20.5±2.3	66 <sup>+20</sup> <sub>-10</sub>
CSIMon-000676	J06414780+0934096	K5	K6	1.81	1.20	2.32	...	...	0.15±0.04	-1.53	0.23	9.40	14.9±2.0	15.3±1.8	66 <sup>+24</sup> <sub>-10</sub>
CSIMon-000681	J06413111+0926582	K3.5	K4	3.00	1.69	2.65	4.49e-08	8.47e-01	0.47±0.03	-1.44	0.73	...	18.1±2.0	16.1±1.6	...
CSIMon-000685	J06404547+0949101	M2	...	0.50	0.36	1.93	4.37e-09	1.98e-02	...	-2.33	0.05	0.18	...	...	...
CSIMon-000697	J06413455+0936325	M1	M1	0.33	0.45	1.41	2.40e-09	1.81e-03	0.12±0.02	...	0.10	15.32	20.9±2.0	14.2±3.0	90
CSIMon-000717	J06411511+0926443	M0.5	M1	0.76	0.53	2.02	2.82e-08	1.72e-02	0.37±0.03	-1.47	0.52	8.56	19.3±2.3	18.8±3.6	77 <sup>+13</sup> <sub>-5</sub>
CSIMon-000718	J06410416+0920443	M2:M2.5	...	0.60	0.34	2.16	4.90e-09	4.32e-03	...	...	...	...	...	...	...
CSIMon-000727	J06412364+0947163	M2	M2.5	0.18	0.35	1.15	4.57e-10	5.61e-04	0.04±0.02	-2.01	0.04	8.11	17.6±2.0	11.4±3.5	62 <sup>+28</sup> <sub>-12</sub>
CSIMon-000733	J06404982+0947309	M4	M5	1.12	0.25	3.38	1.41e-08	7.58e-04	0.32±0.03	-1.30	0.09	...	0.1±2.0	12.0±5.0	...
CSIMon-000736	J06410689+0929240	M0	M2.5	0.49	0.64	1.53	2.24e-09	3.23e-03	0.00±0.07	-1.23	0.24	3.14	20.8±2.7	14.6±3.0	36 <sup>+21</sup> <sub>-6</sub>
CSIMon-000753	J06410597+0939142	M5	M5	0.27	0.21	1.79	3.47e-09	2.54e-04	1.22±0.09	-1.28	0.28	7.67	10.4±2.0	47.8±6.4	90
CSIMon-000754	J06405302+0952594	M0	M1	0.45	0.64	1.46	1.41e-09	2.95e-03	0.18±0.03	-2.82	-0.11	0.97	22.0±2.0	75.8±2.3	84 <sup>+6</sup> <sub>-38</sub>
CSIMon-000765	J06405363+0933247	K1	K2	1.88	1.45	1.76	6.48e-09	1.54e-01	0.00±0.06	-2.29	0.21	2.37	17.2±2.1	22.2±2.4	36 <sup>+16</sup> <sub>-16</sub>
CSIMon-000766	J06404837+0948385	M0.5	M0	0.41	0.53	1.47	2.14e-08	6.54e-02	0.57±0.05	-1.38	0.79	2.80	22.3±3.2	14.6±4.6	33 <sup>+24</sup> <sub>-18</sub>
CSIMon-000774	J06405884+0930573	K2.5	K1.5	3.10	1.83	2.49	5.05e-09	9.33e-02	0.02±0.03	...	0.48	3.49	21.1±2.2	31.4±3.5	60 <sup>+30</sup> <sub>-25</sub>
CSIMon-000795	J06411257+0952311	G:V:e	K2	4.20	1.51	2.11	6.59e-08	3.77e-01	0.57±0.04	-1.72	0.62	...	20.9±2.2	32.2±7.0	...
CSIMon-000796	J06405784+0951089	M2.5	M2.5	0.46	0.33	1.93	3.44e-10	1.48e-03	0.00±0.10	...	0.58	...	20.9±4.5	41.1±7.8	...

Table C.2: Stellar parameters of the CTTs - continued

CSIMon ID	2MASS ID	Sp type (Lit)	Sp type (WTTS)	$L_{bol}$ ( $L_{\odot}$ )	$M_{*}$ ( $M_{\odot}$ )	$R_{*}$ ( $R_{\odot}$ )	$\dot{M}_{acc}$ ( $M_{\odot}/yr$ )	$L_{acc}$ ( $L_{\odot}$ )	Veiling ( $r$ )	$\alpha_{RAC}$	$E(K-3.6\mu m)$	Period (days)	$v_{rad}$ (km/s)	$v \sin i$ (km/s)	$i$ ( $^{\circ}$ )
CSIMon-000798	J06405694+0948407	F9	G0	5.90	1.57	2.30	9.33e-09	1.60e-01	0.34±0.04	-3.73	-0.03	3.81	25.5±2.0	20.2±5.3	41 <sup>+36</sup> <sub>-21</sub>
CSIMon-000804	J06405571+0951138	K5.5	K6	0.85	1.06	1.67	6.76e-09	1.74e-02	0.08±0.06	-0.29	0.23	3.27	26.3±2.1	18.3±2.0	45 <sup>+25</sup> <sub>-17</sub>
CSIMon-000808	J06405159+0928445	K4	K5	0.91	1.24	1.52	1.70e-08	1.17e-01	0.14±0.02	-1.85	0.53	...	20.3±2.1	13.0±4.0	...
CSIMon-000810	J06410982+0927122	K5	K5	2.90	1.20	2.95	1.24e-09	1.41e-02	0.03±0.03	-2.84	0.04	2.92	22.0±2.0	56.7±3.1	65 <sup>+25</sup> <sub>-11</sub>
CSIMon-000811	J06404321+0947072	K6	K6	1.08	0.91	1.97	6.75e-09	6.29e-02	0.10±0.02	-1.64	0.77	7.84	19.4±2.1	15.1±1.7	65 <sup>+25</sup> <sub>-11</sub>
CSIMon-000823	J06405014+0957039	M3	M2.5	0.25	0.30	1.49	7.76e-10	9.01e-04	2.94±0.26	...	-0.00	...	22.2±2.0	...	...
CSIMon-000824	J06410183+0938411	K4	K4	1.96	1.48	2.23	3.28e-09	5.09e-04	0.23±0.05	-2.41	0.38	...	19.9±2.0	17.1±1.8	...
CSIMon-000836	J06404729+0947274	M2	M2	0.18	0.35	1.16	5.25e-10	...	0.24±0.02	-1.54	0.14	18.87	20.4±2.0	10.3±4.4	90
CSIMon-000846	J06411286+0926148	K4	K4	4.21	1.59	2.98	4.77e-07	6.40e+00	0.36±0.03	...	9.75	...	20.7±2.1	16.9±2.2	...
CSIMon-000860	J06415492+0942527	M2.5	M2.5	0.17	0.32	1.18	5.62e-09	1.20e-01	0.59±0.03	-3.23	-0.03	...	15.2±2.0	16.0±5.7	...
CSIMon-000861	J06410080+0952075	K8.5	K7	0.47	0.68	1.47	5.62e-08	1.56e-03	0.20±0.02	-1.11	0.55	...	20.7±2.4	16.5±3.7	...
CSIMon-000873	J06411320+0926103	K5	K5	2.70	1.20	2.83	5.77e-08	6.16e-01	0.02±0.03	-1.56	0.58	1.76	18.7±3.5	46.2±1.5	35 <sup>+11</sup> <sub>-10</sub>
CSIMon-000877	J06411678+0927301	K4	K4	1.16	1.33	1.71	2.83e-08	5.33e-01	0.20±0.03	-1.84	0.43	5.18	17.4±2.1	19.2±3.3	59 <sup>+31</sup> <sub>-14</sub>
CSIMon-000879	J06410338+0940448	M1	K7:M0	0.65	0.45	1.99	1.23e-08	2.44e-02	0.00±0.02	-2.69	0.06	11.40	19.5±2.1	14.3±1.9	90
CSIMon-000893	J06410457+0938308	M3	M5	0.26	0.30	1.52	2.29e-08	2.89e-02	0.90±0.07	-0.78	0.49	...	15.8±2.0	27.8±6.3	...
CSIMon-000904	J06404278+0933350	K7	K7	0.39	0.74	1.30	7.36e-11	1.05e-03	0.20±0.02	-2.12	1.16	2.50	16.8±3.0	15.9±4.7	37 <sup>+29</sup> <sub>-20</sub>
CSIMon-000914	J06405191+0937558	G0:G5	G5	0.30	...	0.54	...	...	9.0±2.7	-1.87	1.25	...	...	...	...
CSIMon-000919	J06411329+0931503	M4	M5	0.76	0.25	2.80	2.04e-08	2.83e-02	0.07±0.03	-1.04	0.39	4.17	21.8±6.8	36.3±6.8	55 <sup>+35</sup> <sub>-13</sub>
CSIMon-000926	J06410642+0928388	M1.5	M2.5	0.25	0.40	1.31	5.01e-09	2.59e-02	0.00±0.10	-1.57	0.07	12.32	20.0±2.0	10.1±4.5	56 <sup>+15</sup> <sub>-15</sub>
CSIMon-000928	J06412562+0934429	M0	M1	0.58	0.63	1.65	5.62e-09	1.41e-02	0.05±0.05	-1.11	0.27	9.84	19.8±2.1	16.2±2.2	90
CSIMon-000931	J06411808+0938253	M3	M5	0.23	0.29	1.43	5.62e-10	2.71e-03	1.24±0.09	-2.89	0.15	0.96	22.1±2.0	...	...
CSIMon-000936	J06410715+0927294	K5	K6	1.32	1.20	1.98	7.08e-08	1.12e-01	0.47±0.03	-0.95	...	10.77	23.0±2.2	14.2±1.6	90
CSIMon-000937	J06405255+0952059	K7	K7	1.01	0.69	2.10	1.02e-08	6.18e-03	0.07±0.02	-2.40	0.23	...	24.5±2.5	26.4±3.2	...
CSIMon-000945	J06404989+0936494	K4	K4	1.37	1.40	1.86	7.41e-08	1.58e-01	0.86±0.04	-1.43	0.62	4.92	20.1±2.0	12.9±1.8	42 <sup>+23</sup> <sub>-16</sub>
CSIMon-000996	J06404131+0951023	K7	K7	0.92	0.69	2.00	2.04e-07	1.24e-01	0.32±0.06	-1.19	0.72	7.81	26.1±2.6	14.5±4.6	50 <sup>+18</sup> <sub>-18</sub>
CSIMon-001003	J06402564+0959597	M4	M5	0.22	0.24	1.52	2.00e-09	2.17e-02	0.69±0.05	-0.98	0.04	3.45	23.1±12.6	11.8±4.2	32 <sup>+24</sup> <sub>-19</sub>
CSIMon-001011	J06404052+0935011	M4.5	M5	0.03	0.14	0.57	1.15e-09	6.93e-03	0.68±0.05	-1.21	...	2.46	31.0±7.5	...	...
CSIMon-001022	J06403911+0950586	K4	K4	2.07	1.50	2.30	6.31e-09	8.32e-02	0.71±0.09	-1.55	0.84	13.88	21.5±2.3	14.4±1.7	90
CSIMon-001031	J06404005+0935029	K4	K5	1.81	1.46	2.14	1.66e-09	2.85e-02	0.77±0.08	-0.30	0.68	4.45	17.3±2.6	18.6±3.7	50 <sup>+40</sup> <sub>-23</sub>
CSIMon-001033	J06404102+0947577	K7	K7	0.64	0.70	1.67	2.04e-08	5.84e-03	0.03±0.02	-1.97	0.02	14.28	21.2±2.1	14.1±2.0	90
CSIMon-001036	J06403200+0949355	M2	M5	0.27	0.36	1.41	6.17e-08	2.36e-01	0.10±0.06	-0.95	0.56	...	19.8±7.1	...	...
CSIMon-001037	J06403086+0934405	K1	K1.5	1.84	1.45	1.74	9.70e-09	8.32e-02	0.29±0.03	-1.29	0.98	8.88	17.2±2.4	32.2±1.8	90
CSIMon-001038	J06402262+0949462	M0	M1	0.32	0.66	1.23	1.51e-09	7.89e-04	0.09±0.02	-1.83	0.62	6.38	24.3±2.2	14.2±3.2	66 <sup>+24</sup> <sub>-10</sub>
CSIMon-001053	J06404113+0952565	K6	K6	1.02	0.91	1.92	8.51e-09	8.84e-02	0.21±0.02	-1.03	0.98	11.84	20.1±2.1	13.6±2.2	90
CSIMon-001054	J06403652+0950456	M2	M2.5	0.63	0.36	2.17	2.09e-07	2.79e-02	0.43±0.03	-1.29	0.59	8.14	24.6±2.3	12.3±5.6	66 <sup>+24</sup> <sub>-18</sub>
CSIMon-001055	J06404041+0950504	K7	K7	2.70	0.68	3.41	4.04e-08	2.03e-01	0.00±0.04	-2.42	0.15	3.73	19.3±2.0	37.1±3.0	53 <sup>+37</sup> <sub>-19</sub>
CSIMon-001059	J06402063+0940499	M5	M5	0.33	0.22	1.97	3.63e-09	...	1.23±0.07	-1.40	0.39	5.82	-15.4±2.0	5.6±3.1	19 <sup>+15</sup> <sub>-15</sub>
CSIMon-001061	J06402416+0934124	M0	M2.5	0.44	0.64	1.45	4.17e-08	9.84e-03	1.09±0.06	-0.79	0.63	...	17.0±5.0	14.9±3.6	...

Table C.2: Stellar parameters of the CTTs - continued

CSIMon ID	2MASS ID	Sp type (Lit)	Sp type (WTTs)	$L_{bol}$ ( $L_{\odot}$ )	$M_{*}$ ( $M_{\odot}$ )	$R_{*}$ ( $R_{\odot}$ )	$\dot{M}_{acc}$ ( $M_{\odot}/\text{yr}$ )	$L_{acc}$ ( $L_{\odot}$ )	Veiling ( $r$ )	$\alpha_{IRAC}$	E(K-3.6 $\mu\text{m}$ )	Period (days)	$v_{rad}$ (km/s)	$v \sin i$ (km/s)	$i$ ( $^{\circ}$ )
CSIMon-001064	J06403518+0951567	M1	M1	0.91	0.45	2.35	1.45e-08	2.06e-02	0.17±0.07	-0.68	0.32	2.70	22.9±3.5	25.1±6.9	35 <sup>+24</sup> <sub>-18</sub>
CSIMon-001076	J06403819+0929524	M1	M2	0.26	0.45	1.25	4.57e-10	4.15e-04	0.39±0.02	-1.39	0.25	5.88	17.2±2.0	15.3±11.0	33 <sup>+28</sup> <sub>-24</sub>
CSIMon-001094	J06403164+0948233	K5	K5	0.74	1.14	1.49	1.58e-08	1.62e-01	0.22±0.02	-1.96	0.11	4.25	17.5±2.4	21.3±2.1	66 <sup>+24</sup> <sub>-10</sub>
CSIMon-001099	J06404136+0954138	G1	G0	4.80	1.52	2.16	3.23e-09	1.14e-01	0.00±0.04	...	0.78	3.42	26.9±2.0	26.8±3.1	57 <sup>+33</sup> <sub>-23</sub>
CSIMon-001100	J06403934+0934455	K6	K6	2.10	0.90	2.75	3.19e-09	2.62e-02	0.72±0.04	-0.42	1.63	...	20.3±5.1	23.1±3.2	...
CSIMon-001114	J06393339+0952017	M1.5	M2	0.85	0.40	2.40	4.27e-08	1.77e-01	0.33±0.02	...	0.02	2.58	13.5±2.7	32.6±4.5	44 <sup>+26</sup> <sub>-17</sub>
CSIMon-001131	J06393441+0954512	M2	M2.5	0.55	0.36	2.01	2.14e-08	9.45e-02	0.07±0.02	...	0.38	5.14	20.1±2.3	12.3±4.5	38 <sup>+40</sup> <sub>-33</sub>
CSIMon-001132	J06402587+0950576	M2.5	M2.5	0.31	0.33	1.58	2.82e-07	7.76e-02	1.73±0.11	-0.99	1.06	2.96	17.0±5.2	12.5±7.6	28 <sup>+20</sup> <sub>-14</sub>
CSIMon-001140	J06394147+0946196	K4	K4	1.10	1.31	1.67	7.67e-09	...	0.28±0.02	...	0.21	3.92	18.7±2.3	22.4±2.3	59 <sup>+31</sup> <sub>-14</sub>
CSIMon-001142	J06403446+0935182	M2	M2.5	0.35	0.36	1.61	6.07e-10	3.41e-03	0.44±0.03	-1.89	0.03	3.88	17.2±2.0	12.8±5.0	38 <sup>+40</sup> <sub>-34</sub>
CSIMon-001144	J06402309+0927423	K5	K6	0.67	1.12	1.42	2.00e-08	9.54e-02	1.15±0.05	-1.73	0.71	4.11	20.6±2.3	18.3±1.5	60 <sup>+30</sup> <sub>-13</sub>
CSIMon-001149a	J06403059+0950147	M3	M2.5	0.79	0.30	2.63	5.50e-09	...	0.13±0.06	-1.46	0.44	...	22.9±2.0	7.7±4.0	...
CSIMon-001149b	J06403059+0950147	...	K2	...	...	...	...	...	...	...	...	...	-14.6±2.0	10.4±3.2	...
CSIMon-001156	J06403357+0933363	M2.5:M3	M2.5	0.15	0.30	1.12	4.27e-09	1.65e-03	1.01±0.05	-3.21	-0.02	16.33	22.6±2.0	16.0±9.4	79 <sup>+11</sup> <sub>-11</sub>
CSIMon-001157	J06402009+0928285	K6	K6	0.63	0.95	1.51	3.98e-09	2.57e-03	0.07±0.02	-0.79	0.24	3.81	21.3±2.1	14.4±2.4	46 <sup>+37</sup> <sub>-19</sub>
CSIMon-001167	J06403787+0934540	M3	M2.5	0.57	0.30	2.23	4.37e-09	1.40e-02	0.00±0.20	-1.87	0.27	8.80	16.6±2.0	16.0±3.1	61 <sup>+29</sup> <sub>-12</sub>
CSIMon-001171	J06393398+0949208	K7	K7:M0	0.70	0.70	1.75	...	...	0.17±0.02	...	-0.05	18.05	20.1±2.3	10.5±3.9	73 <sup>+17</sup> <sub>-17</sub>
CSIMon-001174	J06401370+0956305	M2	M2.5	0.58	0.35	2.08	6.17e-08	2.12e-01	0.22±0.03	0.01	0.73	6.84	24.2±3.5	14.7±4.6	73 <sup>+46</sup> <sub>-46</sub>
CSIMon-001181	J06401801+0950220	M2	M2.5	0.22	0.35	1.27	1.58e-10	1.09e-03	0.57±0.04	-1.84	0.10	6.10	2.1±2.0	37.6±7.8	90
CSIMon-001187	J06401417+0934283	M1.5	M1	0.32	0.40	1.46	1.91e-09	8.34e-04	1.47±0.07	-1.31	0.62	3.10	-15.3±2.0	6.7±5.4	16 <sup>+18</sup> <sub>-17</sub>
CSIMon-001197	J06402616+0937092	M2.5:M3	M2.5	0.19	0.30	1.25	6.61e-10	...	1.08±0.07	-1.23	0.25	4.03	9.7±2.0	45.1±11.5	90
CSIMon-001199	J06404184+0951445	K5	K5	1.23	1.20	1.92	2.04e-08	4.66e-03	0.00±0.02	-1.53	1.10	3.62	25.4±3.7	35.2±1.1	84 <sup>+6</sup> <sub>-2</sub>
CSIMon-001201	J06403662+0948229	K5	K5	0.81	1.16	1.56	1.59e-10	2.97e-03	0.02±0.02	-4.19	0.03	16.43	20.2±2.0	11.8±2.2	90
CSIMon-001203	J06393939+0945215	K6	K6	0.83	0.93	1.72	2.82e-08	9.73e-02	0.19±0.02	...	0.59	...	19.7±2.1	13.3±2.4	...
CSIMon-001217	J06403665+0952032	K4	K4	1.23	1.30	1.77	8.91e-08	1.53e-01	1.36±0.05	...	1.13	7.86	20.4±2.4	17.8±3.0	81 <sup>+9</sup> <sub>-4</sub>
CSIMon-001219	J06402744+0952303	M4	M5	0.15	0.23	1.25	3.98e-10	2.69e-04	0.04±0.03	-1.48	0.02	1.14	24.1±2.0	...	...
CSIMon-001223	J06400600+0949426	M2	M2	0.42	0.36	1.77	1.26e-08	9.88e-04	0.25±0.03	-1.29	0.34	8.11	22.1±2.0	15.6±3.6	64 <sup>+26</sup> <sub>-11</sub>
CSIMon-001234a	J06401113+0938059	K6	K7	0.76	0.94	1.65	1.45e-09	8.29e-02	0.22±0.06	-1.35	0.64	9.61	24.2±2.4	10.7±2.1	60 <sup>+30</sup> <sub>-13</sub>
CSIMon-001234b	J06401113+0938059	...	K3	...	...	...	...	...	...	...	...	...	-13.4±2.4	7.0±3.0	...
CSIMon-001241	J06403378+0948438	M3	M2.5	0.35	0.30	1.75	6.61e-09	1.87e-03	0.11±0.05	-1.76	0.28	...	15.2±2.0	13.6±4.0	...
CSIMon-001249	J06402027+0956063	M3	M2.5	1.03	0.30	3.01	2.95e-08	3.33e-02	0.05±0.07	-0.67	0.41	1.95	25.0±3.5	21.3±4.5	16 <sup>+7</sup> <sub>-7</sub>
CSIMon-001275	J06402877+0931002	K4	K4	4.60	1.60	3.42	2.51e-08	1.50e-01	0.09±0.02	...	0.49	7.49	16.9±2.0	15.2±3.1	41 <sup>+27</sup> <sub>-18</sub>
CSIMon-001279	J06403123+0931071	K6	K6	1.22	0.91	2.09	4.58e-10	5.02e-03	0.17±0.07	...	0.09	1.98	30.2±2.6	30.1±1.9	34 <sup>+11</sup> <sub>-8</sub>
CSIMon-001304	J06401361+0924494	K0	K1.5	6.20	2.17	3.03	...	...	0.16±0.03	-2.81	...	1.08	22.1±2.0	61.1±4.6	26 <sup>+9</sup> <sub>-9</sub>

**Notes.** The CSIMon ID is a naming scheme devised for the CS12264 campaign (Cody et al. 2014). 2MASS IDs are given for comparison. Spectral types were taken from Venuti et al. (2014), who adopted the values of Dahm & Simon (2005), Rebull et al. (2002) or Walker (1956), or derived them from CFHT colors. Stellar luminosity ( $L_{bol}$ ), mass ( $M_{*}$ ) and radius ( $R_{*}$ ) were determined by Venuti et al. (2014). Mass accretion rates ( $\dot{M}_{acc}$ ) and accretion luminosity ( $L_{acc}$ ) were derived from UV excess by Venuti et al. (2014) or from H $\alpha$  line profiles. Veiling, radial velocities ( $v_{rad}$ ) and  $v \sin i$  were determined using FLAMES spectra. The periods given are those from CoRoT observations (Alencar et al. 2010; Venuti et al. 2017a).  $\alpha_{IRAC}$  and IR excess were determined using photometry from the literature or the CS12264 campaign. Inclinations were estimated by us from the rotational properties of the stars.

Table C.3: Equivalent width, centroid velocity and FWHM of the components of the [O I] 6300Å line

CSIMon ID	Narrow LVC			Broad LVC			Blueshifted HVC			Redshifted HVC		
	EW	$v_c$	FWHM	EW	$v_c$	FWHM	EW	$v_c$	FWHM	EW	$v_c$	FWHM
CSIMon-000011	0.195	-4.7±1.3	38.1±1.8	0.127	-1.1±6.2	72.7±10.3	...	...	...	0.032	114.0±3.1	31.6±5.0
CSIMon-000021	0.039	17.3±2.6	28.3±4.3	...	...	...	...	...	...	...	...	...
CSIMon-000103	0.099	-6.5±3.9	50.1±5.8	0.186	-14.5±9.3	110.6±15.1	...	...	...	...	...	...
CSIMon-000119	0.053	3.4±2.6	38.4±4.1	0.100	-36.1±56.0	250.4±93.2	...	...	...	...	...	...
CSIMon-000120	0.653	2.5±3.5	43.2±1.5	...	...	...	...	...	...	...	...	...
CSIMon-000126	1.008	-29.2±23.1	66.4±2.4	0.665	-20.8±24.5	130.3±14.2	...	...	...	...	...	...
CSIMon-000131	0.372	1.4±1.1	49.1±1.5	...	...	...	...	...	...	...	...	...
CSIMon-000137	...	...	...	0.327	-15.9±12.2	101.4±20.0	...	...	...	...	...	...
CSIMon-000153	...	...	...	0.381	-11.8±21.3	108.5±18.2	0.226	-120.2±18.5	45.4±4.8	...	...	...
CSIMon-000168	...	...	...	0.278	5.8±3.9	70.5±6.1	...	...	...	...	...	...
CSIMon-000177	0.027	0.6±1.8	33.3±2.9	0.051	-9.7±5.5	81.3±9.0	...	...	...	...	...	...
CSIMon-000228	...	...	...	0.601	-8.1±18.9	148.1±28.0	0.986	-33.6±8.7	56.7±2.7	...	...	...
CSIMon-000250	0.286	-1.1±0.7	34.4±0.9	...	...	...	0.015	-39.7±3.1	30.9±5.1	...	...	...
CSIMon-000260	0.093	-10.2±7.2	36.8±10.4	...	...	...	0.970	-49.4±3.7	36.7±1.1	...	...	...
CSIMon-000273	0.254	-4.0±2.4	47.1±3.5	...	...	...	...	...	...	...	...	...
CSIMon-000295	...	...	...	0.432	-10.7±10.8	101.2±15.6	...	...	...	...	...	...
CSIMon-000296	0.185	-5.5±2.1	53.1±3.5	...	...	...	...	...	...	...	...	...
CSIMon-000297	0.174	-0.8±1.3	48.7±1.5	0.114	9.0±15.7	163.2±26.1	...	...	...	...	...	...
CSIMon-000314	...	...	...	0.477	1.3±5.5	72.1±5.9	...	...	...	...	...	...
CSIMon-000326	0.070	21.1±4.9	47.2±8.0	...	...	...	...	...	...	...	...	...
CSIMon-000328	0.114	16.8±6.1	50.9±9.9	...	...	...	...	...	...	...	...	...
CSIMon-000335	0.209	0.0±2.8	54.7±4.6	...	...	...	...	...	...	...	...	...
CSIMon-000341	0.160	-6.1±4.1	47.3±5.8	...	...	...	...	...	...	...	...	...
CSIMon-000346	...	...	...	0.773	-37.5±4.2	107.3±6.6	0.910	-79.7±1.5	45.1±1.0	...	...	...
CSIMon-000347	0.188	13.2±10.4	24.7±3.2	...	...	...	...	...	...	...	...	...
CSIMon-000349	0.556	0.7±2.2	39.3±2.5	0.827	-18.7±6.1	95.9±9.8	...	...	...	...	...	...
CSIMon-000357	0.153	-2.8±1.6	37.4±2.3	...	...	...	...	...	...	0.157	72.2±20.4	145.5±33.9
CSIMon-000358	0.450	-6.1±5.6	37.6±2.1	1.147	-14.4±5.9	80.9±3.7	...	...	...	...	...	...
CSIMon-000359	0.446	-3.2±1.4	40.5±1.4	0.230	2.7±19.8	143.3±33.0	...	...	...	...	...	...
CSIMon-000370	0.130	-1.3±0.9	35.1±1.3	0.076	-3.6±9.0	89.5±14.9	...	...	...	...	...	...
CSIMon-000379	0.073	-2.4±2.6	44.2±4.1	0.090	17.0±6.4	78.6±10.5	...	...	...	...	...	...
CSIMon-000392	0.119	-22.8±23.4	32.9±0.3	...	...	...	1.370	-47.6±23.4	37.2±0.1	...	...	...
CSIMon-000406	...	...	...	0.153	-12.5±5.5	80.0±9.0	0.314	-113.3±2.7	69.9±4.0	...	...	...
CSIMon-000412	...	...	...	0.340	-9.2±4.9	114.2±8.1	...	...	...	...	...	...
CSIMon-000423	...	...	...	0.999	-47.4±31.5	145.0±10.0	...	...	...	...	...	...
CSIMon-000425	0.203	-19.0±1.2	49.3±1.8	...	...	...	0.153	-63.7±1.8	50.5±3.0	0.051	68.8±15.3	103.0±25.5
CSIMon-000433	0.030	8.9±1.5	16.1±2.1	0.539	-7.5±1.5	66.2±2.0	...	...	...	...	...	...

Table C.3: Equivalent width, centroid velocity and FWHM of the components of the [OI] 6300Å line - continued

CSIMon ID	Narrow LVC			Broad LVC			Blueshifted HVC			Redshifted HVC		
	EW	$v_c$	FWHM	EW	$v_c$	FWHM	EW	$v_c$	FWHM	EW	$v_c$	FWHM
CSIMon-000434	...	...	...	0.125	-20.8±16.4	110.5±27.2	...	...	...	...	...	...
CSIMon-000441	0.451	0.9±8.2	52.1±6.8	...	...	...	...	...	...	...	...	...
CSIMon-000448	...	...	...	0.928	-17.4±6.2	136.6±8.1	...	...	...	...	...	...
CSIMon-000456	...	...	...	0.080	6.4±9.6	90.4±16.0	...	...	...	...	...	...
CSIMon-000457	...	...	...	0.940	-40.3±3.0	116.5±3.4	...	...	...	...	...	...
CSIMon-000462	0.031	-2.7±1.3	33.8±1.8	...	...	...	...	...	...	...	...	...
CSIMon-000469	0.146	-19.0±21.9	39.2±1.4	1.691	-49.5±22.0	133.8±3.4	...	...	...	...	...	...
CSIMon-000474	0.106	0.7±0.8	29.6±1.2	0.102	-8.7±5.8	81.3±9.7	...	...	...	...	...	...
CSIMon-000491	...	...	...	0.298	-0.9±6.2	82.3±8.4	...	...	...	...	...	...
CSIMon-000498	0.036	-3.8±2.7	33.6±4.5	0.258	-27.3±4.1	111.9±6.8	...	...	...	...	...	...
CSIMon-000510	...	...	...	0.246	-26.6±2.9	79.4±4.6	...	...	...	...	...	...
CSIMon-000558	...	...	...	0.134	-3.0±3.0	61.4±4.9	...	...	...	...	...	...
CSIMon-000567	...	...	...	0.401	-49.1±6.6	119.4±9.2	...	...	...	...	...	...
CSIMon-000577	...	...	...	0.216	-13.9±16.0	198.2±26.6	...	...	...	...	...	...
CSIMon-000598	0.606	-9.0±1.8	55.0±2.1	...	...	...	...	...	...	...	...	...
CSIMon-000613	0.275	-5.5±1.4	54.7±2.1	0.206	-9.8±46.0	287.4±76.6	...	...	...	...	...	...
CSIMon-000619	...	...	...	0.819	-10.9±2.8	80.5±3.9	...	...	...	...	...	...
CSIMon-000628	...	...	...	0.782	-26.4±16.2	140.7±19.5	...	...	...	...	...	...
CSIMon-000631	...	...	...	0.030	8.7±7.0	69.8±8.4	...	...	...	...	...	...
CSIMon-000632	...	...	...	0.846	-14.3±27.3	120.0±17.8	...	...	...	...	...	...
CSIMon-000637	0.185	-8.1±4.3	43.9±6.6	...	...	...	...	...	...	...	...	...
CSIMon-000650	...	...	...	0.121	12.9±6.7	89.2±11.2	...	...	...	...	...	...
CSIMon-000667	0.107	-6.5±2.8	57.1±4.6	...	...	...	...	...	...	...	...	...
CSIMon-000681	0.052	-1.4±1.5	33.2±2.4	0.079	2.7±12.1	119.4±20.2	...	...	...	...	...	...
CSIMon-000717	...	...	...	0.347	-12.9±10.3	150.6±17.0	...	...	...	...	...	...
CSIMon-000736	0.462	3.7±2.3	42.0±2.4	0.797	-11.7±5.3	103.3±8.3	...	...	...	...	...	...
CSIMon-000765	0.058	1.2±2.7	43.4±4.4	...	...	...	...	...	...	...	...	...
CSIMon-000766	0.470	0.1±2.7	38.4±1.5	0.319	-20.2±6.4	124.4±9.7	...	...	...	...	...	...
CSIMon-000774	0.115	-2.1±3.2	65.0±5.1	0.299	-22.8±7.1	158.8±11.7	...	...	...	...	...	...
CSIMon-000795	...	...	...	0.157	-9.8±2.6	73.8±4.1	...	...	...	...	...	...
CSIMon-000796	...	...	...	0.867	1.0±5.1	93.9±5.0	...	...	...	...	...	...
CSIMon-000804	0.145	1.4±3.2	52.6±5.1	...	...	...	...	...	...	...	...	...
CSIMon-000808	0.139	2.0±2.0	43.0±3.3	...	...	...	...	...	...	...	...	...
CSIMon-000811	...	...	...	0.171	-0.9±4.3	72.6±7.0	...	...	...	...	...	...
CSIMon-000846	0.082	-9.4±1.4	37.9±2.2	0.249	-39.7±6.7	147.6±11.1	...	...	...	...	...	...
CSIMon-000861	...	...	...	0.800	-0.2±3.3	85.8±5.0	...	...	...	...	...	...
CSIMon-000873	0.160	-3.2±2.9	34.5±1.2	0.579	-20.7±3.7	115.2±3.8	...	...	...	...	...	...

Table C.3: Equivalent width, centroid velocity and FWHM of the components of the [OI] 6300Å line - continued

CSIMon ID	Narrow LVC		Broad LVC		Blueshifted HVC		Redshifted HVC	
	EW	$v_c$	EW	$v_c$	EW	$v_c$	EW	$v_c$
CSIMon-000877	0.251	-2.5±1.4	0.240	-1.3±5.6	0.240	121.4±9.3	...	...
CSIMon-000879	0.092	10.7±5.3	...	...	...	...	...	...
CSIMon-000904	...	...	1.292	-4.4±2.6	...	64.1±2.2	...	...
CSIMon-000919	...	...	0.818	-13.5±6.9	...	91.7±4.2	...	...
CSIMon-000928	0.120	-10.1±4.3	...	...	...	...	0.205	49.9±6.9
CSIMon-000936	0.146	-15.4±2.4	0.478	-37.1±11.3	...	168.7±18.8	...	...
CSIMon-000937	...	...	0.200	10.6±13.1	...	117.0±21.7	...	...
CSIMon-000996	...	...	0.104	3.0±9.6	...	70.4±15.8	...	...
CSIMon-001003	0.625	-24.3±12.6	0.563	-19.6±24.9	...	160.8±35.9	...	...
CSIMon-001011	...	...	0.533	-24.0±10.0	...	79.5±11.5	...	34.0±9.4
CSIMon-001022	...	...	0.211	-16.8±17.4	...	151.7±29.0	...	69.1±13.5
CSIMon-001031	...	...	0.292	4.9±7.0	...	80.1±11.3	...	28.3±5.7
CSIMon-001033	...	...	0.332	-4.5±5.3	...	95.1±8.8	...	...
CSIMon-001036	0.289	-7.2±6.8	0.512	-17.1±8.9	...	104.6±9.7	...	...
CSIMon-001037	...	...	0.533	-15.3±2.1	...	95.8±2.6	...	...
CSIMon-001038	...	...	0.305	0.6±6.4	...	85.4±10.5	...	...
CSIMon-001053	0.241	-7.5±1.2	0.195	-36.8±13.6	...	139.4±22.6	...	...
CSIMon-001054	...	...	0.629	-19.6±4.5	...	114.8±7.3	...	...
CSIMon-001061	0.038	-20.7±6.3	0.142	-17.2±14.5	...	165.6±22.9	...	...
CSIMon-001064	...	...	0.734	-22.2±3.2	...	76.9±2.4	...	...
CSIMon-001094	0.126	-2.3±2.5	...	...	...	...	...	...
CSIMon-001100	3.647	-10.5±4.7	...	...	...	...	1.414	-55.3±4.7
CSIMon-001114	0.096	-2.0±2.7	...	...	...	...	...	51.2±0.8
CSIMon-001131	0.282	-0.8±2.1	...	...	...	...	...	...
CSIMon-001132	0.927	-4.9±4.8	...	...	...	...	1.836	-96.0±5.1
CSIMon-001140	0.121	-9.3±3.4	...	...	...	...	...	98.4±2.8
CSIMon-001144	...	...	0.249	-1.6±7.8	...	106.8±12.8	...	...
CSIMon-001157	...	...	0.268	-28.3±2.7	...	67.7±4.3	...	...
CSIMon-001171	0.220	-3.5±1.5	...	...	...	...	...	...
CSIMon-001174	0.243	-2.2±3.1	...	...	...	...	...	...
CSIMon-001199	0.025	-0.5±3.4	0.276	7.0±7.0	...	104.5±10.4	...	...
CSIMon-001203	0.296	-6.0±0.9	...	...	...	...	...	...
CSIMon-001217	0.166	-6.8±2.7	0.193	-49.9±48.2	...	213.3±80.2	...	...
CSIMon-001234	...	...	0.487	15.9±7.5	...	98.8±12.4	...	...
CSIMon-001249	...	...	...	...	...	...	0.324	-57.4±7.5
CSIMon-001279	...	...	0.164	29.4±7.9	...	96.2±12.9	...	...
							0.283	76.0±19.9
								164.0±32.7

Notes. Equivalent widths are given in Å,  $v_c$  and FWHM are given in km/s.

Table C.4: [OI] 6300Å line parameters

CSIMon ID	2MASS ID	$L_{[OI]}$ ( $L_{\odot}$ )	$L_{NLVC}$ ( $L_{\odot}$ )	$L_{BLVC}$ ( $L_{\odot}$ )	$L_{HVC,blue}$ ( $L_{\odot}$ )	$L_{HVC,red}$ ( $L_{\odot}$ )	$v_{jet}$ (km/s)
CSIMon-000011	J06411725+0954323	1.54e-05	8.48e-06	5.52e-06	...	1.39e-06	...
CSIMon-000021	J06405944+0959454	3.55e-06	3.55e-06	...	...	...	...
CSIMon-000056	J06415315+0950474	<1.91e-05	...	...	...	...	...
CSIMon-000062	J06422190+0948329	<2.19e-05	...	...	...	...	...
CSIMon-000063	J06411193+0959412	<3.93e-06	...	...	...	...	...
CSIMon-000064	J06411070+0957424	<8.53e-06	...	...	...	...	...
CSIMon-000090	J06410896+0933460	<3.13e-06	...	...	...	...	...
CSIMon-000103	J06405954+0935109	9.12e-05	3.17e-05	5.95e-05	...	...	...
CSIMon-000109	J06413743+0937280	<5.53e-05	...	...	...	...	...
CSIMon-000117	J06405413+0948434	<3.93e-06	...	...	...	...	...
CSIMon-000119	J06412100+0933361	1.58e-05	5.49e-06	1.04e-05	...	...	...
CSIMon-000120	J06411911+0926294	1.98e-05	1.98e-05	...	...	...	...
CSIMon-000123	J06410821+0934094	<7.87e-06	...	...	...	...	...
CSIMon-000126	J06405783+0941201	9.17e-05	5.53e-05	3.65e-05	...	...	...
CSIMon-000131	J06404927+0923503	3.30e-05	3.30e-05	...	...	...	...
CSIMon-000134	J06411441+0926582	<4.50e-06	...	...	...	...	...
CSIMon-000136	J06411599+0926094	<2.28e-05	...	...	...	...	...
CSIMon-000137	J06404712+0942077	3.58e-06	...	3.58e-06	...	...	...
CSIMon-000153	J06405990+0947044	3.14e-06	...	1.91e-06	1.23e-06	...	-142
CSIMon-000168	J06414287+0925084	9.88e-06	...	9.88e-06	...	...	...
CSIMon-000177	J06410620+0936229	2.99e-05	1.04e-05	1.96e-05	...	...	...
CSIMon-000192	J06405001+0944545	<4.38e-06	...	...	...	...	...
CSIMon-000207	J06405904+0949062	<6.18e-06	...	...	...	...	...
CSIMon-000212	J06411830+0944067	<5.39e-06	...	...	...	...	...
CSIMon-000219	J06411890+0935541	<1.98e-06	...	...	...	...	...
CSIMon-000220	J06412454+0937355	<3.67e-06	...	...	...	...	...
CSIMon-000225	J06410622+0925036	<3.82e-06	...	...	...	...	...
CSIMon-000228	J06405624+0939327	2.47e-05	...	1.16e-05	1.32e-05	...	-116
CSIMon-000250	J06410050+0945031	1.67e-05	1.61e-05	...	5.45e-07	...	-355
CSIMon-000260	J06411099+0935556	1.21e-05	1.47e-06	...	1.06e-05	...	-58
CSIMon-000273	J06411837+0939411	6.98e-06	6.98e-06	...	...	...	...
CSIMon-000279	J06412119+0932146	<2.75e-06	...	...	...	...	...
CSIMon-000280	J06404100+0927543	<2.68e-05	...	...	...	...	...
CSIMon-000290	J06405867+0936132	<6.81e-06	...	...	...	...	...
CSIMon-000295	J06404340+0930343	5.22e-06	...	5.22e-06	...	...	...
CSIMon-000296	J06405059+0954573	2.99e-05	2.99e-05	...	...	...	...
CSIMon-000297	J06404516+0928444	5.35e-05	3.23e-05	2.12e-05	...	...	...
CSIMon-000314	J06404459+0932261	2.58e-06	...	2.58e-06	...	...	...
CSIMon-000318	J06404458+0948126	<2.99e-05	...	...	...	...	...
CSIMon-000326	J06405882+0939187	1.23e-06	1.23e-06	...	...	...	...
CSIMon-000328	J06412700+0930131	1.49e-06	1.49e-06	...	...	...	...
CSIMon-000330	J06413160+0948328	<2.68e-05	...	...	...	...	...
CSIMon-000335	J06413728+0945066	2.76e-05	2.76e-05	...	...	...	...
CSIMon-000340	J06415593+0940468	<9.42e-06	...	...	...	...	...
CSIMon-000341	J06405426+0949203	4.92e-06	4.92e-06	...	...	...	...
CSIMon-000342	J06405573+0946456	<4.53e-06	...	...	...	...	...
CSIMon-000346	J06410908+0930090	4.67e-05	...	2.13e-05	2.53e-05	...	-164
CSIMon-000347	J06410444+0936433	1.92e-06	1.92e-06	...	...	...	...
CSIMon-000349	J06404912+0937363	4.87e-05	1.96e-05	2.91e-05	...	...	...
CSIMon-000352	J06412562+0944032	<5.47e-06	...	...	...	...	...
CSIMon-000356	J06410506+0949228	<2.13e-06	...	...	...	...	...
CSIMon-000357	J06410574+0931012	4.16e-05	2.05e-05	...	...	2.11e-05	+170
CSIMon-000358	J06410673+0947275	7.87e-06	2.22e-06	5.65e-06	...	...	...
CSIMon-000359	J06404221+0940110	2.55e-05	1.68e-05	8.68e-06	...	...	...
CSIMon-000361	J06410308+0929045	<3.12e-06	...	...	...	...	...
CSIMon-000370	J06405679+0937490	2.36e-05	1.49e-05	8.70e-06	...	...	...
CSIMon-000379	J06410497+0950460	5.19e-05	2.33e-05	2.87e-05	...	...	...
CSIMon-000392	J06404464+0948021	1.08e-03	1.05e-04	...	9.78e-04	...	...
CSIMon-000406	J06405968+0928438	2.79e-05	...	1.10e-05	1.69e-05	...	-133
CSIMon-000412	J06404711+0932401	1.70e-05	...	1.70e-05	...	...	...
CSIMon-000423	J06411485+0925550	1.02e-05	...	1.02e-05	...	...	...
CSIMon-000424	J06411521+0937576	<5.52e-06	...	...	...	...	...

Table C.4: [OI] 6300Å line parameters - continued

CSIMon ID	2MASS ID	$L_{[OI]}$ ( $L_{\odot}$ )	$L_{NLVC}$ ( $L_{\odot}$ )	$L_{BLVC}$ ( $L_{\odot}$ )	$L_{HVC,blue}$ ( $L_{\odot}$ )	$L_{HVC,red}$ ( $L_{\odot}$ )	$v_{jet}$ (km/s)
CSIMon-000425	J06411668+0929522	9.96e-05	5.10e-05	...	3.59e-05	1.27e-05	-89/+96
CSIMon-000426	J06411945+0930286	<4.13e-05	...	...	...	...	...
CSIMon-000433	J06410111+0934522	1.67e-05	8.78e-07	1.58e-05	...	...	...
CSIMon-000434	J06410406+0935211	3.00e-06	...	3.00e-06	...	...	...
CSIMon-000441	J06405809+0936533	2.99e-06	2.99e-06	...	...	...	...
CSIMon-000448	J06410360+0930290	1.19e-05	...	1.19e-05	...	...	...
CSIMon-000456	J06405154+0943242	1.83e-05	...	1.83e-05	...	...	...
CSIMon-000457	J06410673+0934459	5.09e-04	...	3.96e-04	4.42e-05	6.90e-05	...
CSIMon-000462	J06404218+0933374	4.74e-05	4.74e-05	...	...	...	...
CSIMon-000469	J06404114+0933578	4.56e-05	2.51e-06	2.91e-05	9.54e-06	4.49e-06	...
CSIMon-000474	J06410682+0927322	1.70e-04	8.66e-05	8.33e-05	...	...	...
CSIMon-000484	J06410542+0934095	<1.83e-06	...	...	...	...	...
CSIMon-000491	J06405616+0936309	2.69e-05	...	2.69e-05	...	...	...
CSIMon-000498	J06404750+0949289	9.50e-05	1.16e-05	8.34e-05	...	...	...
CSIMon-000510	J06410429+0924521	3.65e-05	...	1.69e-05	1.96e-05	...	...
CSIMon-000525	J06405118+0944461	<6.70e-05	...	...	...	...	...
CSIMon-000530	J06411938+0921469	<1.54e-05	...	...	...	...	...
CSIMon-000553	J06410303+0937357	<8.38e-05	...	...	...	...	...
CSIMon-000558	J06413974+0940279	6.42e-05	...	6.42e-05	...	...	...
CSIMon-000566	J06405275+0943004	<3.09e-06	...	...	...	...	...
CSIMon-000567	J06405639+0935533	3.85e-05	...	3.00e-05	8.54e-06	...	...
CSIMon-000577	J06414382+0940500	6.41e-05	...	6.41e-05	...	...	...
CSIMon-000578	J06415003+0929322	<1.32e-05	...	...	...	...	...
CSIMon-000590	J06405891+0928528	<6.90e-06	...	...	...	...	...
CSIMon-000598	J06405932+0946165	3.54e-05	3.54e-05	...	...	...	...
CSIMon-000613	J06410577+0948174	8.10e-05	4.63e-05	3.47e-05	...	...	...
CSIMon-000619	J06411475+0934134	2.86e-05	...	2.86e-05	...	...	...
CSIMon-000628	J06410827+0930228	2.98e-06	...	2.98e-06	...	...	...
CSIMon-000631	J06410587+0922556	9.31e-05	...	9.31e-05	...	...	...
CSIMon-000632	J06404936+0952539	2.42e-06	...	1.58e-06	8.32e-07	...	...
CSIMon-000636	J06404884+0943256	<1.85e-05	...	...	...	...	...
CSIMon-000637	J06404921+0957387	4.08e-06	4.08e-06	...	...	...	...
CSIMon-000650	J06410098+0932444	8.29e-05	...	8.29e-05	...	...	...
CSIMon-000655	J06412313+0937338	<4.57e-06	...	...	...	...	...
CSIMon-000660	J06410051+0929159	<2.36e-05	...	...	...	...	...
CSIMon-000667	J06412878+0938388	3.15e-05	3.15e-05	...	...	...	...
CSIMon-000676	J06414780+0934096	<3.77e-05	...	...	...	...	...
CSIMon-000681	J06413111+0926582	5.42e-05	1.51e-05	2.29e-05	1.62e-05	...	...
CSIMon-000685	J06404547+0949101	<9.28e-06	...	...	...	...	...
CSIMon-000697	J06413455+0936325	<8.93e-06	...	...	...	...	...
CSIMon-000717	J06411511+0926443	1.40e-05	...	1.40e-05	...	...	...
CSIMon-000718	J06410416+0920443	<4.79e-06	...	...	...	...	...
CSIMon-000727	J06412364+0947163	<3.36e-06	...	...	...	...	...
CSIMon-000733	J06404982+0947309	<1.84e-05	...	...	...	...	...
CSIMon-000736	J06410689+0929240	9.55e-06	3.51e-06	6.05e-06	...	...	...
CSIMon-000753	J06410597+0939142	<7.83e-07	...	...	...	...	...
CSIMon-000754	J06405302+0952594	<5.28e-06	...	...	...	...	...
CSIMon-000765	J06405363+0933247	1.14e-05	1.14e-05	...	...	...	...
CSIMon-000766	J06404837+0948385	3.99e-05	1.06e-05	7.22e-06	2.20e-05	...	-105
CSIMon-000774	J06405884+0930573	8.86e-05	2.46e-05	6.40e-05	...	...	...
CSIMon-000795	J06411257+0952311	3.56e-05	...	3.56e-05	...	...	...
CSIMon-000796	J06405784+0951089	1.31e-05	...	1.31e-05	...	...	...
CSIMon-000798	J06405694+0948407	<5.31e-05	...	...	...	...	...
CSIMon-000804	J06405571+0951138	9.57e-06	9.57e-06	...	...	...	...
CSIMon-000808	J06405159+0928445	1.09e-05	1.09e-05	...	...	...	...
CSIMon-000810	J06410982+0927122	<2.92e-05	...	...	...	...	...
CSIMon-000811	J06404321+0947072	2.39e-05	...	2.39e-05	...	...	...
CSIMon-000823	J06405014+0957039	<2.54e-06	...	...	...	...	...
CSIMon-000824	J06410183+0938411	<2.69e-05	...	...	...	...	...
CSIMon-000836	J06404729+0947274	<4.13e-06	...	...	...	...	...
CSIMon-000846	J06411286+0926148	3.38e-04	7.34e-05	2.23e-04	4.15e-05	...	...
CSIMon-000860	J06415492+0942527	<6.35e-06	...	...	...	...	...

Table C.4: [OI] 6300Å line parameters - continued

CSIMon ID	2MASS ID	$L_{[OI]}$ ( $L_{\odot}$ )	$L_{NLVC}$ ( $L_{\odot}$ )	$L_{BLVC}$ ( $L_{\odot}$ )	$L_{HVC,blue}$ ( $L_{\odot}$ )	$L_{HVC,red}$ ( $L_{\odot}$ )	$v_{jet}$ (km/s)
CSIMon-000861	J06410080+0952075	4.45e-05	...	4.45e-05	...	...	...
CSIMon-000873	J06411320+0926103	1.48e-04	3.21e-05	1.16e-04	...	...	...
CSIMon-000877	J06411678+0927301	5.88e-05	3.01e-05	2.88e-05	...	...	...
CSIMon-000879	J06410338+0940448	4.34e-06	4.34e-06	...	...	...	...
CSIMon-000893	J06410457+0938308	<3.47e-06	...	...	...	...	...
CSIMon-000904	J06404278+0933350	3.98e-05	...	3.98e-05	...	...	...
CSIMon-000914	J06405191+0937558	<1.07e-05	...	...	...	...	...
CSIMon-000919	J06411329+0931503	1.51e-05	...	1.21e-05	...	3.02e-06	+87
CSIMon-000926	J06410642+0928388	<3.72e-06	...	...	...	...	...
CSIMon-000928	J06412562+0934429	3.98e-06	3.98e-06	...	...	...	...
CSIMon-000931	J06411808+0938253	<1.15e-06	...	...	...	...	...
CSIMon-000936	J06410715+0927294	7.41e-05	1.41e-05	4.61e-05	1.40e-05	...	...
CSIMon-000937	J06405255+0952059	1.09e-05	...	1.09e-05	...	...	...
CSIMon-000945	J06404989+0936494	<1.30e-05	...	...	...	...	...
CSIMon-000996	J06404131+0951023	2.33e-05	...	8.16e-06	...	1.51e-05	+114
CSIMon-001003	J06402564+0959597	5.35e-06	2.82e-06	2.54e-06	...	...	...
CSIMon-001011	J06404052+0935011	3.82e-06	...	2.41e-06	1.40e-06	...	...
CSIMon-001022	J06403911+0950586	3.53e-05	...	3.25e-05	2.85e-06	...	...
CSIMon-001031	J06404005+0935029	6.83e-05	...	5.33e-05	1.50e-05	...	-151
CSIMon-001033	J06404102+0947577	1.63e-05	...	1.63e-05	...	...	...
CSIMon-001036	J06403200+0949355	1.60e-05	4.35e-06	7.70e-06	3.94e-06	...	...
CSIMon-001037	J06403086+0934405	3.29e-04	...	3.11e-04	1.73e-05	...	...
CSIMon-001038	J06402262+0949462	7.60e-06	...	7.60e-06	...	...	...
CSIMon-001053	J06404113+0952565	2.52e-05	1.39e-05	1.13e-05	...	...	...
CSIMon-001054	J06403652+0950456	1.97e-05	...	1.97e-05	...	...	...
CSIMon-001055	J06404041+0950504	<4.19e-05	...	...	...	...	...
CSIMon-001059	J06402063+0940499	<1.79e-06	...	...	...	...	...
CSIMon-001061	J06402416+0934124	1.08e-05	8.25e-07	3.08e-06	3.94e-06	2.93e-06	...
CSIMon-001064	J06403518+0951567	3.52e-05	...	3.52e-05	...	...	...
CSIMon-001076	J06403819+0929524	<4.28e-06	...	...	...	...	...
CSIMon-001094	J06403164+0948233	8.78e-06	8.78e-06	...	...	...	...
CSIMon-001099	J06404136+0954138	<2.61e-05	...	...	...	...	...
CSIMon-001100	J06403934+0934455	6.09e-04	3.93e-04	...	2.05e-05	1.95e-04	...
CSIMon-001114	J06393339+0952017	4.36e-06	4.36e-06	...	...	...	...
CSIMon-001131	J06393441+0954512	1.07e-05	1.07e-05	...	...	...	...
CSIMon-001132	J06402587+0950576	3.95e-05	1.71e-05	...	2.19e-05	5.45e-07	-108/+60
CSIMon-001140	J06394147+0946196	1.39e-05	1.39e-05	...	...	...	...
CSIMon-001142	J06403446+0935182	<9.46e-06	...	...	...	...	...
CSIMon-001144	J06402309+0927423	1.46e-05	...	1.19e-05	2.76e-06	...	-257
CSIMon-001149	J06403059+0950147	<3.60e-06	...	...	...	...	...
CSIMon-001156	J06403357+0933363	<2.62e-06	...	...	...	...	...
CSIMon-001157	J06402009+0928285	1.16e-05	...	1.16e-05	...	...	...
CSIMon-001167	J06403787+0934540	<5.09e-06	...	...	...	...	...
CSIMon-001171	J06393398+0949208	9.98e-06	9.98e-06	...	...	...	...
CSIMon-001174	J06401370+0956305	7.05e-06	7.05e-06	...	...	...	...
CSIMon-001181	J06401801+0950220	<2.51e-06	...	...	...	...	...
CSIMon-001187	J06401417+0934283	<3.86e-06	...	...	...	...	...
CSIMon-001197	J06402616+0937092	<1.77e-06	...	...	...	...	...
CSIMon-001199	J06404184+0951445	1.29e-05	1.07e-06	1.19e-05	...	...	...
CSIMon-001201	J06403662+0948229	<1.76e-05	...	...	...	...	...
CSIMon-001203	J06393939+0945215	1.51e-05	1.51e-05	...	...	...	...
CSIMon-001217	J06403665+0952032	2.35e-05	1.09e-05	1.26e-05	...	...	...
CSIMon-001219	J06402744+0952303	<1.89e-06	...	...	...	...	...
CSIMon-001223	J06400600+0949426	<6.85e-06	...	...	...	...	...
CSIMon-001234	J06401113+0938059	2.05e-05	...	2.05e-05	...	...	...
CSIMon-001241	J06403378+0948438	<7.19e-06	...	...	...	...	...
CSIMon-001249	J06402027+0956063	1.81e-05	...	...	9.71e-06	8.41e-06	-60/+79
CSIMon-001275	J06402877+0931002	<6.43e-05	...	...	...	...	...
CSIMon-001279	J06403123+0931071	1.86e-05	...	1.86e-05	...	...	...
CSIMon-001304	J06401361+0924494	<7.64e-05	...	...	...	...	...

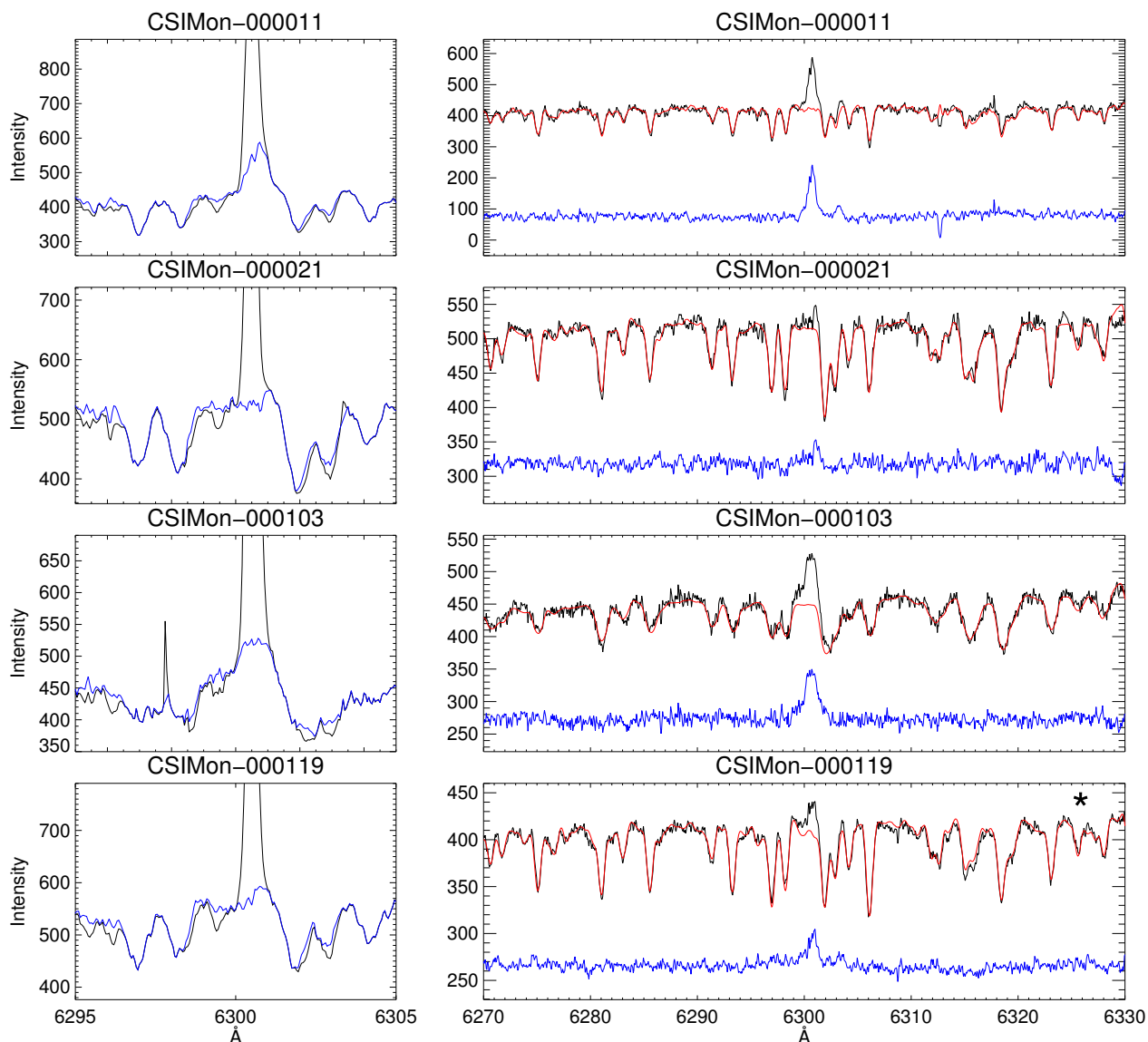


Fig. D.1: Correction of the  $[OI]\lambda 6300$  line profiles for contamination by telluric emission and absorption lines (left panels) and photospheric absorption lines (right panels) for all stars where emission was detected in  $[OI]\lambda 6300$ .

Left panels: the original spectra are plotted in black, while the blue shows the spectrum after corrections for telluric emission and absorption, as well as the removal of cosmic rays. Right panels: the spectrum after telluric corrections is shown in black, while red represents the photospheric template that was used (including veiling and rotational broadening). The final, residual profile is shown in blue, shifted in the vertical axis for better viewing.

**Notes.** Profiles marked with an asterisk on the top right corner of the right panel are those that were observed more than once. In these cases, telluric corrections were applied for each night individually, then the mean spectrum was taken in order to increase the S/N. This mean spectrum (shown in black on the right panels) was then corrected for the photospheric contribution and the residual profile was recovered. For these stars, the left panel shows the telluric corrections of one night.

Some stars did not present photospheric features in the region close to the  $[OI]\lambda 6300$  line, either due to their effective temperature (the B-type star CSIMon-000392) or to insufficient S/N in the photospheric lines (CSIMon-000423, CSIMon-000632, and CSIMon-001011). For these stars, we fitted the continuum and subtracted it to recover the residual profile.

The star CSIMon-000631 is an A-type star for which a good template was not found since few hot stars were included in our observations. We used as its photospheric template an F-type star with a similar absorption feature close to the  $[OI]\lambda 6300$  line in order to remove this feature, ignoring the rest of the spectrum. This is why the absorption line close to  $6320\text{\AA}$  is not well fitted.

The star CSIMon-001234 is a spectroscopic binary, therefore it was fitted with a combination of two photospheric templates.

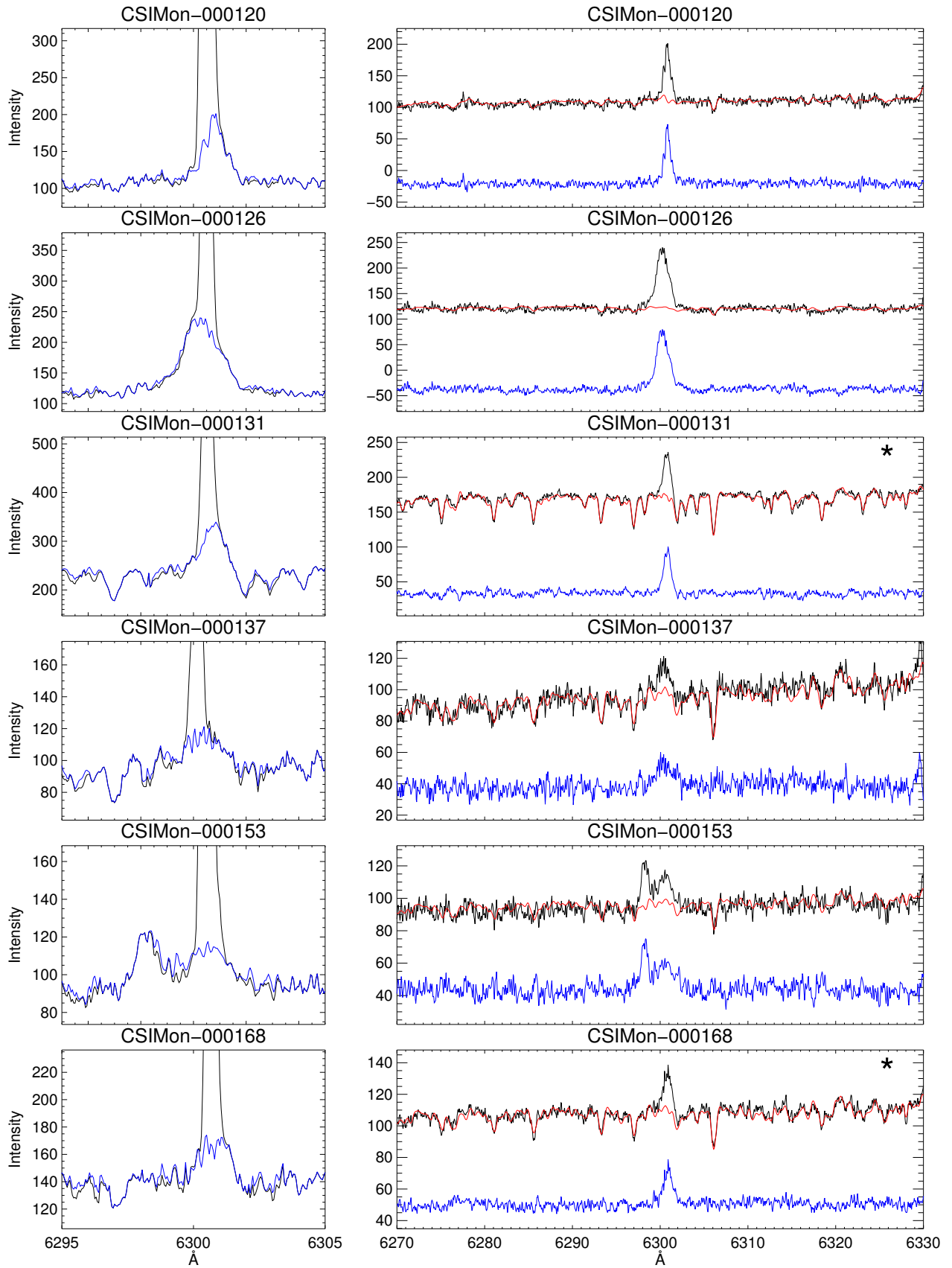


Fig. D.1: Continued.

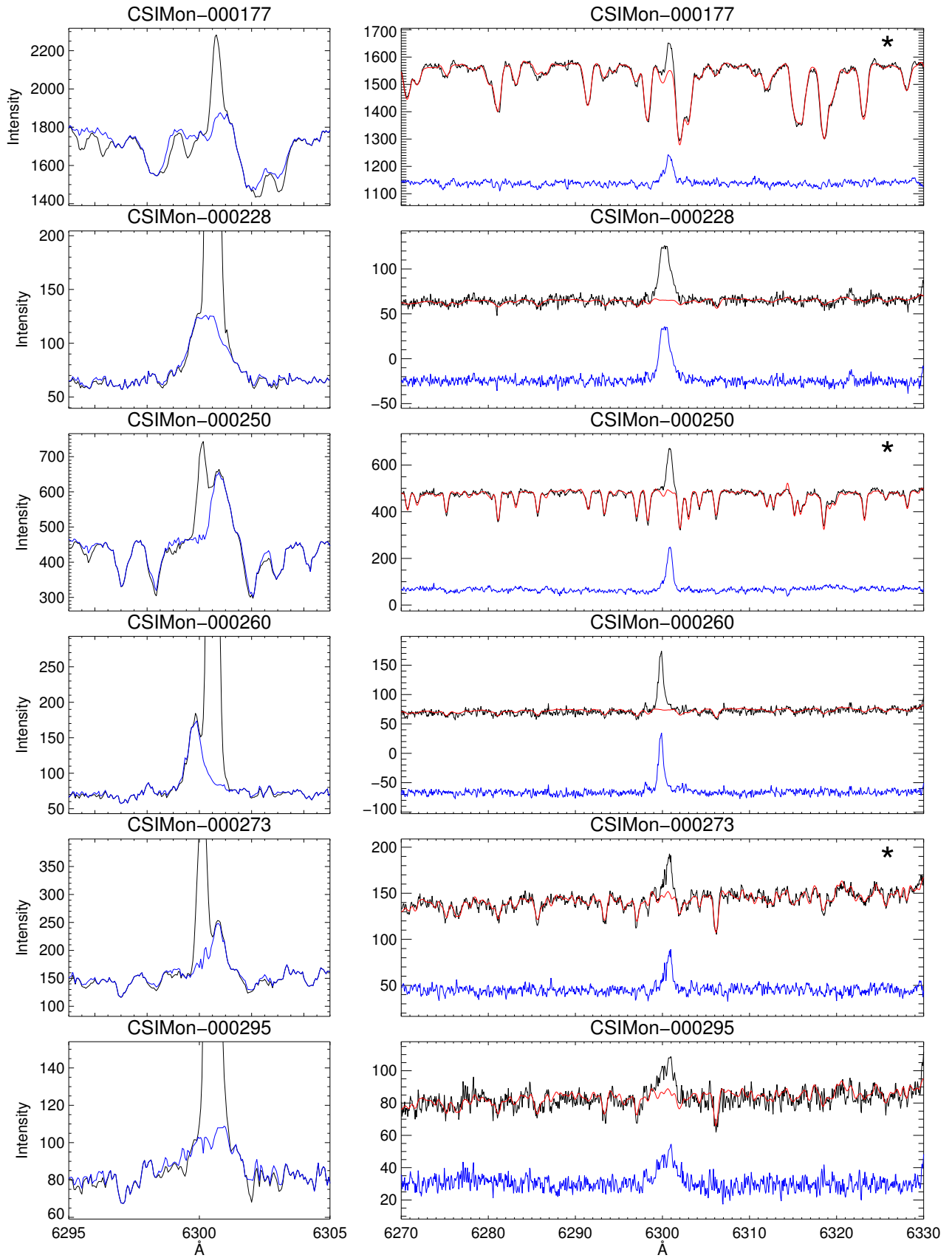


Fig. D.1: Continued.

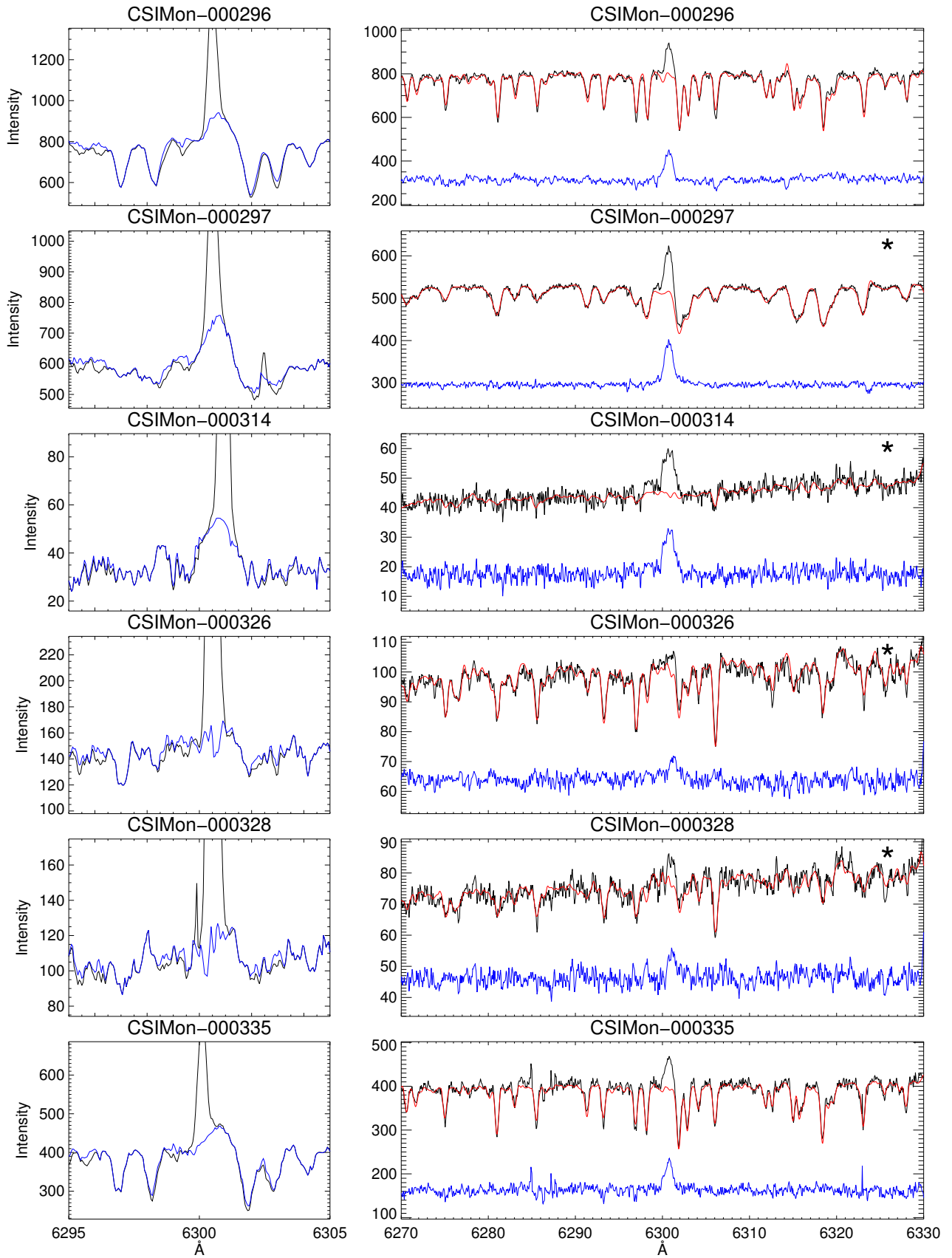


Fig. D.1: Continued.

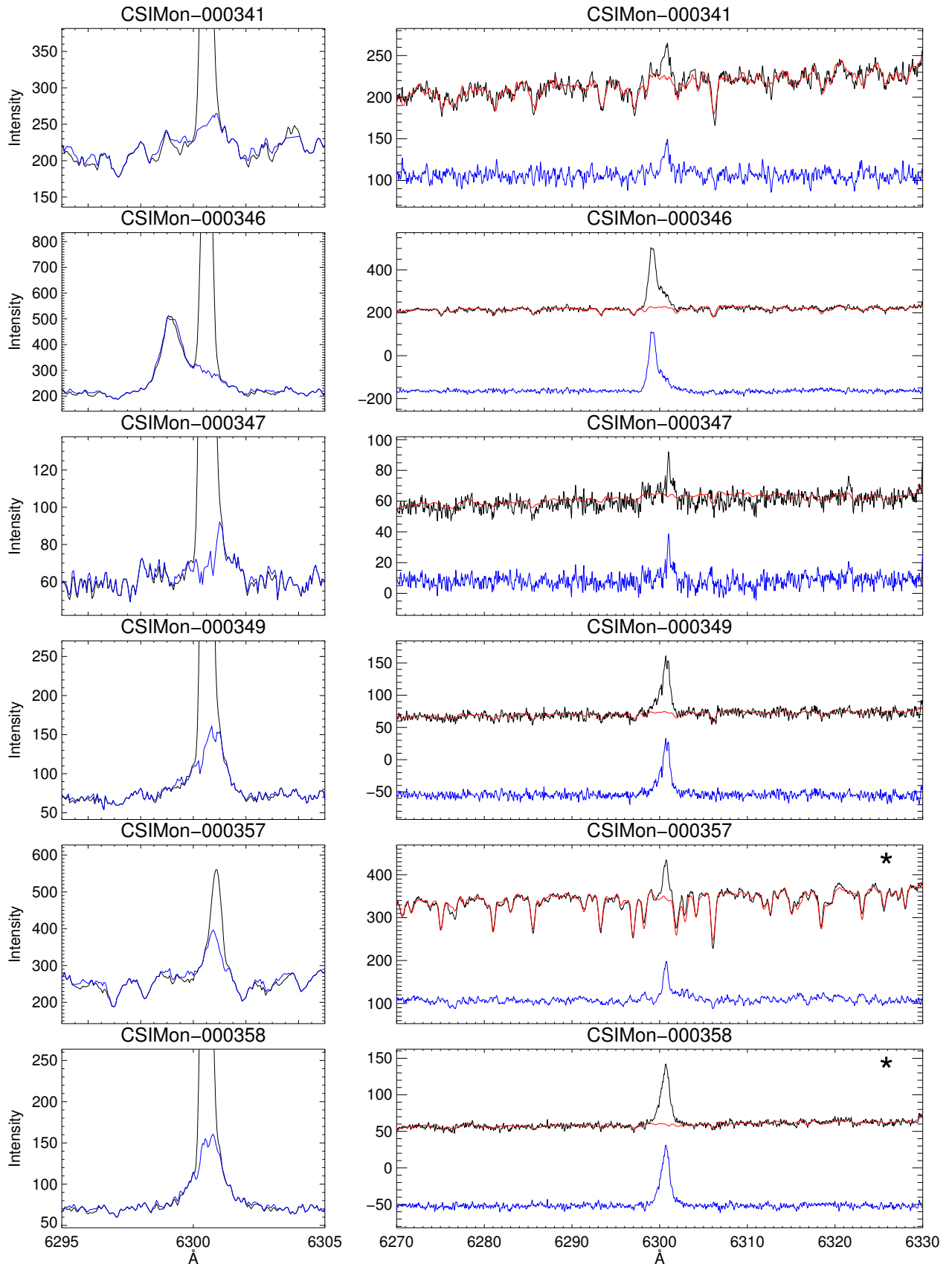


Fig. D.1: Continued.

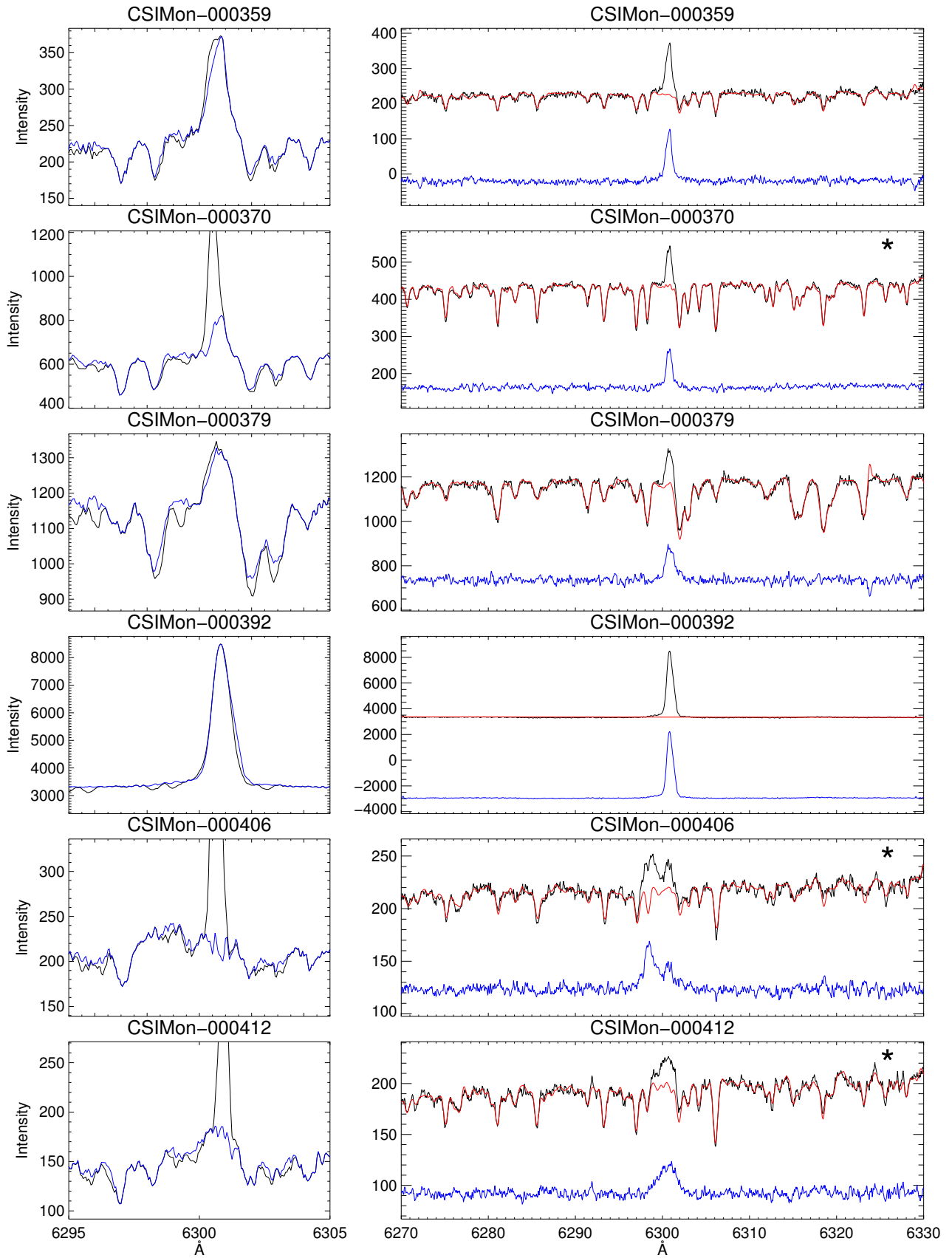


Fig. D.1: Continued.

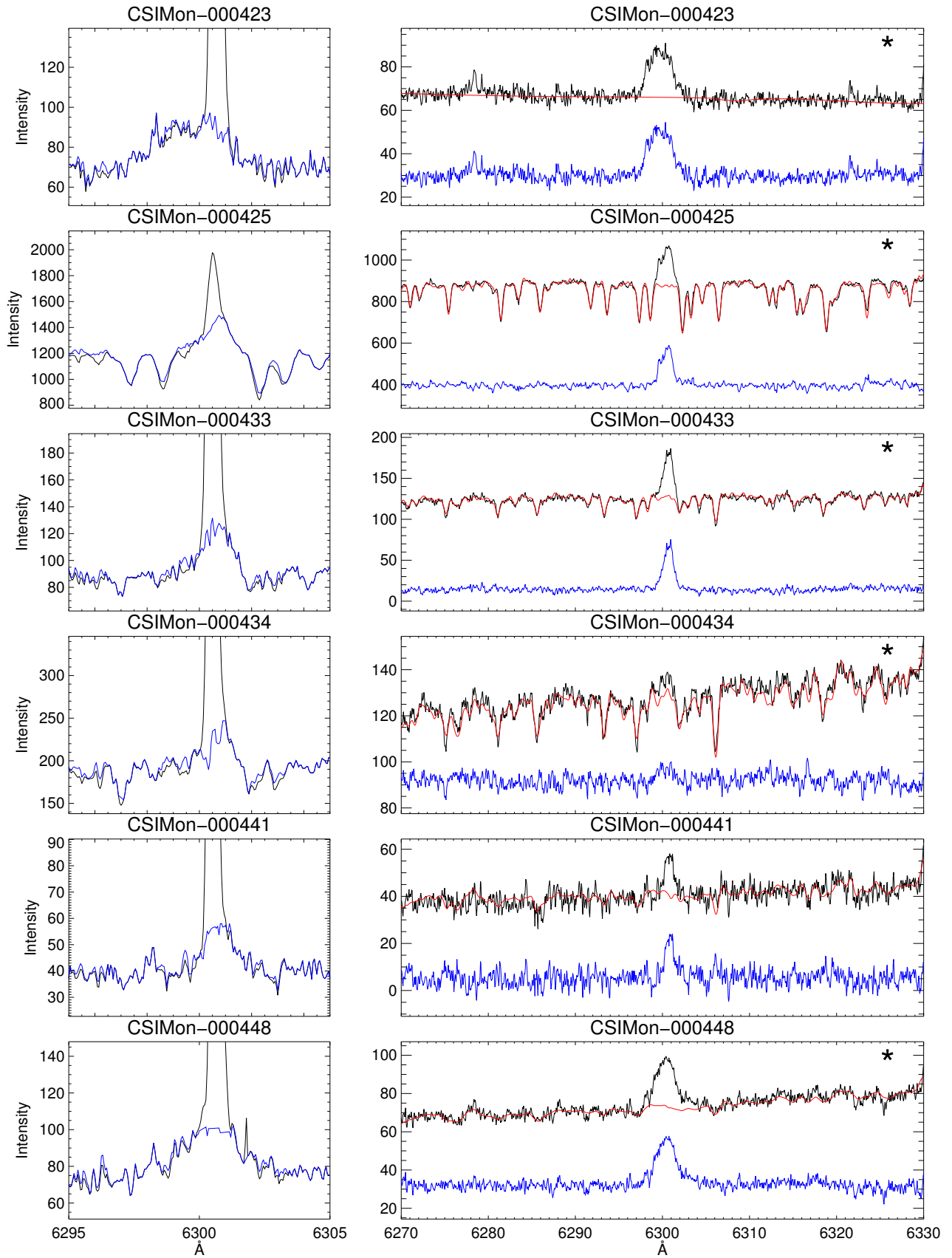


Fig. D.1: Continued.

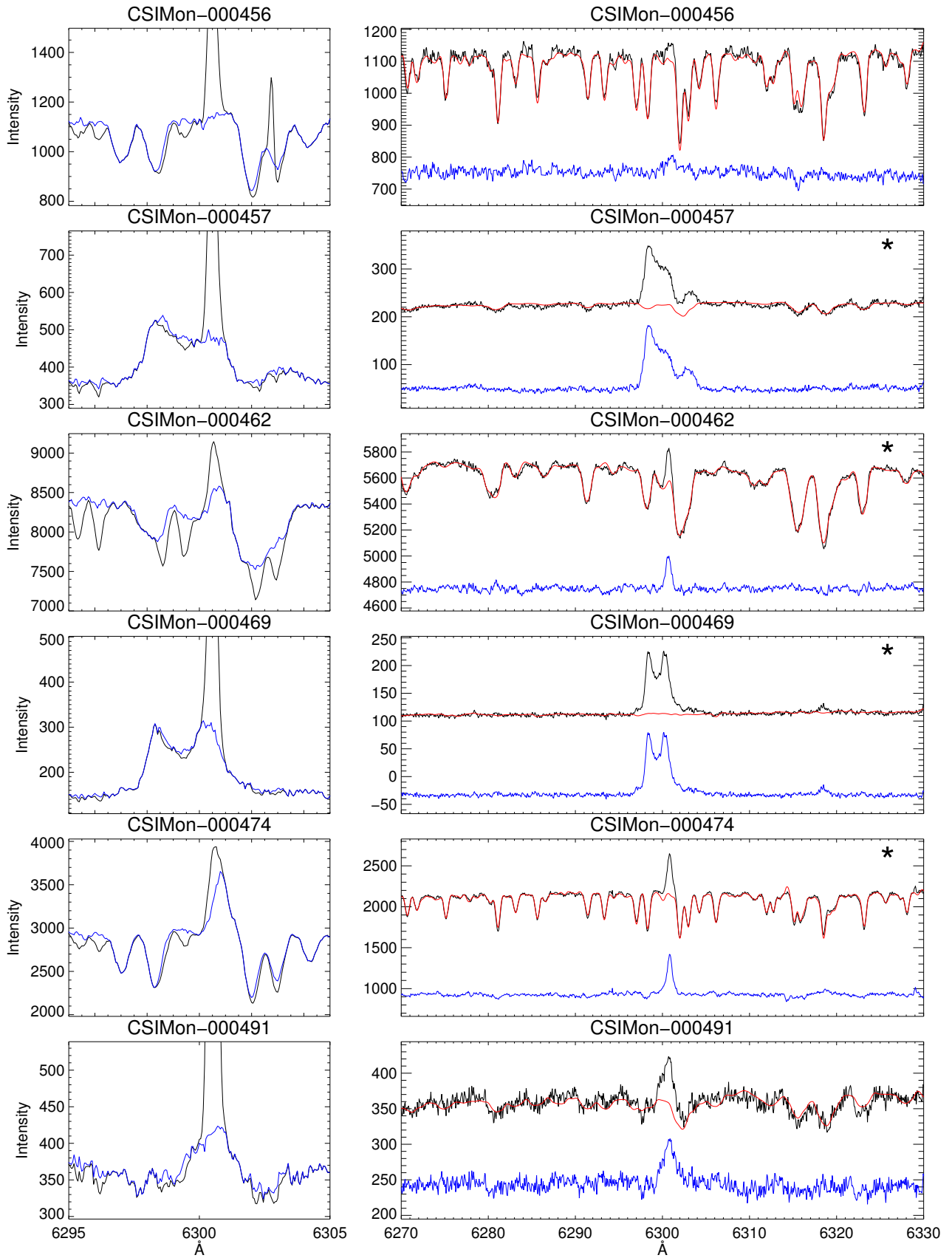


Fig. D.1: Continued.

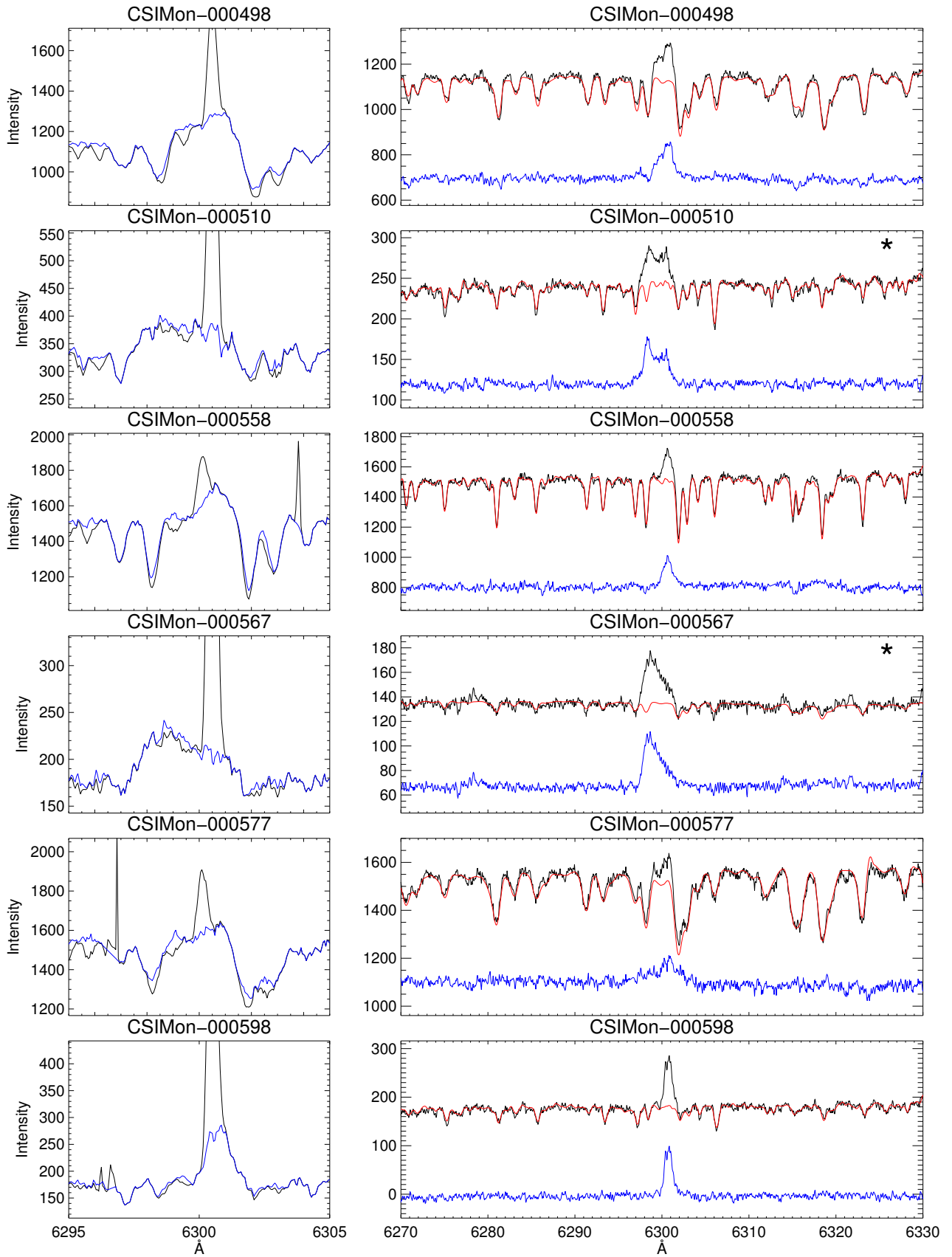


Fig. D.1: Continued.

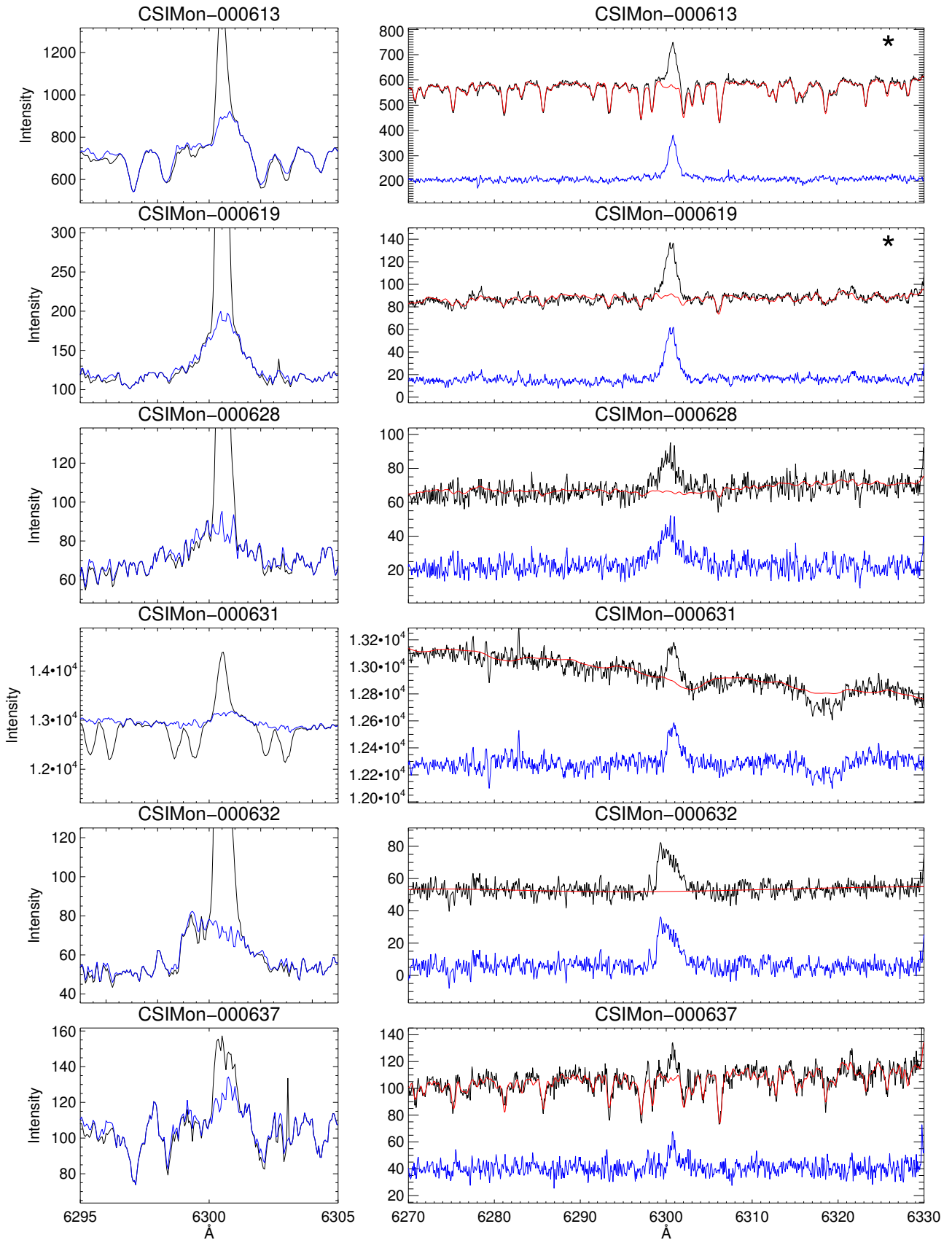


Fig. D.1: Continued.

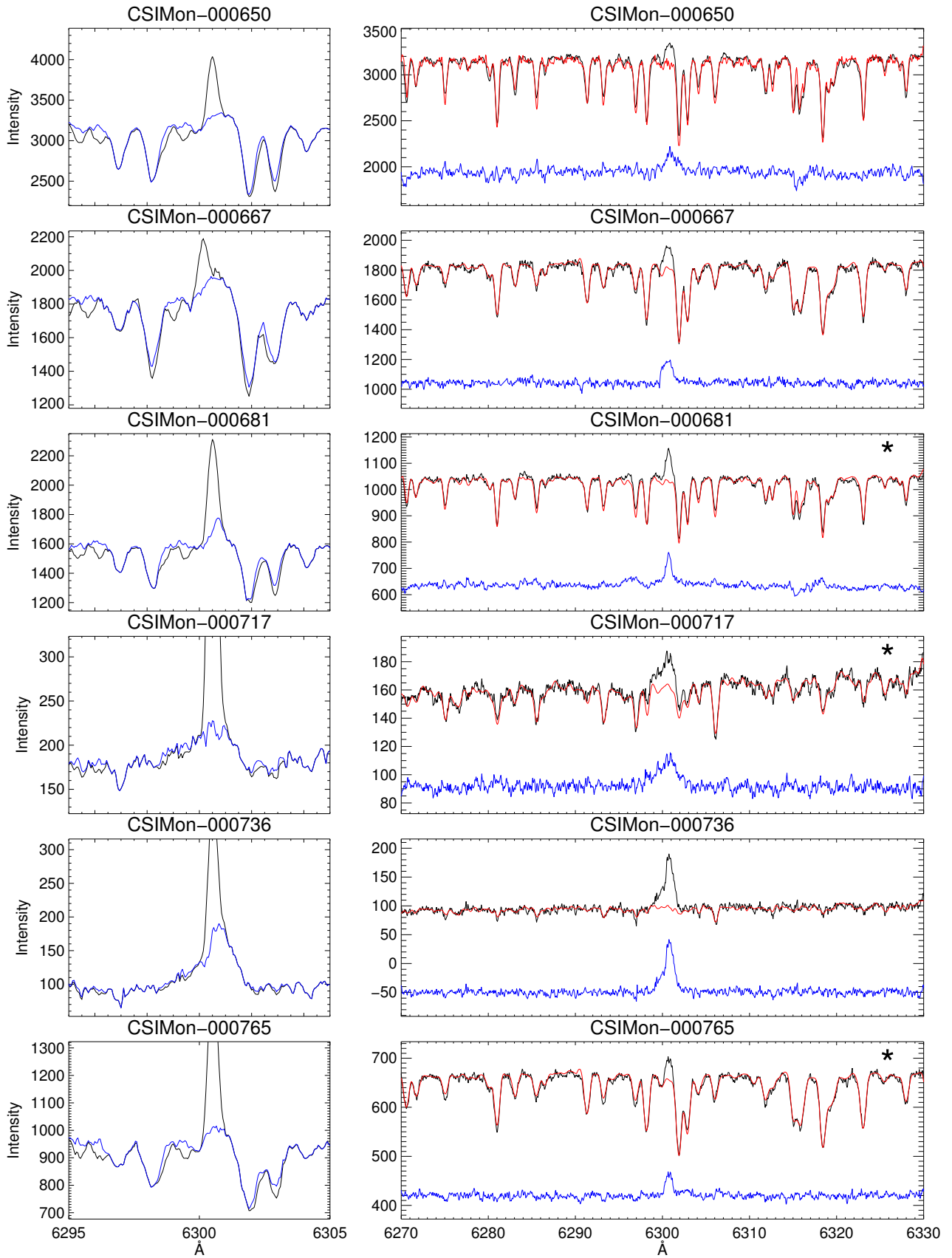


Fig. D.1: Continued.

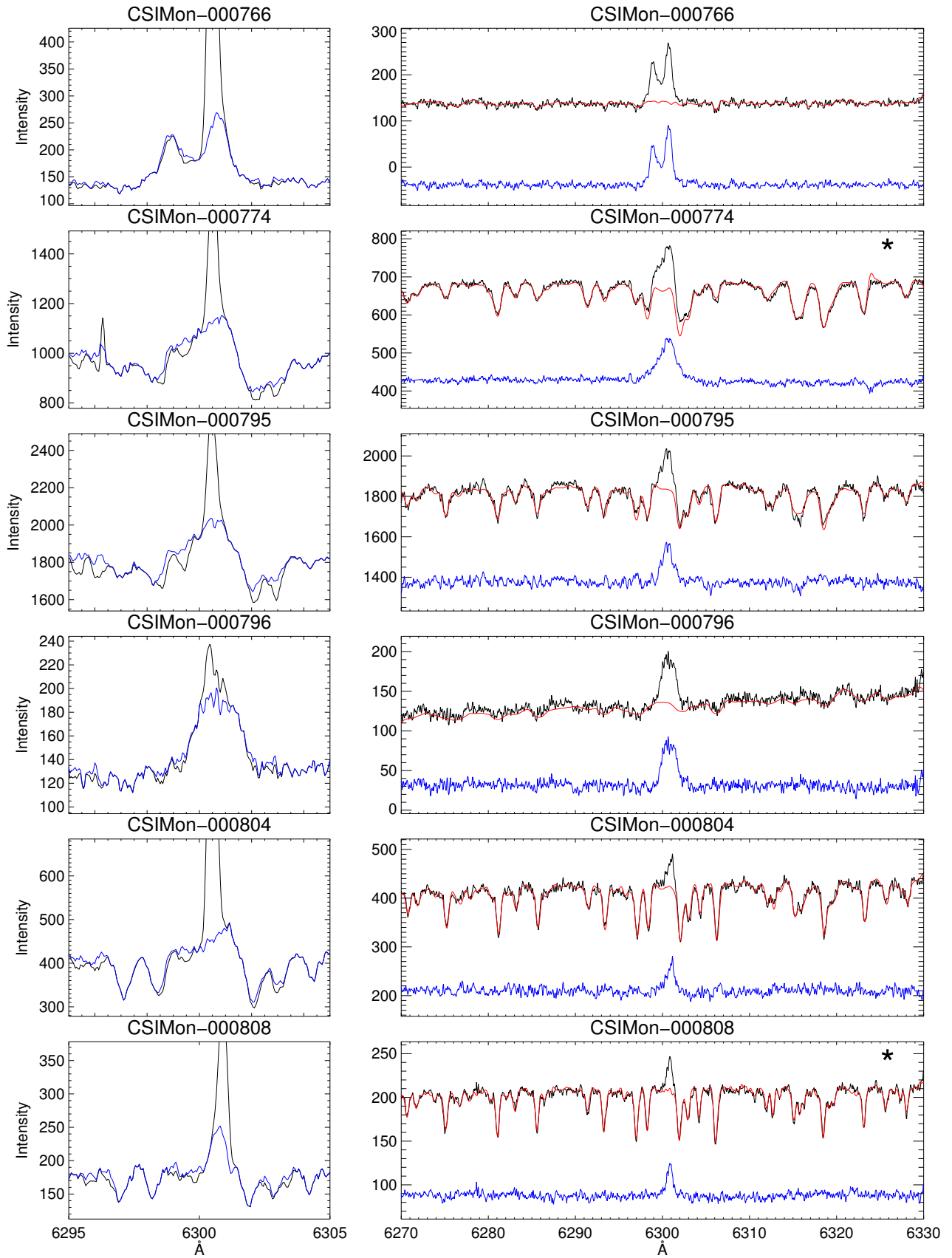


Fig. D.1: Continued.

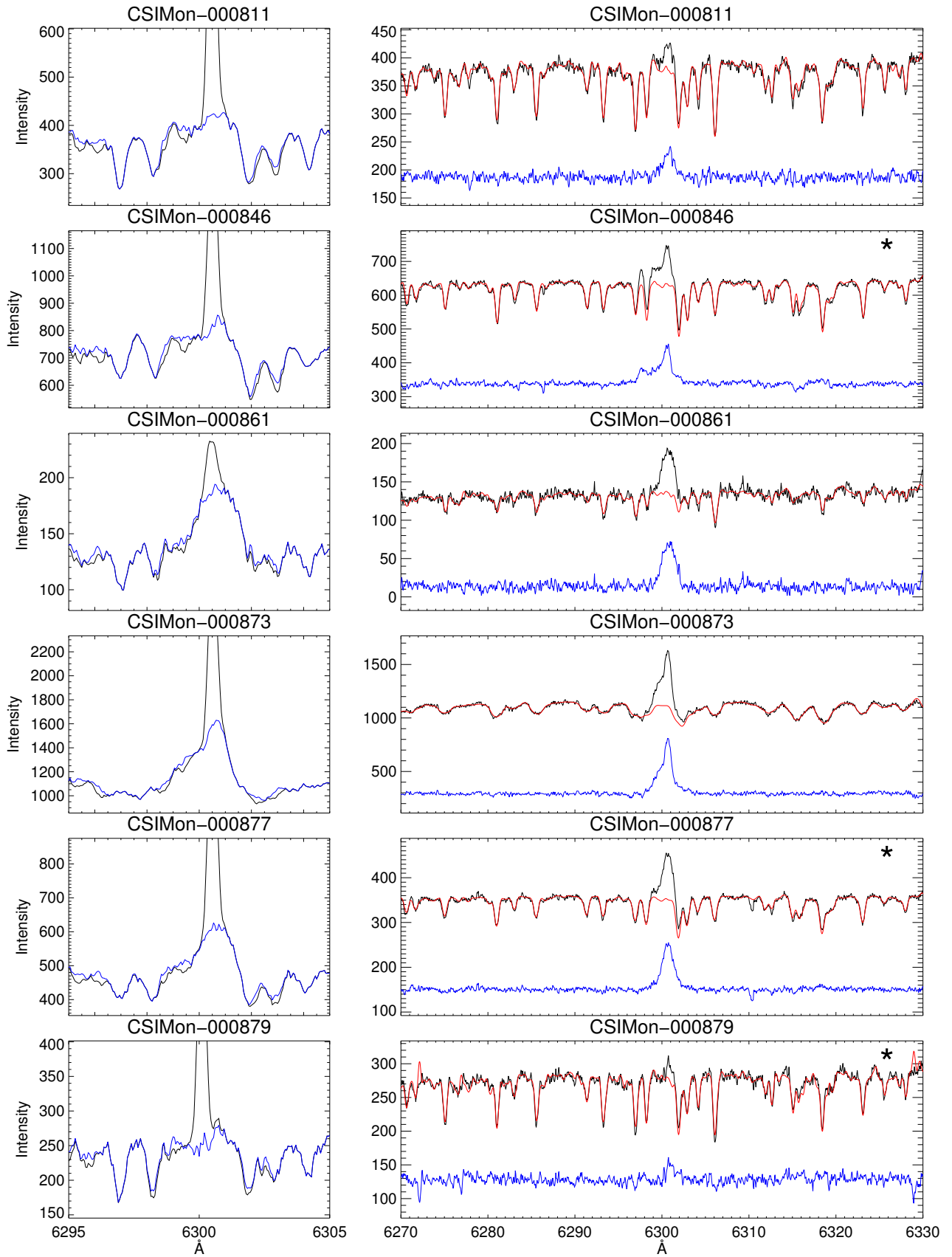


Fig. D.1: Continued.

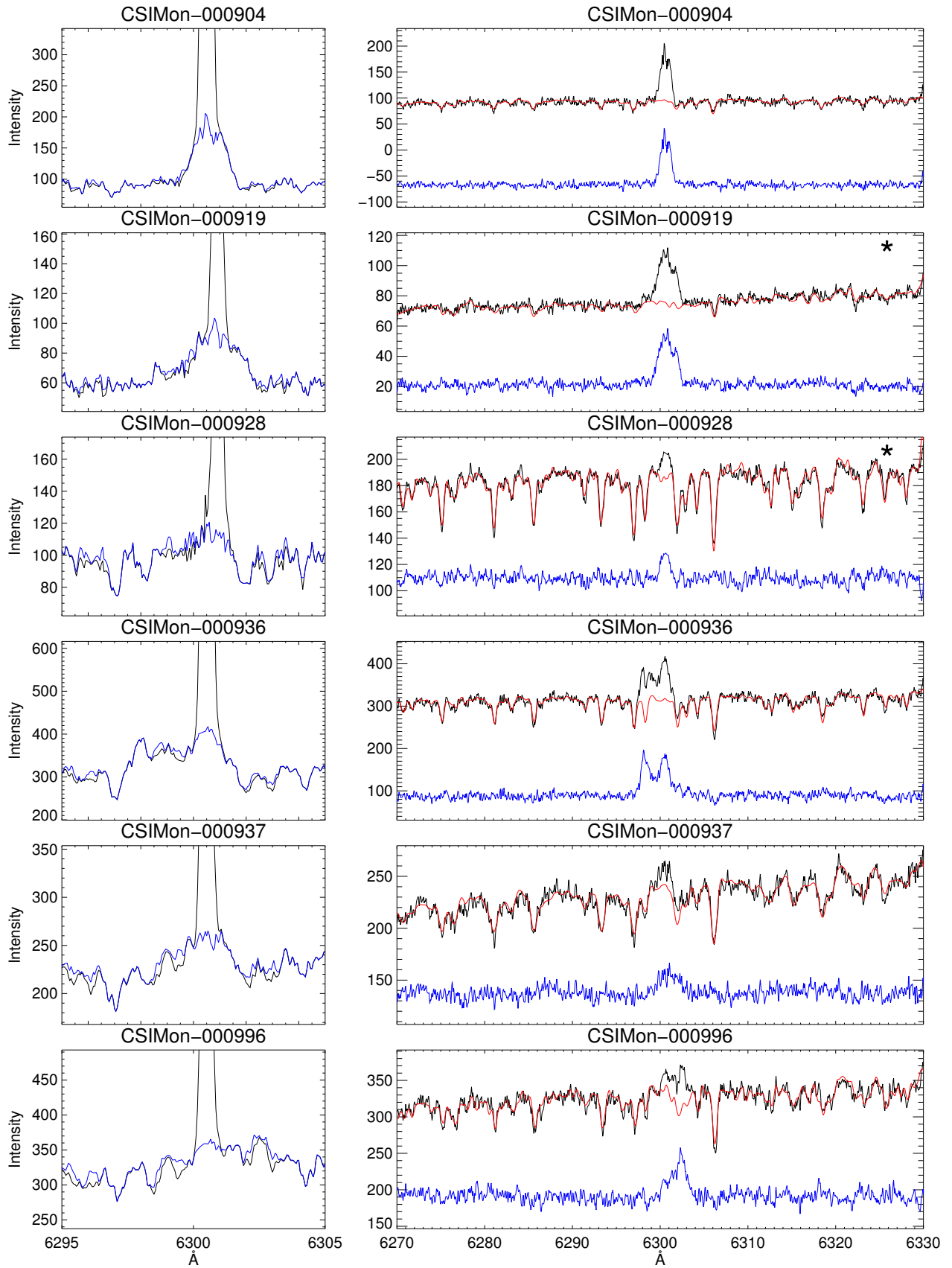


Fig. D.1: Continued.

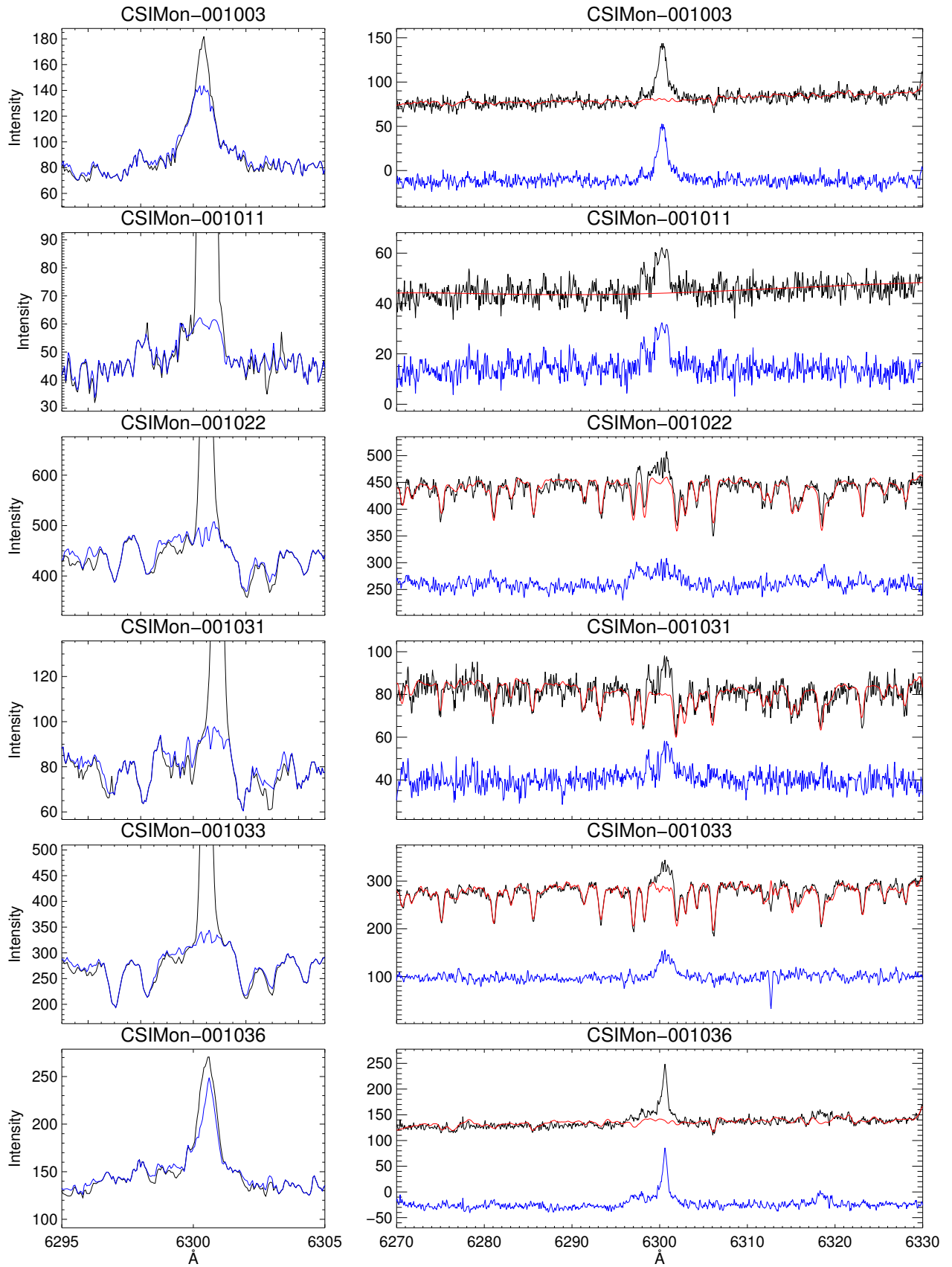


Fig. D.1: Continued.

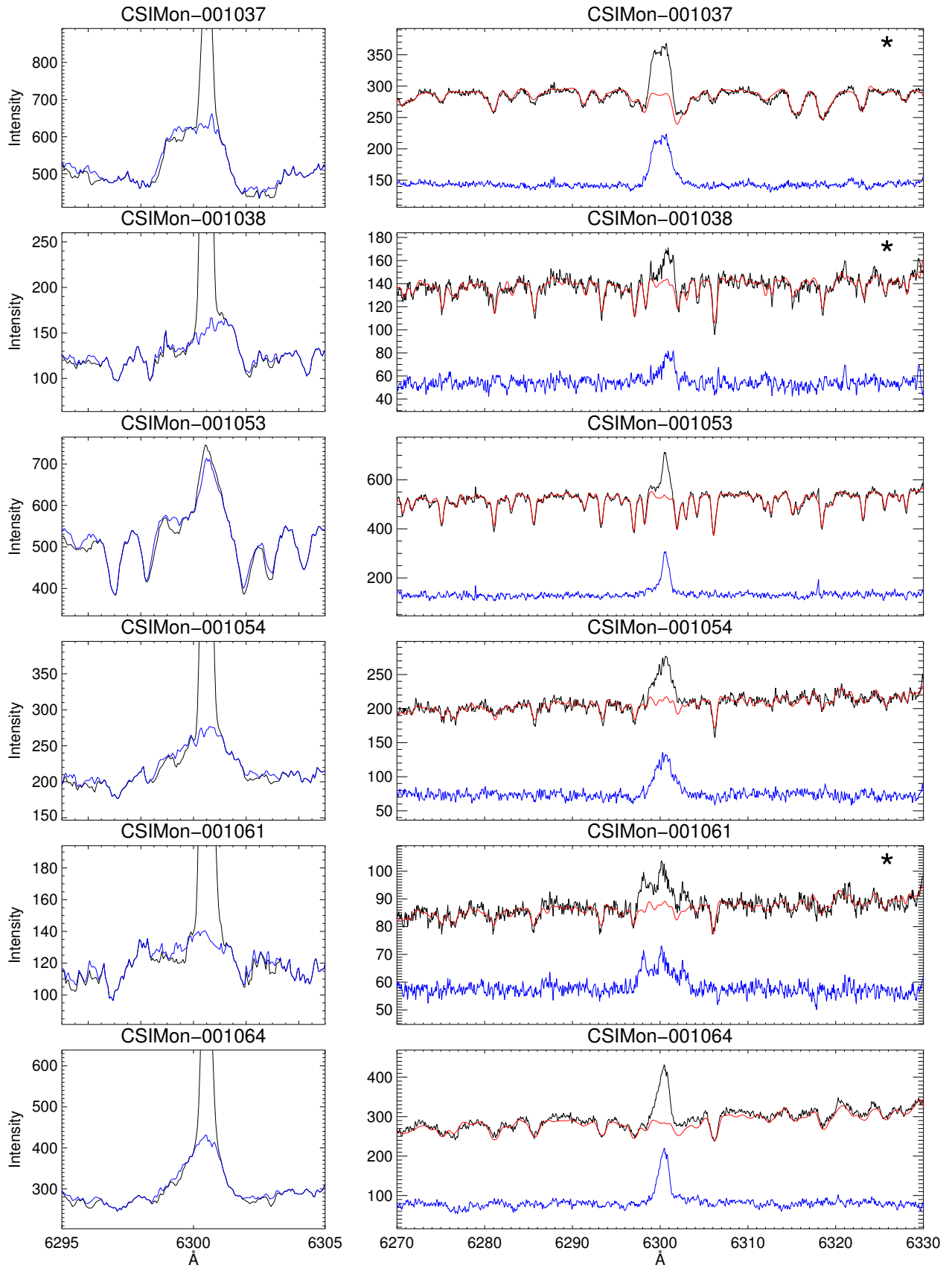


Fig. D.1: Continued.

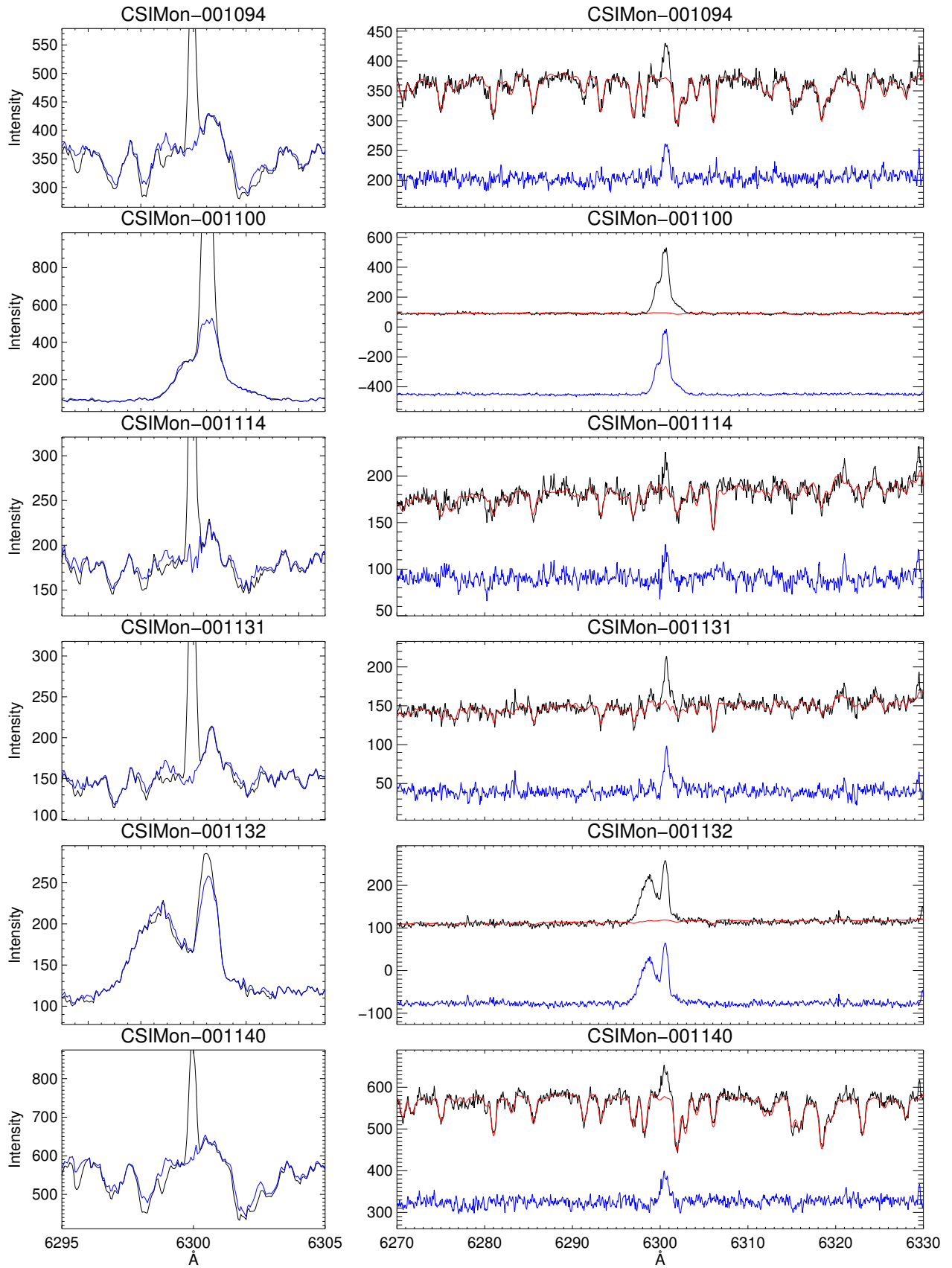


Fig. D.1: Continued.

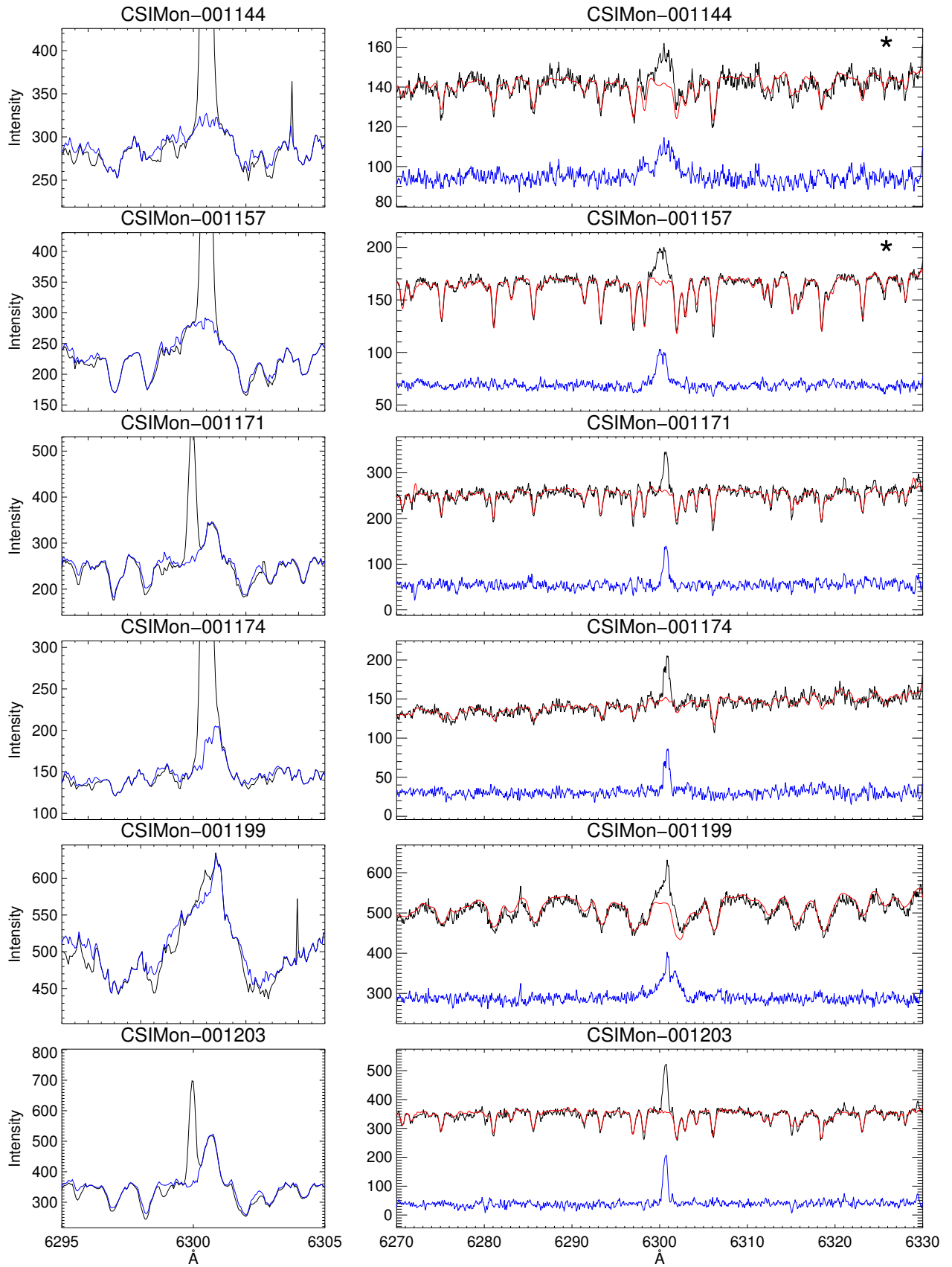


Fig. D.1: Continued.

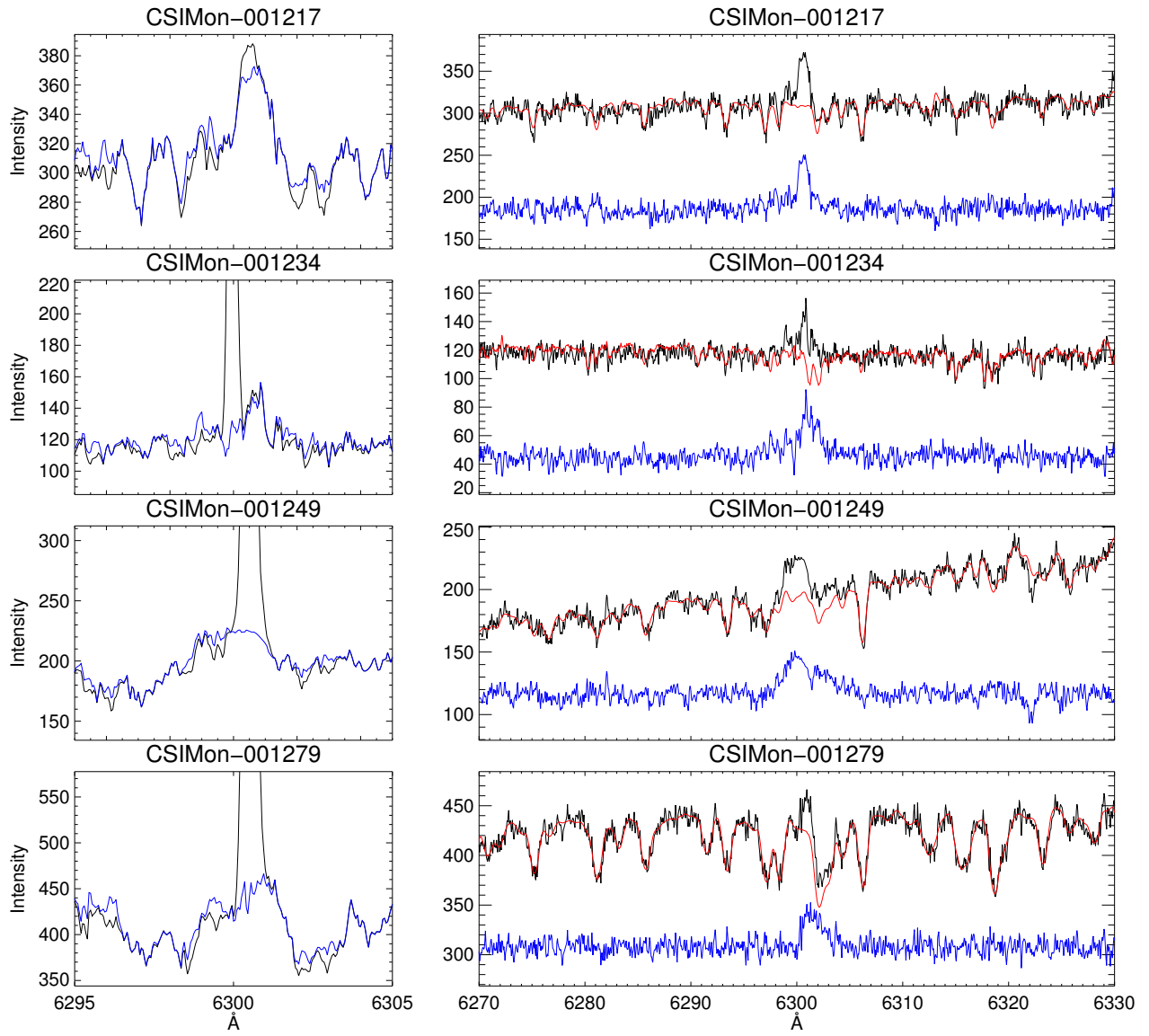


Fig. D.1: Continued.

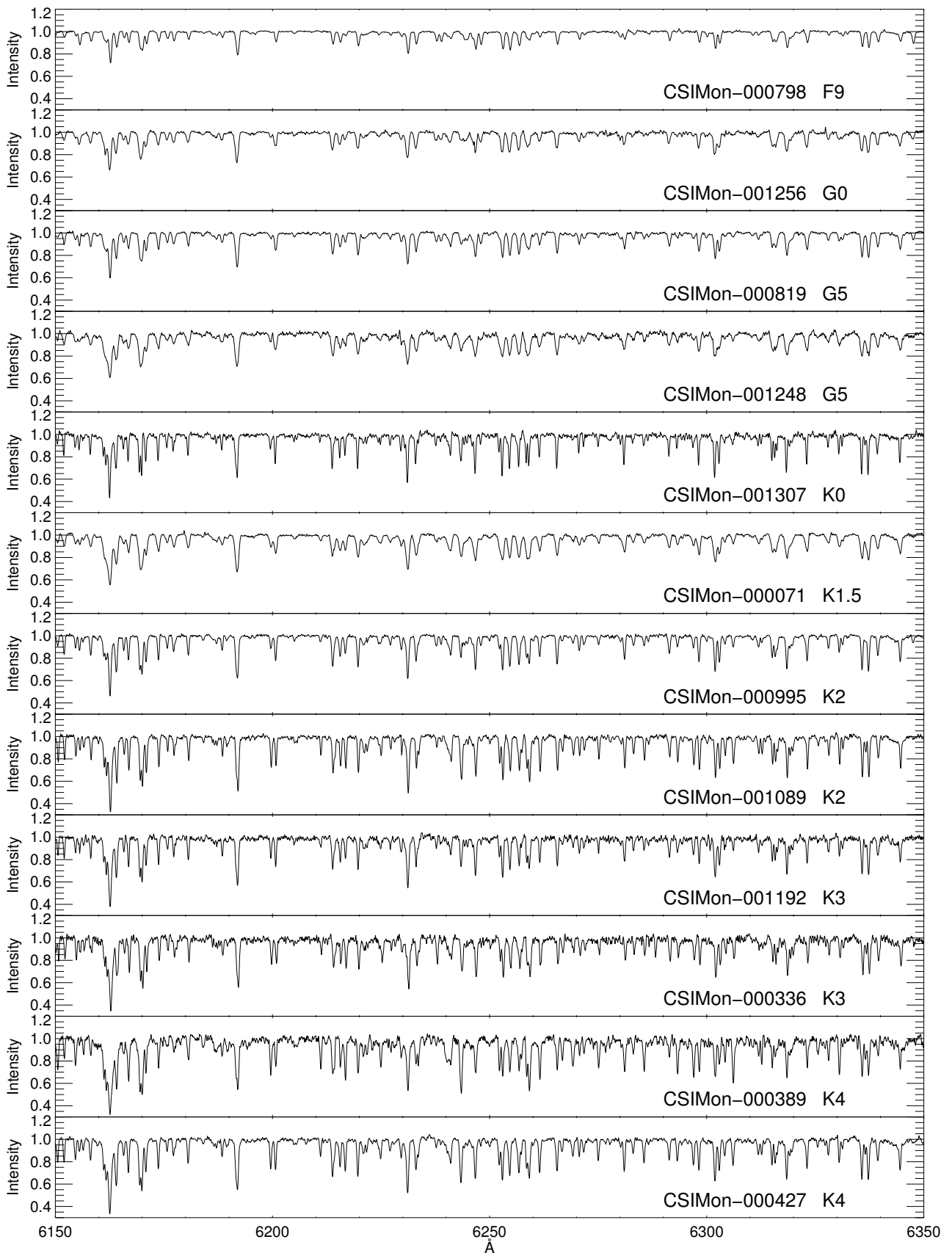


Fig. D.2: WTTs used as photospheric templates, ordered by spectral type (as given in the literature).

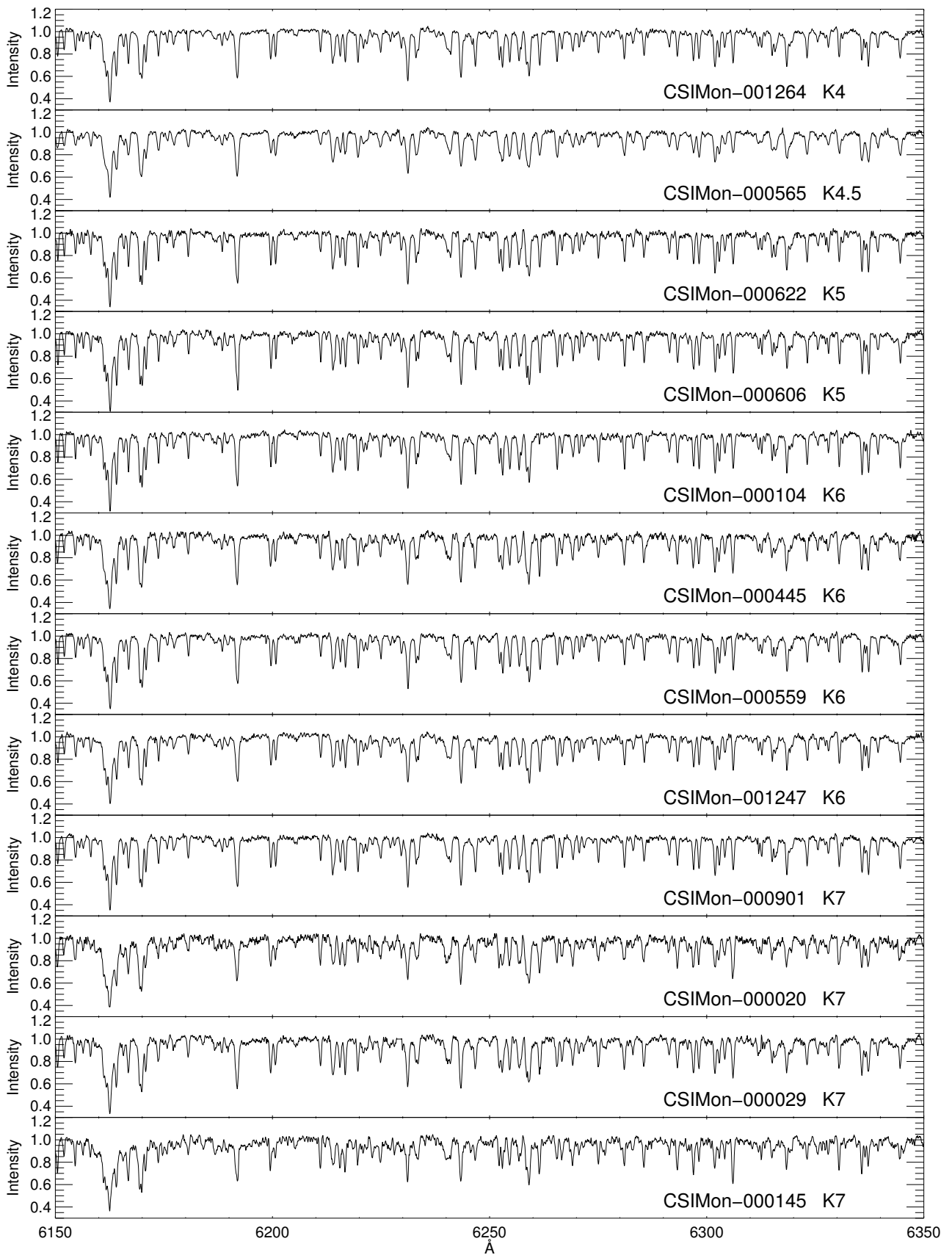


Fig. D.2: Continued.

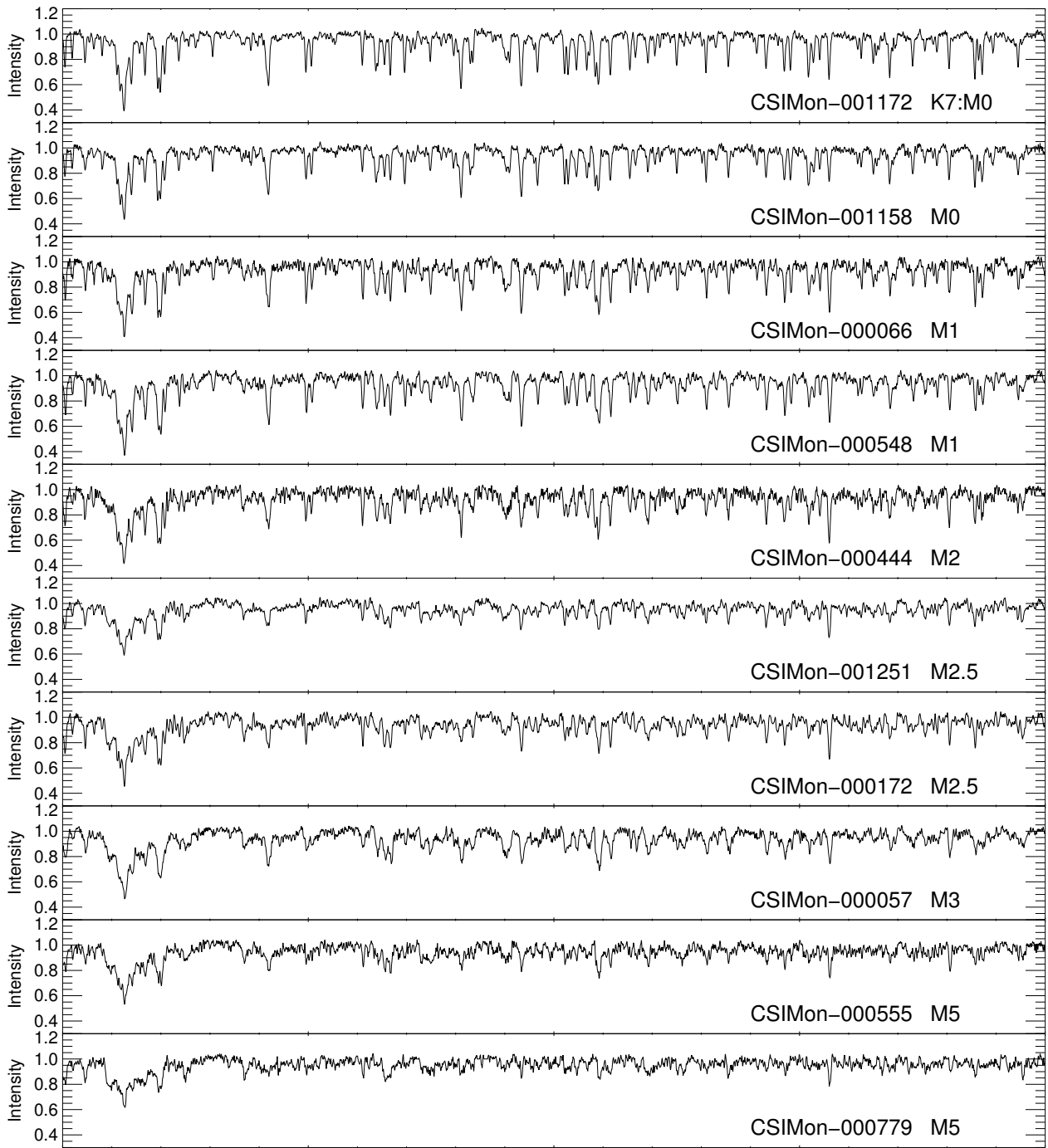


Fig. D.2: Continued.

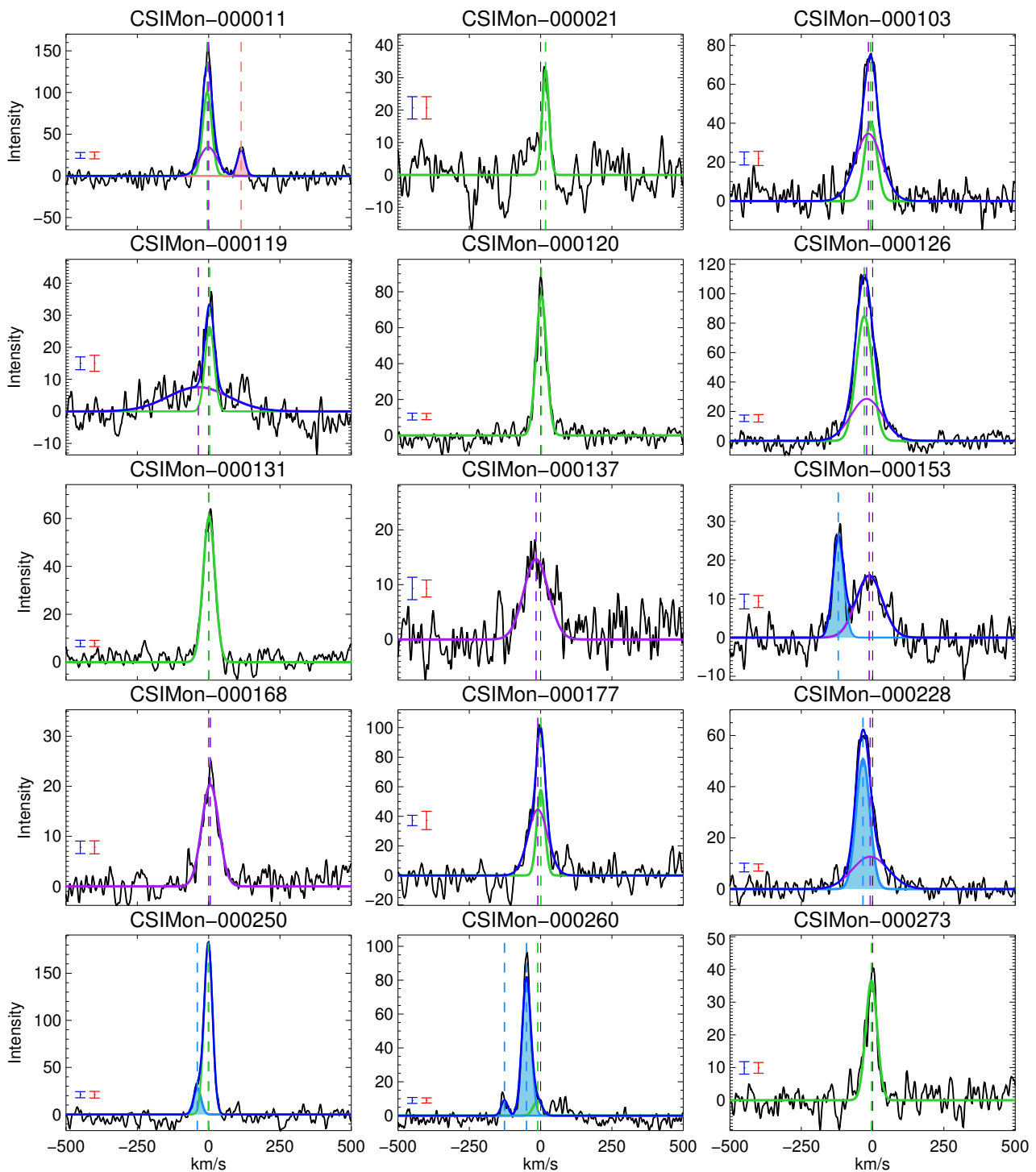


Fig. D.3: Gaussian decomposition of the [OI] $\lambda$ 6300 line profiles. Individual Gaussians are shown in different colors: in green are the narrow LVCs; in purple the broad LVCs; light blue shaded components represent blueshifted HVCs; and pink shaded components represent redshifted HVCs. The sum of all Gaussians is shown in blue. These are all plotted over the observed profile, which is in black. A red error bar in the bottom left corner of each panel shows the  $1\sigma$  level of residue of the final spectrum (corrected for telluric and photospheric contribution), while the blue error bar shows the  $1\sigma$  level of the noise in the continuum of the original, uncorrected spectrum.

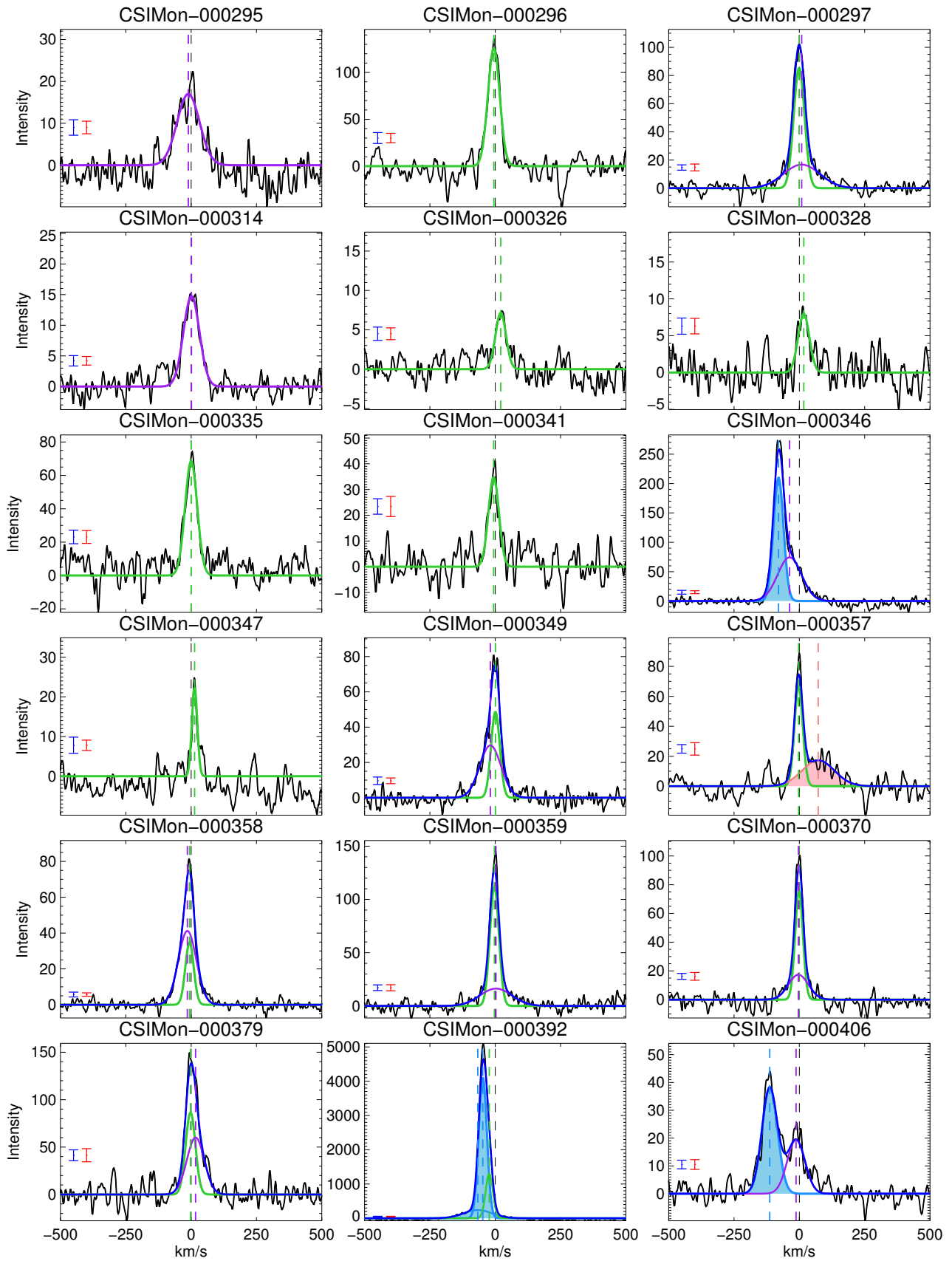


Fig. D.3: Continued.

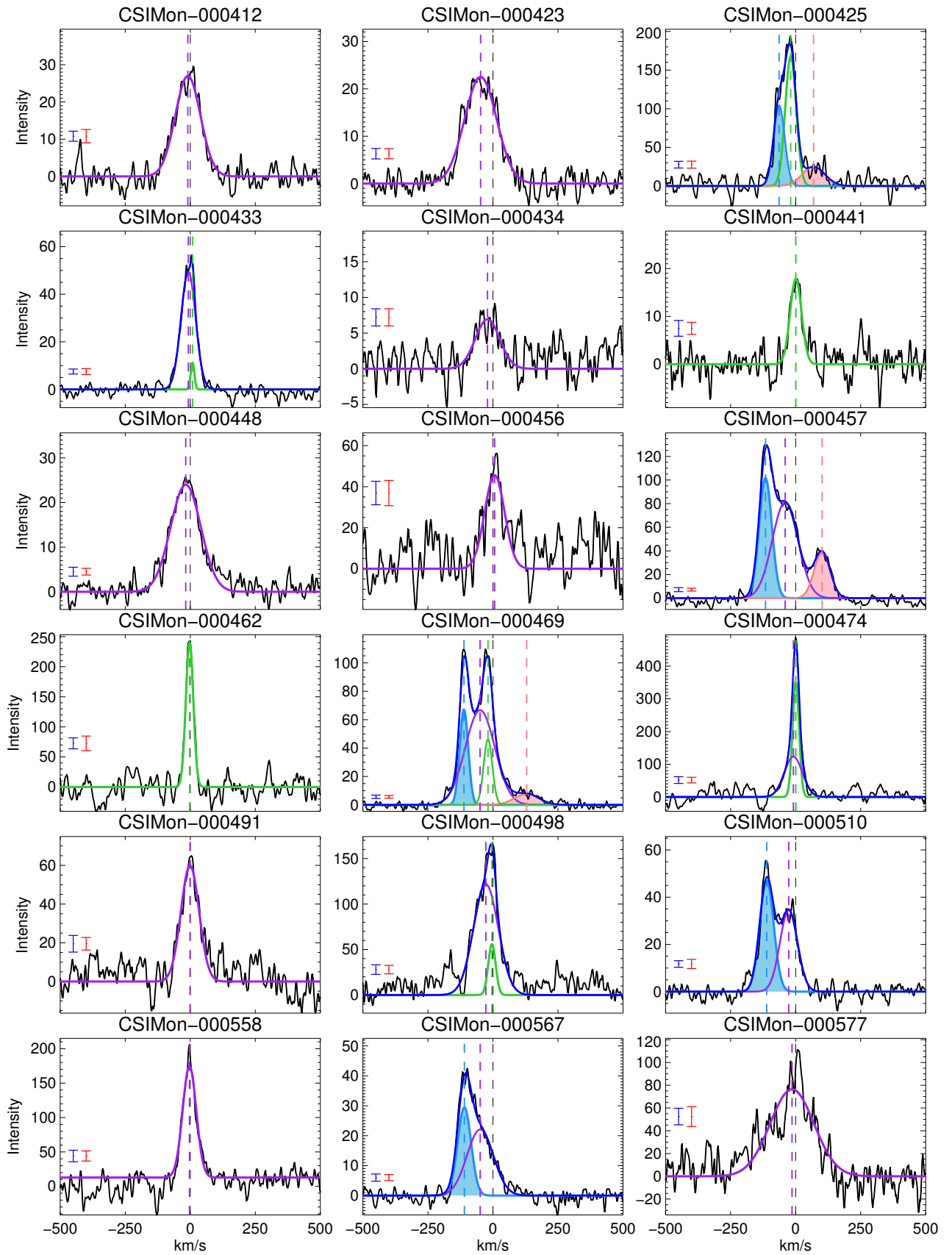


Fig. D.3: Continued.

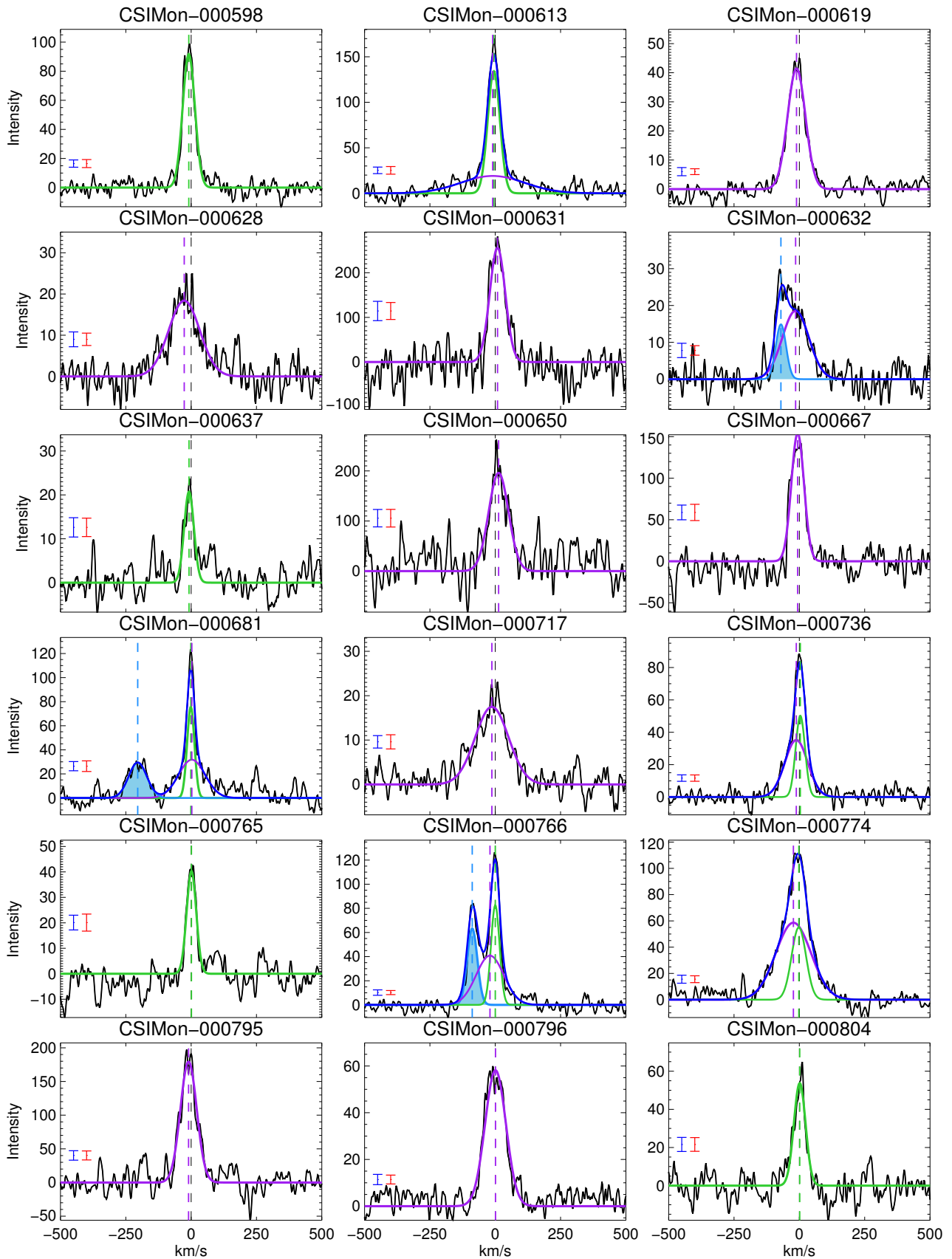


Fig. D.3: Continued.

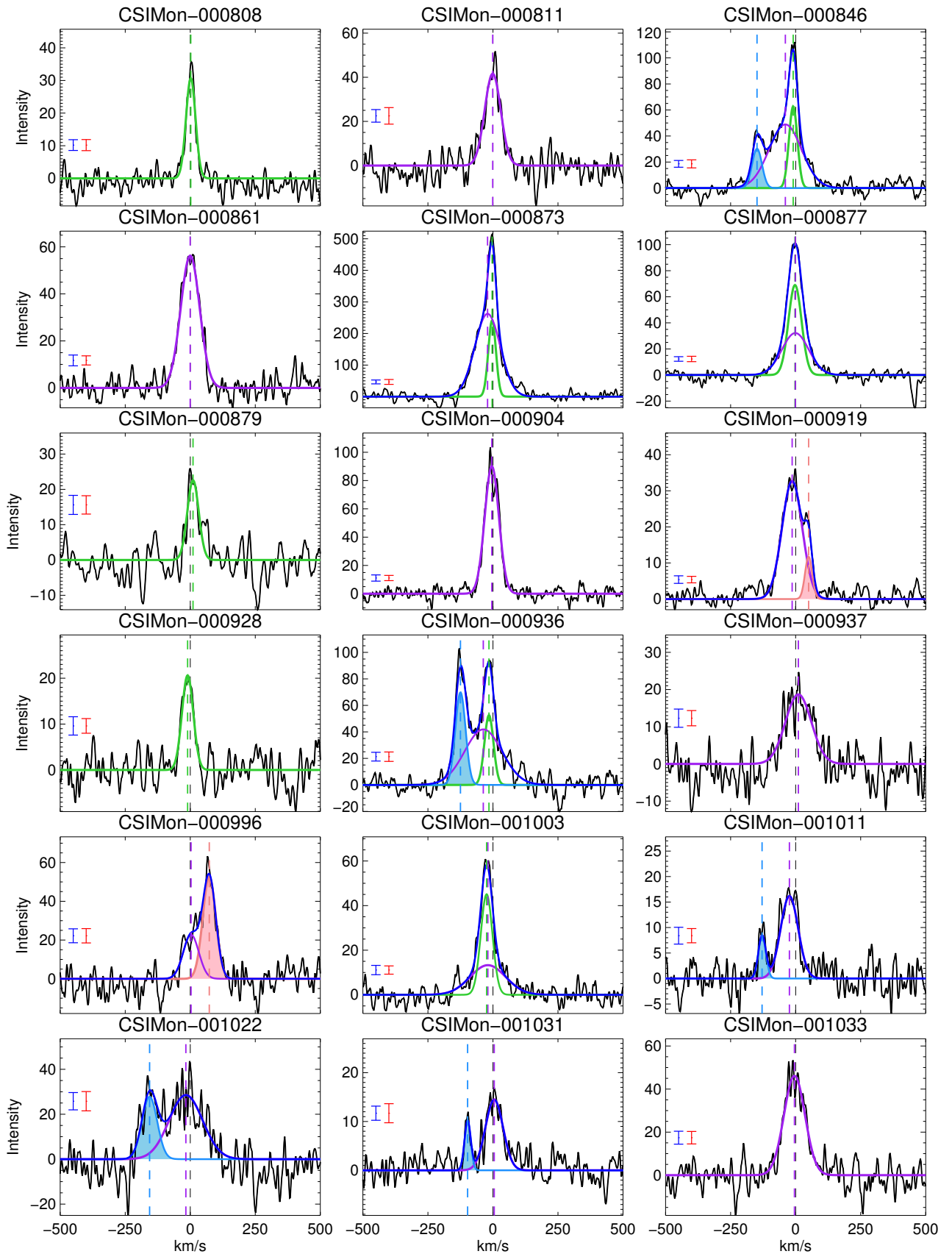


Fig. D.3: Continued.

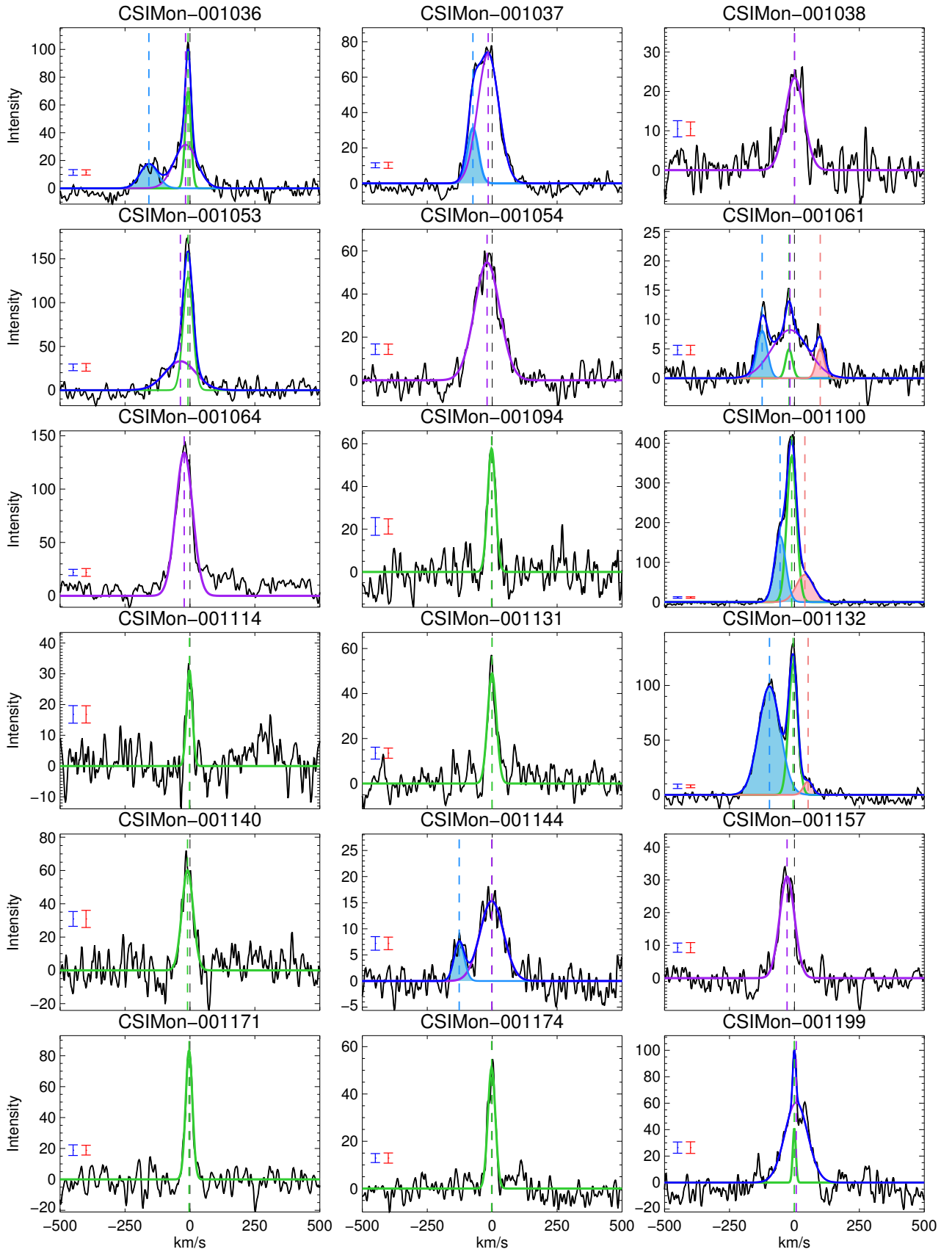


Fig. D.3: Continued.

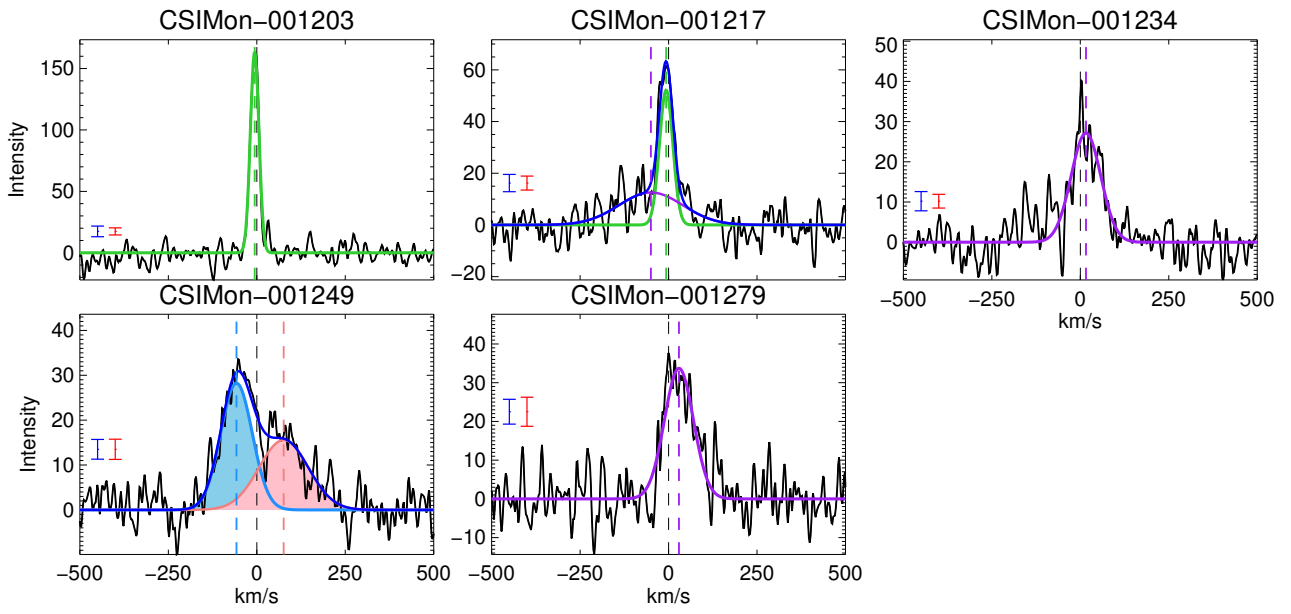


Fig. D.3: Continued.

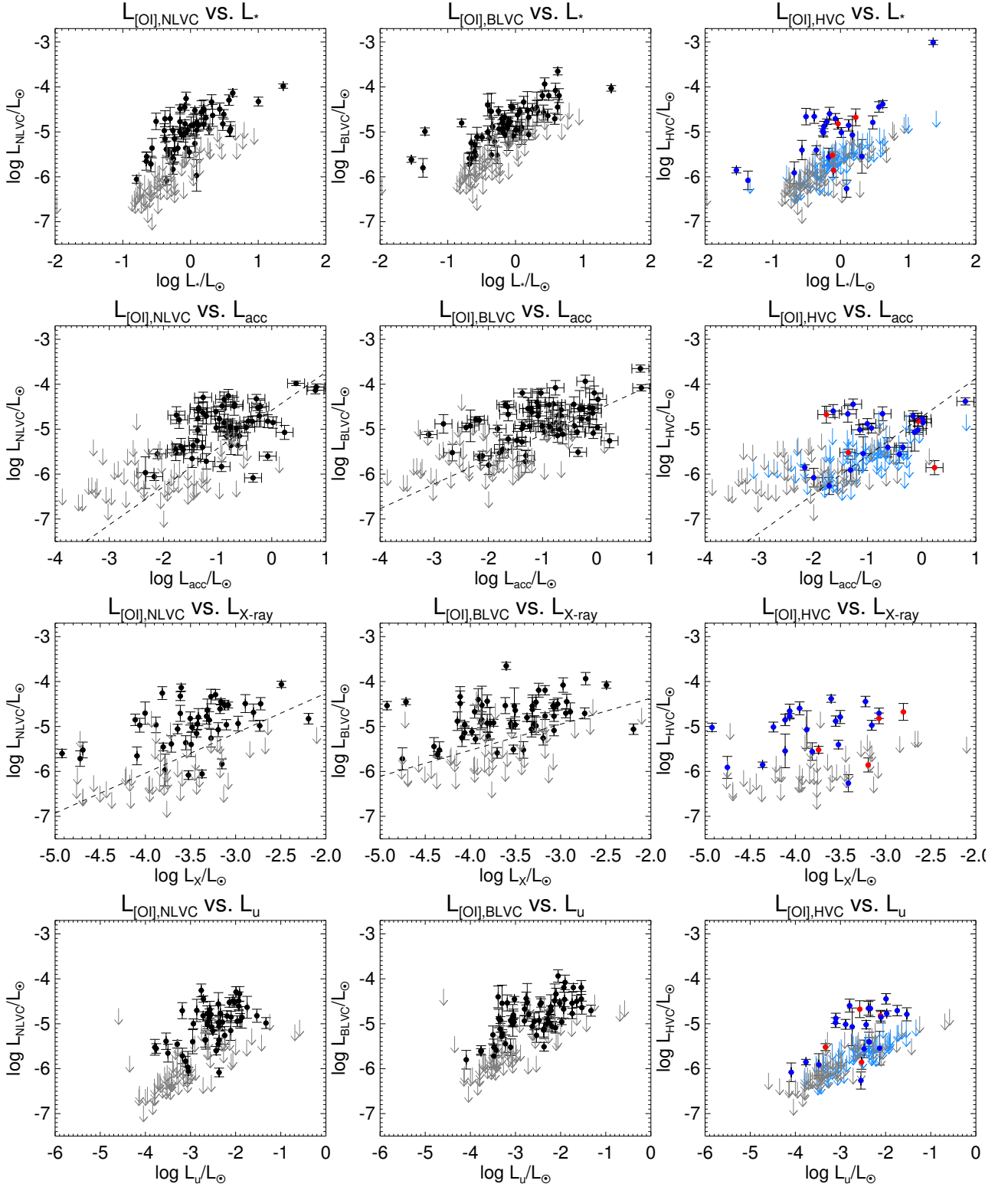


Fig. D.4: First row: Luminosity of each [OI] $\lambda$ 6300 component versus stellar luminosity. Second row: Luminosity of each [OI] $\lambda$ 6300 component versus accretion luminosity (derived from UV excess or H $\alpha$  profiles, in that order of preference). Third row: Luminosity of each [OI] $\lambda$ 6300 component versus X-ray luminosity. Fourth row: Luminosity of each [OI] $\lambda$ 6300 component versus the CFHT  $u$ -band luminosity. Gray arrows represent upper limits for [OI] $\lambda$ 6300 line luminosities when no emission in [OI] $\lambda$ 6300 was detected. In the HVC plots (right columns): light blue arrows represent upper limits for HVC luminosities when only low-velocity [OI] $\lambda$ 6300 emission was detected; blue filled circles represent blueshifted HVCs while red filled circles represent redshifted HVCs (systems that did not present a blueshifted component).